Electronic structure, magnetic ordering and phonons in molecules and solids

Von der Fakultät für Chemie und Physik
der TU Bergakademie Freiberg
angenommene
Habilitationsschrift
zur Erlangung des akademischen Grades
doctor rerum naturalium habilitatus
Dr. rer. nat. habil.
vorgelegt

von Dr. rer. nat. Jens Kortus
geboren am 1. Oktober 1967 in Potsdam

eingereicht am 21. März 2003

Gutachter: Prof. Dr. rer. nat. habil. Jochen Monecke, Freiberg
Prof. Dr. rer. nat. Ole K. Andersen, Stuttgart
Prof. Dr. rer. nat. habil. Gotthard Seifert, Dresden

Tag der Verleihung: 9. Dezember 2003

Contents

Preface

The present work gives an overview of the authors work in the field of electronic structure calculations. The density functional theory (DFT) is the theoretical background used for various applications from physics and chemistry. Therefore DFT is also the combining principle which joins the selected publications of the author. The main objective is to show how electronic structure methods can be used for the description and interpretation of experimental results in order to enhance our understanding of physical and chemical properties of materials. DFT is a very powerful method in that respect, as recognized by the Nobel prize in chemistry 1998.

This method has been successfully applied to many different classes of materials and properties. In order to place the present work in a proper context a brief introduction in the basics of DFT will be given. The main part of the work discusses the electronic structure of a few interesting examples. Today the electronic structure itself is an experimental property measured by angle resolved photo emission spectroscopy (ARPES), resonant inelastic X-ray scattering or probed directly by the de Haas-van Alphen (dHvA) effect. The recently found superconductor MgB_2 is an example where the electronic structure was the key to our understanding of the surprising properties of this material. The experimental confirmation of the predicted electronic structure from first principles calculations was very important for the acceptance of earlier theoretical suggestions.

The only input parameter to DFT is the atomic composition of the material, no further experimental information is required. Because it is possible to determine the forces acting on the atoms within the DFT, one can optimize the atomic postions, predict stable structures and calculate vibrational spectra. IR and Raman spectroscopy are widely used tools for materials characterization and first principles electronic structure calculations deliver very important information for interpreting these spectra. Not only vibrational frequencies but also IR and Raman intensities can be calculated from DFT, as will be discussed in a few examples.

Molecular crystals build from magnetic clusters containing a few transition metal ions and organic ligands show fascinating magnetic properties at the nanoscale. DFT allows for the investigation of magnetic ordering and magnetic anisotropy energies. The magnetic anisotropy which results mainly from the spin-orbit coupling determines many of the poperties which make the single molecule magnets interesting. Some recent results of the author in this field will be given.

Chapter 1

Introduction to DFT

Molecules and solids are complicated many-particle systems which are in principle described by the corresponding Schrödinger equation. Unfortunately, analytic solutions are available only for a few very simple systems [1], and even numerically exact solutions are limited to a small number of atoms or electrons. Therefore one is forced to find accurate approximations in order to describe real materials. The density-functional theory is one of the most successful methods in that respect.

Within the scope of this work we will give only a brief introduction to the basic foundations of density functional theory [2, 3]. There are excellent reviews available on that topic [4–8] which will give much more insight in the theoretical basics, accuracy and limitations than this short overview.

In principle electrons and atomic nuclei can be treated at the same theoretical basis, although the problem can be simplified by decoupling the electronic and nuclear degrees of freedom. In many cases it is very appropriate to assume that electronic and nuclear dynamics take place at different time scales and can therefore be separated. This approach called Born-Oppenheimer approximation considers all nuclei as fixed in space during the electronic relaxation.

The stationary Schrödinger equation of a system consisting of N electrons is given by:

$$\left\{ -\sum_{i}^{N} \frac{\hbar^2 \Delta_i}{2\, m_e} + \sum_{j}^{N} v(\mathbf{r}_j) + \sum_{j>i}^{N} \frac{e^2}{4\pi\varepsilon_0\, |\mathbf{r}_i - \mathbf{r}_j|} - E \right\} \Phi(\mathbf{r}_1, \ldots, \mathbf{r}_N) = 0 \qquad (1.1)$$

where

$$v(\mathbf{r}_j) = -\sum_{i} \frac{Z_i e^2}{4\pi\varepsilon_0\, |\mathbf{R}_i - \mathbf{r}_j|} \qquad (1.2)$$

$\mathbf{R}_i$ and Z_i are the coordinates and atomic numbers of the nuclei. The spin variables have been omitted for clarity (or the $\mathbf{r}_i$ could be interpreted as generalized coordinates which include the spin degrees of freedom too). From here on we will use atomic units (1 Hartree = 27.2116 eV, 1 a_B=0.529177 Å).

The most important observation for a non-degenerate ground state of this many-electron system is, that the total energy can be expressed as a unique functional of the electron density $\rho(\mathbf{r})$ [2], which is determined solely by the locations $\mathbf{R}_i$ of the nuclei.

$$E_{tot} = T_0[\rho(\mathbf{r})] + \int \mathrm{d}\mathbf{r}\rho(\mathbf{r})v(\mathbf{r}) + E_H[\rho(\mathbf{r})] + E_{xc}[\rho(\mathbf{r})] \tag{1.3}$$

where

$$V_H[\rho(\mathbf{r})] = \frac{1}{2}\int \mathrm{d}\mathbf{r}\rho(\mathbf{r})V_H(\mathbf{r}) = \frac{1}{2}\iint \mathrm{d}\mathbf{r}\mathrm{d}\mathbf{r}'\frac{\rho(\mathbf{r})\rho(\mathbf{r}')}{|\mathbf{r}-\mathbf{r}'|} \tag{1.4}$$

$T_0[\rho(\mathbf{r})]$ is the kinetic energy of a non-interacting electron gas with density $\rho(\mathbf{r})$, E_H is the Hartree energy due to the average electrostatic interaction of the electrons. $E_{xc}[\rho(\mathbf{r})]$ is the exchange-correlation energy, which is in general an unknown functional of the electron density. The potential $v(\mathbf{r})$ for an interacting N-electron system is defined as a general external potential. The knowledge of the ground state density $\rho(\mathbf{r})$ determines the external potential within an irrelevant constant. The initial proof of the above statement given by Hohenberg and Kohn in 1964 [2] has been extended also to the lowest state of each symmetry [9], degenerate ground states [7] or spin density functional theory [8].

1.1 Kohn-Sham equation

The ground state density must give the lowest energy by definition. This allows to use the variational principle in order to obtain the ground state energy. Instead of using the electron density directly, Kohn and Sham [3] suggested to represent the electron density in terms of single particle orbitals $\psi_{i\sigma}$. Minimization of the total energy functional (1.3) with the constraint that the single particle orbitals fulfill a normalization condition leads to the Kohn-Sham equation:

$$\left[-\frac{\Delta}{2} + v(\mathbf{r}) + V_H[\rho(\mathbf{r})] + V_{xc}^{\sigma}[\rho_\uparrow(\mathbf{r}),\rho_\downarrow(\mathbf{r})]\right]\psi_{i\sigma} = \varepsilon_{i,\sigma}\psi_{i\sigma}, \tag{1.5}$$

$$V_{xc}^{\sigma}[\rho_\uparrow(\mathbf{r}),\rho_\downarrow(\mathbf{r})] = \frac{\delta E_{xc}[\rho_\uparrow(\mathbf{r}),\rho_\downarrow(\mathbf{r})]}{\delta\rho_\sigma(\mathbf{r})}, \tag{1.6}$$

$$\rho(\mathbf{r}) = \rho_\uparrow(\mathbf{r}) + \rho_\downarrow(\mathbf{r}) = \sum_{i,\sigma}\Theta(\mu-\varepsilon_{i,\sigma})\left|\psi_{i\sigma}\right|^2. \tag{1.7}$$

Here σ is the z-component of the spin variable and the external potential $v(\mathbf{r})$ is due to the nuclei. The step function $\Theta(\mu-\varepsilon_{i,\sigma})$ ensures that all Kohn-Sham orbitals with $\varepsilon_{i,\sigma} < \mu$ are occupied and the chemical potential μ is defined by conservation of charge

$$\int \mathrm{d}\mathbf{r}\rho(\mathbf{r}) = N. \tag{1.8}$$

Equation (1.5) is a significant simplification compared with the initial many electron problem (1.1), because it presents a single particle equation. The original interacting electron system has been replaced by a system of non-interacting electrons in an effective potential. However, all the difficulties are conserved in the exchange correlation functional E_{xc} which is not explicitely known.

It should be noticed, since the functionals in (1.5) depend on the electron density and thus on the Kohn-Sham orbitals themselves, the Kohn-Sham equation has to be solved self-consistently until input and output densities are identical.

1.2 The exchange-correlation energy

The only unknown quantity is the exchange-correlation energy and many efforts are devoted to seek approximations for this functional. Different functionals have been proposed and today several functionals exist which give excellent results for most molecular and solid properties.

While E_{xc} is often only a small fraction of the total energy of an atom, molecule or solid it is an important contribution to the chemical bonding energy or atomization energy. The exchange-correlation energy is the glue, without most matter would bind only very weakly. Therefore, very accurate approximations of E_{xc} are essential in order to obtain reliable results from DFT calculations.

1.2.1 Local Spin Density Approximation: LSDA

The most widely used approximation in the past has been the local spin density approximation (LSDA)

$$E_{xc}[\rho_\uparrow(\mathbf{r}), \rho_\downarrow(\mathbf{r})] = \int \mathrm{d}\mathbf{r}\rho(\mathbf{r})\varepsilon_{xc}(\rho_\uparrow(\mathbf{r}), \rho_\downarrow(\mathbf{r})) \tag{1.9}$$

where $\varepsilon_{xc}(\rho_\uparrow(\mathbf{r}), \rho_\downarrow(\mathbf{r}))$ is the exchange and correlation energy of a homogenous electron gas of the corresponding spin densities. The exchange-correlation energy for a uniform electron gas is known with great accuracy ($\sim$ 0.1 %) and can be obtained by Quantum Monte-Carlo simulations [10, 11] for various values of the spin densities which are then parameterized. Among others, different parameterizations for $\varepsilon_{xc}(\rho_\uparrow(\mathbf{r}), \rho_\downarrow(\mathbf{r}))$ have been given by Gunnarsson and Lundqvist [9], von-Barth and Hedin [12], Vosko *et al.* [13], and Perdew and Zunger [14]. This approximation is based on the assumption of slowly varying densities, which is unfortunately not fulfilled in most molecules or solids. Surprisingly, LSDA has been shown to give satisfactory results for equilibrium bond lengths (1% too short), elastic constants and vibrational properties. The

main weakness is the well known tendency to overbind, that means to overestimate the total energies of condensed matter compared with their atomic constituents. For example it has been shown for 20 selected molecules, that the mean absolute error of the atomization energies has a value of 1.3 eV [15]. Similarly, energy barriers are calculated too small.

1.2.2 Generalized Gradient Approximations: GGA

The best energy functionals or potentials used currently depend on the spin densities, their gradients and their second derivatives. The most common approximations for the gradient corrected functionals have been developed by Perdew and coworkers [15, 16] and Becke, Lee, Yang and Parr [17, 18]. This is still an area of active research in order to achieve the goal of *chemical accuracy* ($\sim$ 50 meV for atomization energies).

GGA normally improves significantly on energy barriers or atomization energies. The average absolute error of the atomization energies for the same 20 molecules as mentioned before reduces to 0.3 eV [15]. The bond lengths show similar accuracy as the ones obtained from LSDA with 1% accuracy, although the bond lengths are now too long compared with experiment. Some extensive tests of GGA functionals can be found in [6, 15, 16].

1.3 Basis Set Expansion

In order to make further progress one has to expand the Kohn-Sham orbitals in terms of a basis set. A straight-forward approach would be the solution of the numerical problem on a real space mesh without any restrictions. The DMOL^3 code [19] follows this approach and uses numerical functions on an atom-centered grid as its atomic basis. The atomic basis functions are obtained from solution of the DFT equations for individual atoms and are stored as sets of cubic spline.

Nevertheless, due to the numerical difficulties most DFT implementations are based on expanding $\psi_{i\sigma}$ in terms of suitable basis functions $\phi_j(\mathbf{r})$. The Kohn-Sham orbitals can be expressed as a product of spatial basis functions $\phi_j(\mathbf{r})$ and spinors (χ_σ) according to:

$$\psi_{i,\sigma}(\mathbf{r}) = \sum_j c_j^{i\sigma} \phi_j(\mathbf{r}) \chi_\sigma \tag{1.10}$$

Once this ansatz is introduced, one varies the expansion coefficients ($c_j^{i\sigma}$) rather than the value of each wavefunction at each point in space which leads to a secular equation.

The choice of basis functions $\phi_j(\mathbf{r})$ determines the size of the matrix one has to diagonalize, which is often the most time consuming part of the calculations.

All-electron approaches consider both core and valence electrons explicitely. The strongly localized core electrons consequently require strongly localized basis functions such as linearized augmented plane waves (LAPW) [20] or linearized muffin-tin orbitals (LMTO) [21], Slater-type orbitals [22] or Gaussian-type orbitals (GTO) [22–28]. Pseudopotentials, which effectively project out the core states from the problem, allow for the use of plane waves as basis functions. Plane waves are numerically very easy to handle but result in rather large basis sets. The use of intelligible and numerical efficient basis functions is crucial for the development of the DFT method. The best suited basis should be chosen based on the problem to solve, but is more often dictated by the availability of a certain program package.

Many algorithms for the solution of the above equations exist, and the algorithm that one uses depends rather strongly on the form of the spatial basis functions that are used.

1.4 NRLMOL implementation

The Naval Research Laboratory Molecular Orbital Library (NRLMOL) program is an all-electron Gaussian-type orbital implementation of DFT [29–38]. Because the author spent a large fraction of his time working on and using extensively the NRLMOL program package developed by Pederson, Jackson and Porezag it seems suitable to give some details on this particular numerical implementation.

The molecular orbitals were expanded as linear combinations of Gaussian functions centered at the atomic sites. The multicenter integrals required in the solution of the Kohn-Sham equation are calculated by integrating numerically over a mesh of points [30]. Many LSDA and GGA functionals are available. One important feature is a very efficient parallelization which allows for calculations of more than 100 atoms at the all-electron level, which becomes important in case of the molecular magnets discussed later in this work. Here the parallel version will not be discussed , please see Ref. [38] for more information.

In Figure 1.1, a simplified flow chart is presented that describes the standard tasks which are used in NRLMOL in order to self-consistently solve the Kohn-Sham equations (1.5).

As shown in the flow chart, it is first necessary to determine the locations and charges of the basis sets. Once these are determined, the program uses a previously generated basis set [37]. The basis set has been obtained by performing an self-consistent LDA calculation of the spherical unpolarized atom where the total energy of the atom was converged to within 10 meV.

Second, for each isolated atom the self-consistent potential is numerically determined and a least-square representation of it is generated. These potentials are expanded as a sum of bare spherical Gaussians or as a sum of Gaussian-

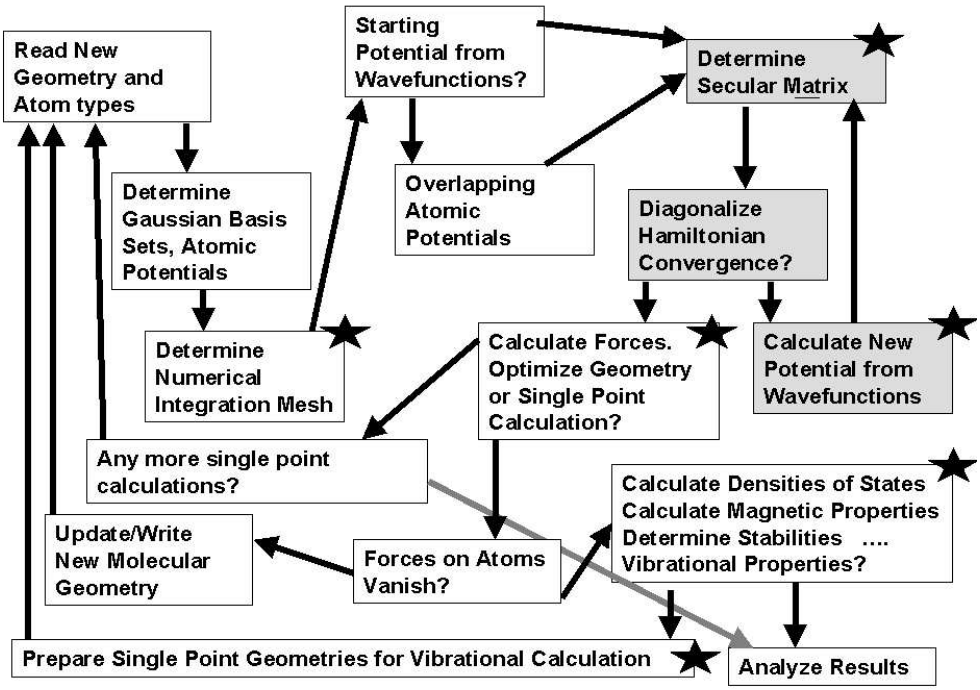

Figure 1.1: Flow chart of parallel version of NRLMOL. The gray area represents the iterative part of the self-consistency cycle which is the computationally intensive part of the problem. The stars on the boxes represent the tasks which are massively parallelized.

screened $1/r$ potentials.

Given the basis sets and the Gaussian-representation of the atomic potentials, it is possible to obtain very good insight into the class of multicenter integrands that need to be integrated, and this information is used to generate a numerical variational integration mesh [30] that allows to precisely determine integrals required for calculation of secular matrices, total energies and derivatives according to:

$$I = \int \mathrm{d}\mathbf{r} Q(\mathbf{r}) = \sum_i Q(\mathbf{r}_i)\Omega_i \tag{1.11}$$

where Ω_i is the volume associated with point $\mathbf{r}_i$. Once the variational mesh is determined the calculation starts. Errors arising from the numerical integration can easily be checked and controlled by adjusting a few parameters which control the mesh construction.

For a new problem, a guess of the Hamiltonian matrix or self-consistent wavefunctions is not available so one relies on the least-square fit representa-

tion of overlapping atomic potentials to determine a starting Hamiltonian. Once the wavefunctions are determined, by solution of Poissons equation it is possible to calculate the potential due to these wavefunctions. Further, the Coulomb potential due to the electrons and the nuclei as well as the exchange-correlation energy density and potentials are required. The exchange-correlation term requires the evaluation of spin densities and the first and second derivatives of the spin densities for GGA. The solution of the Kohn-Sham equation (1.5) for that potential determines the new wavefunctions. The equations are then solved self-consistently by iterating until the total energy is converged to a μHartree.

The number of iterations required to reach self-consistency can be significantly decreased by using sophisticated mixing of input and output potentials which were originally proposed by Broyden and others. We use the Broyden algorithm of Johnson in our calculations [39].

Once self-consistency is achieved the forces acting on each atom are determined from the Hellmann-Feynman-Pulay theorem. [40] The determination of the Hellmann-Feynman force is relatively inexpensive but the Pulay force is computationally intensive for Gaussian-orbital methods. After obtaining all the forces acting on all the atoms a conjugate-gradient method, or other force-based algorithms, can be used to determine a new set of atomic coordinates. Once a new set of atomic coordinates is determined we find that the wavefunction expansion coefficients provide the best starting point for a calculation on this geometry. Once an equilibrium geometry and Kohn-Sham wavefunctions are determined there are many physical observables which one might be interested in calculating. These include local, total and joint electronic densities of states, polarizabilities, vibrational frequencies, infrared and Raman spectra, magnetic moments, charge states, magnetic anisotropy energies, and potential and density contour plots.

1.4.1 Calculation of vibrational properties

The forces are derivatives of the total energy with respect to the nuclear coordinates and can be computed easily from the Hellman-Feynman theorem including the Pulay corrections [31, 40]. The Pulay corrections arise from the dependence of the basis functions on the nuclear coordinates. This correction is particularly important in cases of atomic centered basis sets like the one used in NRLMOL, in contrast to a plane wave basis set where the Pulay correction vanishes. Accurate forces are an requirement for computing the vibrational frequencies. NRLMOL calculates the vibrational modes in the harmonic approximation, using a finite difference scheme of the atomic forces to build the dynamical matrix [35]. The vibrational frequencies are calculated by direct diagonalization of the dynamical matrix. This matrix is constructed by taking finite differences of both positive and negative displacements (0.05 a.u.) of the

coordinates of each atom near the equilibrium geometry and calculating the forces for each corresponding geometry. The symmetry of the cluster will be used, so that only non-equivalent geometries have to be calculated. Using this approach NRLMOL computes on average frequencies within 3% of the experimental ones, where LDA give harder and GGA softer modes.

The IR and Raman intensities are a response of the matter to an electric field. This can be described in the Kohn-Sham equation (1.5) by introducing an additional potential due to a spatially uniform, static external electric field **G**

$$V_{\text{ext}} = -e\,\mathbf{r}\cdot\mathbf{G}. \tag{1.12}$$

For finite systems like molecules it is straightforward to include an external field. The external potential V_{ext} will in general lower the point group symmetry of the molecule, which will be the only change required. This is different in case of infinite systems with periodic boundary conditions, because V_{ext} breaks the translational invariance.

The electric dipole moment μ and polarizability α_{ij} of a molecule can be defined through derivatives of the total energy with respect to the external electric field.

$$\mu_i = -\left.\frac{\partial E}{\partial G_i}\right|_{G=0} \tag{1.13}$$

and

$$\alpha_{ij} = -\left.\frac{\partial^2 E}{\partial G_i \partial G_j}\right|_{G=0} = \left.\frac{\partial \mu_i}{\partial G_j}\right|_{G=0}. \tag{1.14}$$

The electric field derivatives are computed by finite differences using δG_i= 0.005 a.u. which yields well converged values of derivatives [35]. The used field strength corresponds to 2.6 10^9 V/m, which is about two orders of magnitude larger than strong laboratory fields. Despite the fact that the applied fields are much larger than the experimental ones, the change in total energy is still very small on the order of 0.3 meV. Obtaining accurate results for IR and Raman intensities thus requires very well converged and accurate total energies.

The IR intensity depends on the change of the dipole moment and the Raman activity on the change of the polarizability with the atomic motions of the corresponding vibrational mode. Consequently, for a vibrational mode to be IR active, the dipole moment of the molecule must change as a result of the displacements. The polarizability can be related to the volume of the molecule, therefore modes that change the molecular volume tend to be Raman active. Very high numerical accuracy is needed for Raman activities, because Raman intensities involve second derivatives.

IR intensities calculated using the GGA functionals show 10-20% deviations from experimental data, weak modes are in general reproduced in correct experimental order. Strong Raman active modes are calculated with an accuracy of 20-30%.

Chapter 2

Applications

The electronic structure is a key to our understanding of chemical bonding, structural and elastic properties, vibrational spectra, electric field gradients, hyperfine fields or magnetic properties and many more.

The following sections present a few selected examples of the authors work. By using these examples the author intends to show how electronic structure calculations can be used in order to obtain a better understanding of physical and chemical properties of matter. The division into the different sections is somewhat arbitrary because many examples belong to more than one section.

2.1 The superconductor MgB_2

The announcement of the discovery of superconductivity in MgB_2 with a critical temperature of 39 K by Akimitsu at a conference in Japan in January 2001 was a great surprise for the scientific community [41]. Several hundreds papers on that single material appeared in only two years, nearly all possible experimental methods have been applied, which makes MgB_2 one of the best characterized materials. Many of its physical properties showed surprising features which called for theoretical investigation. Now, only two years later many of the unexpected physical properties, in particular the relatively high critical temperature, are well understood. This is quite different from the case of high-temperature superconductors where more than one decade after their discovery no consensus on the mechanism exists [42, 43].

The simple hexagonal unit cell with only one Mg- and two B-atoms allows for first-principles calculations without any limiting assumptions. The key for our understanding was given by the calculation of the electronic structure [44–46], which is in excellent agreement with experimental data obtained from de-Haas-van-Alphen [47] or ARPES measurements [48]. Nearly all key ideas in that field have been suggested from this kind of simulations and were then experimentally confirmed.

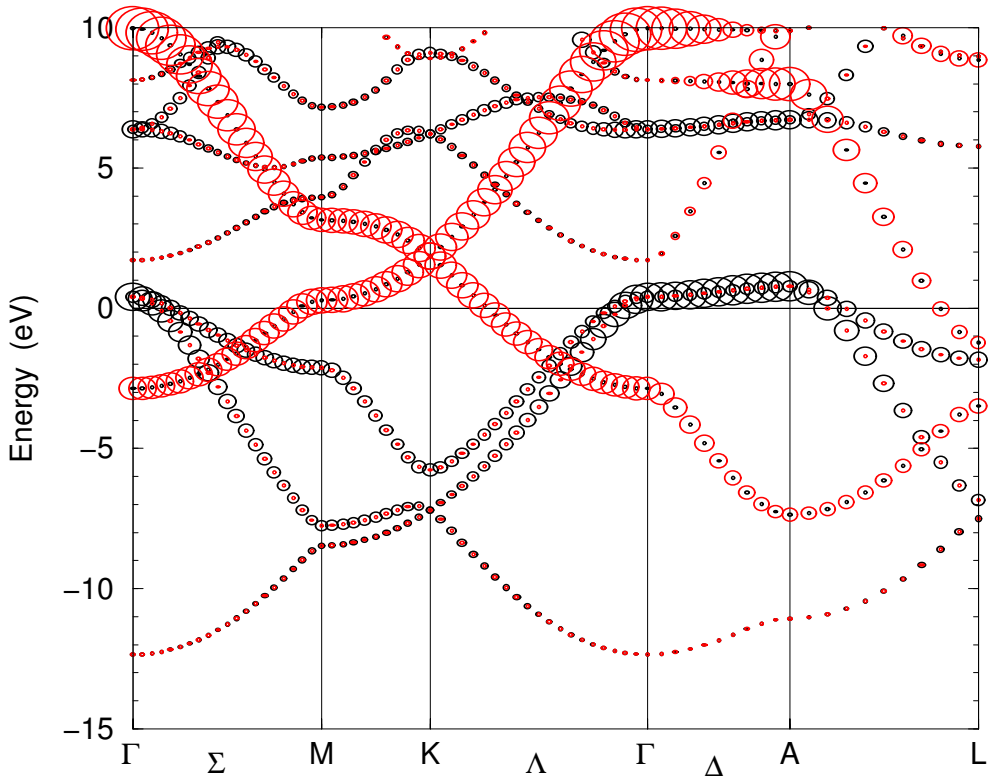

Figure 2.1: Bandstructure of MgB_2 with the B p-character. The radii of the red (black) circles are proportional to the B π (B σ) character.

MgB_2 occurs in the so-called AlB_2 structure. Borons form a primitive honeycomb lattice, consisting of graphite-type sheets stacked with no displacement. The borons form hexagonal prisms with the base diameter of 3.5Å nearly equal to the height. This creates large, nearly spherical pores for Mg. As in graphite, the intraplanar B-B bonds are much shorter than the distance between the planes, and hence the B-B bonding is strongly anisotropic.

2.1.1 Electronic structure

The energy bands and Fermi surface of MgB_2 are shown in Figure 2.1 and 2.2 and discussed in detail in Appendix A. One finds that there are no Mg states at the Fermi level. In fact, one can say that Mg is fully ionized in this compound, however the electrons donated to the system are not localized on the anion, but rather are distributed over the whole crystal. The resulting band structure can be easily understood in terms of the boron sublattice. If the boron sublattice accepts the two valence electrons from the Mg atom it becomes formally isovalent to graphene sheets. As expected, the bands are therefore quite similar to

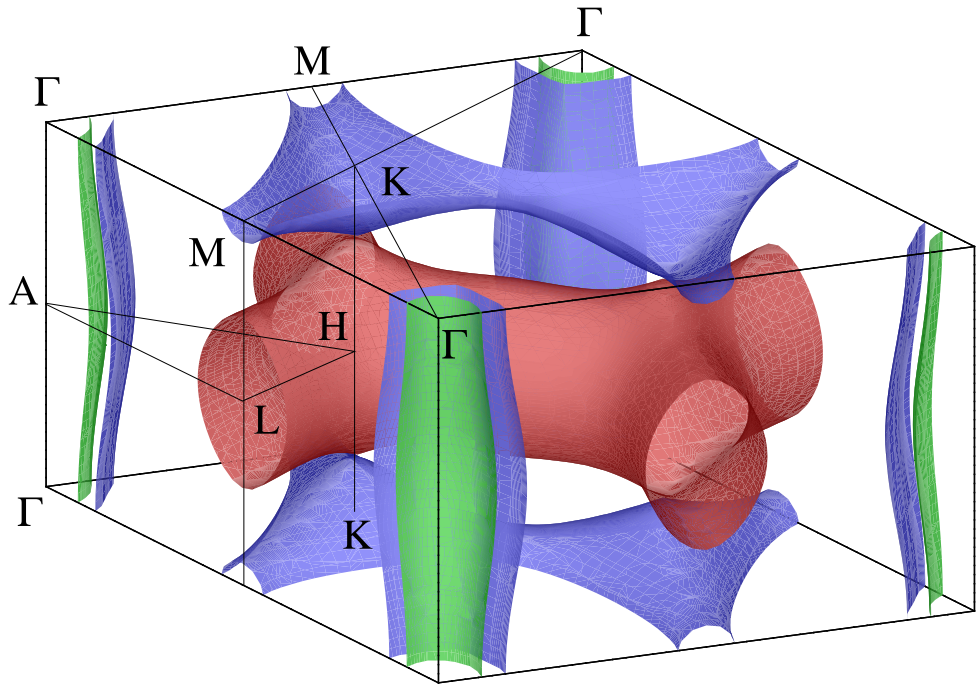

Figure 2.2: The Fermi surface of MgB_2. Green and blue cylinders (hole-like) come from the bonding $p_{x,y}$ bands, the blue tubular network (hole-like) from the bonding p_z bands, and the red (electron-like) tubular network from the antibonding p_z band. The last two surfaces touch along the K-H line.

those of graphite.

MgB_2 has two π and three σ-bands (Fig. 2.1) formed by, respectively, the two B p_z and the three bond-orbitals per cell, or, more correctly, by the corresponding Wannier-like functions. A bond orbital is the bonding linear combination of the two B sp^2-hybrids which are directed along a B-B bond. The attractive potential from the Mg^{2+} ions in the hollows between the hexagonal boron layers is felt much stronger by a p_z-electron than by a bond-electron and, as a result, the π-band is pulled so far down in energy that $\sim$0.17 holes are left at the top of the σ-band. The strong coupling of these holes to the optical bond-stretching modes is what drives the superconductivity.

The above described band structure is typical for an $sp-$metal. What is *not* typical is that this particular $sp-$metal is held together by covalent bonding with a substantial ionic component [44, 49], which inevitably leads to a strong

	Orbit	F_{calc} [T]	m_{calc}	λ	$m(\lambda)_{\text{calc}}$	F_{exp} [T]	$m(\lambda)_{\text{exp}}$
1	σ Γ-plane	728	-0.245	1.25	0.551	540	0.54
2	σ^* Γ-plane	1605	-0.530	1.16	1.145		
3	π Γ-plane	34630	1.96	0.43	2.763		
4	σ A-plane	1756	-0.312	1.25	0.702	1530	0.66
5	σ^* A-plane	3393	-0.618	1.16	1.335		
6	π^* Γ-plane	31130	-1.00	0.47	1.470		
7	π ΓAM-plane	458	-0.246	0.43	0.352		
8	π^* ΓAM-plane	2889	0.315	0.47	0.463	2685	0.45

Table 2.1: Calculated de Haas-van Alphen parameters from Appendix B (F_{calc}) compared to the experimental data (F_{exp}) of Ref. [47]. The electron-phonon coupling constant λ has been computed from Tables 1 and 2 of Ref. [45]. $m(\lambda) = |(1+\lambda)m|$ is the thermal mass renormalized by the electron-phonon coupling λ. All masses are in units of the bare electron mass.

electron-phonon interaction.

It may be seen in Figure 2.2 that the π bands form two tubular networks: an antibonding electron-type sheet centered at $k_z = \pi/c$ (red) and a similar bonding hole-type sheet centered at $k_z = 0$ (blue). In contrast to graphite the σ-bands are filled incompletely. They have only a small k_z dispersion along the Γ-A line (see Figure 2.1) and form two nearly cylindrical Fermi surface sheets along the Γ-A line. The holes in the σ-bands are very unusual, in fact MgB_2 seems to be the first material for which this has been observed. These holes are of the utmost importance in order to understand the superconductivity in $MgB2_2$.

2.1.2 de Haas-van Alphen effect

Historically, the most reliable probe of the bulk electronic structure has been the de Haas-van Alphen effect (dHvA) [50]. Recent observation of this effect in MgB_2 single crystals [47] provides key information to assess the validity of the standard band structure calculation. Given the fact that most theoretical papers rely on this band structure, the importance of a proper analysis of these data can hardly be overestimated.

The Fermi surface of MgB_2 consists of four sheets (Figure 2.2). Two sheets are formed by boron σ-bands primarily, and are shaped as slightly (nearly sinusoidally) warped cylinders, σ (bonding) and σ^* (antibonding), and two tubular networks, the bonding one, π, in the Γ ($k_z = 0$) plane, and the antibonding one, π^*, in the A ($k_z = \pi/c$) plane. There are 6 extremal dHvA cross-sections for the field parallel to k_z (along the $\Gamma-$A line), namely:

1. σ in the Γ plane,
2. σ^* in the Γ plane,
3. π in the Γ plane ("holes" between the tubes),
4. σ in the A plane,
5. σ^* in the A plane,
6. π^* in the A-plane.

For a field parallel to k_y (perpendicular to the $\Gamma-$AM plane) there are two extremal cross-sections (tubes' necks), for the π surface (7) and for the π^* surface (8).

The agreement between the calculated and measured thermal masses (see Table 2.1) can be characterized as excellent. Very importantly, this agreement is so good only because the calculated electron-phonon coupling differs by a factor of 3 between the σ and π bands. This is the first direct demonstration of this important effect. The agreement between the calculated areas F and the experimental ones is good, but not outstanding. F_1, F_2 and F_3 are overestimated by 35%, 15%, and 8%, respectively. The first number indicates that the calculations underestimate the k_z dispersion: the F_1 and F_2 ratio measures the degree of the warping of the σ cylinder. In fact, shifting the σ band by 6 mRy up in the Γ plane and by 1 mRy up in the A plane, and the π^* band by 6 mRy down brings the calculated areas to full agreement with the experiment.

This observation does not mean that we try to enhance agreement with experiment by adjusting the Fermi level. The discrepancies between experiment and theory are less than 300 T, which corresponds to only 0.2% of the area of the hexagonal Brillouin zone. Therefore, the difference itself is not large and will result only in quantitative corrections in the description of MgB_2 but will not change the qualitative picture. Similar shifts of the Fermi level which would bring the experimental and calculated areas to better agreement have also been noted by Rosner *et al.* [51].

2.1.3 Angle resolved photoemission spectroscopy

While at the dawn of electronic structure calculations it was not believed that the electronic bands themselves will be a measureable quantity, progress in experimental technique proved that to be wrong. Angle resolved photo emission spectroscopy (ARPES) allows for the detection of occupied bands close to the Fermi level. The electronic structure of several metals such as Cu or Ag has been probed by photoemission [52, 53] in good agreement with electronic structure calculations.

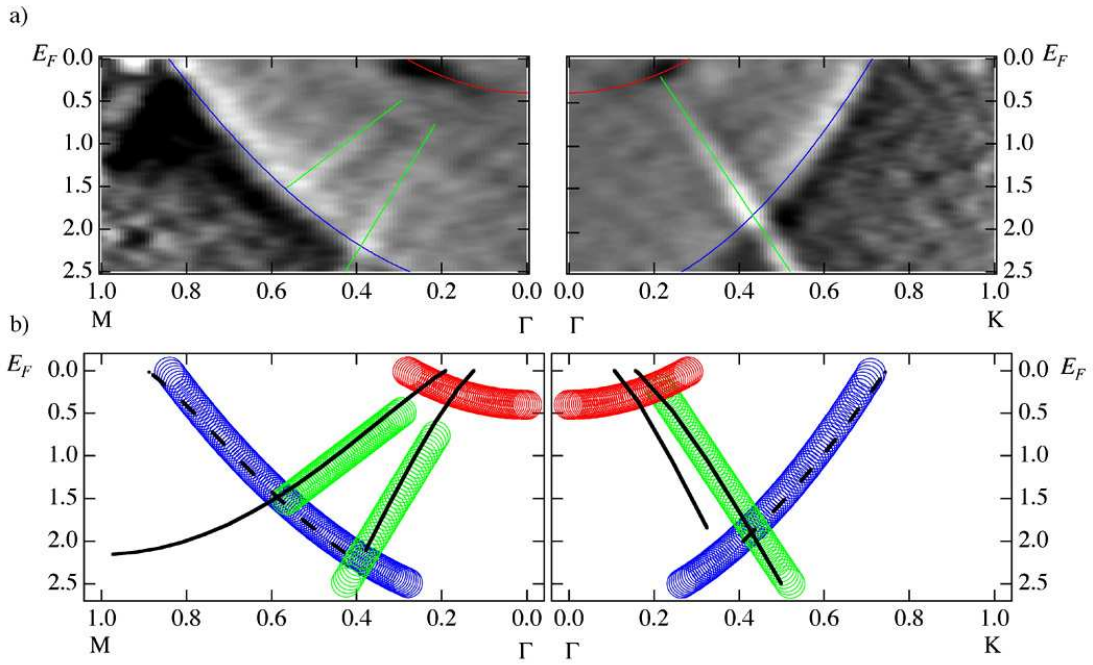

Figure 2.3: The measured ARPES spectra [48] compared with the band structure calculated by the author (lines).

Figure 2.3 shows the experimental ARPES from single crystals of MgB_2 [48] compared with band structure calculations of the author of this work. Both the π and σ bands were observed along the Γ-M direction in excellent agreement with the theoretical predictions. The dispersion along Γ-K shows only one of the two σ bands, were the authors of [48] speculated that this is due to a superpostion of the two bands which could experimentally not be resolved. Although, due to different symmetries along the two measured directions different selection rules may influence the transition matrix elements. The parabolic feature around Γ with a minimum 0.5 eV below the Fermi energy has been identified as a surface state [54].

In summary, ARPES and dHvA experiments in MgB_2 both fully support the DFT calculations, which leaves practically no room for electron-electron correlation or manybody renormalization of the band masses and Fermi velocities. This already gives strong support for a more conventional picture of superconductivity driven by the electron-phonon coupling, because it makes several more exotic theories [55, 56] rather unlikely.

2.1.4 X-ray spectroscopy

X-ray emission and absorption spectroscopies are also powerful probes of the electronic structure of solids. Photon emission and absorption involve a transition between electronic states. In the soft x-ray regime, one of the states is a localized, dispersionless core level. This allows for the interpretion of the measured spectra in terms of unoccupied states for absorption and occupied states for emission. Since dipole selection rules govern the transitions to or from the core level, it is actually the angular-momentum-resolved density of states that is measured. Furthermore, since the core level is associated with a specific element in the compound, x-ray absorption and emission are also element specific. Finally, they have the advantage of being relatively insensitive to the quality of the sample surface, unlike x-ray photoelectron spectroscopy (XPS) or ultraviolet photoemission, where in order to measure the bulk electronic structure it is necessary to prepare atomically clean, stoichiometric, and ordered surfaces.

Using the full potential LAPW code WIEN97, [57] the author calculated the near edge absorption and emission X-ray spectra. According to the final-state rule formulated by von Barth and Grossmann, [58] accurate X-ray emission and absorption spectra of simple metals may be obtained from ordinary one-electron theory if the relevant dipole matrix elements are calculated from valence functions obtained in the potential of the final state of the x-ray process: in other words, a potential reflecting the fully screened core hole for absorption but not for emission. Because we neglected core relaxation effects in our calculations, we expect significantly better agreement between theory and experiment for emission spectra. The calculated spectra are Lorentz broadened with a spectrometer broadening

As shown in Appendix C, the measured x-ray emission and absorption spectra of the constituents of the superconductor MgB_2 are found in good agreement with results of band structure calculations and in particular calculations of intensities of x-ray spectra taking the necessary matrix elements into account. Further, according to the experimental findings magnesium is positively charged in this compound, which supports the results of electronic structure calculations. The comparison of x-ray emission spectra of graphite, AlB_2, and MgB_2 supports the idea of superconductivity driven by hole doping of the covalent σ bands.

2.1.5 What is special about MgB_2?

The previous sections discussed only the electronic structure of MgB_2 in some detail together with several experiments which are able to probe this electronic structure. Although, there are many more interesting features of this material which are outside the scope of the present work. Most importantly, all aspects of superconductivity are not mentioned here.

More than forty years ago Suhl, Matthias, and Walker predicted the existence of *multigap* superconductivity, in which a disparity of the pairing interaction in different bands, such as the s- and d-bands in transition metals, leads to different order parameters and to an enhancement of the critical temperature [59]. Despite much effort, a clear materialization of this phenomenon was not found, neither in transition metals, nor in novel transition-metal compounds, such as $YBa_2Cu_3O_7$ or Sr_2RuO_4. The material MgB_2 appears to be the first superconductor, for which a two-gap model [45, 60] offers a simple explanation of many anomalous experimental findings.

Recent experimental data from scanning tunneling measurements and point-contact spectroscopy [61–63], high-resolution photo-emission spectroscopy [64], Raman spectroscopy [65], specific heat measurements [66] and muon spin relaxation studies of the magnetic penetration depth [67] support the concept of a double gap in MgB_2 (see Ref. [68] for a review of experiments).

For the sake of completeness a short summary of what makes MgB_2 so exciting is given. For detailed information of the authors work in the field of MgB_2 please see [44, 45, 69–76].

- There are holes at the top of the sp^2-bonding σ-bands.
- These holes couple strongly to the optical bond-stretching modes with $q < 2k_F$.
- Since k_F is merely 1/5 of the Brillouin zone radius, very few electrons and very few phonons contribute to the electron-phonon coupling constant $\lambda_{\sigma\sigma} \simeq 1$.
- Since the σ-holes couple stronger to the phonons than the π-electrons, there are two distinct superconducting order parameters.
- The critical temperature T_c is enhanced by the anisotropy of the gap.
- These effects are visible only because impurity $\sigma - \pi$ band scattering is negligible, except in severely damaged samples.
- Multiband effects are very important also in the normal state transport and thermodynamical properties .

2.2 Electric field gradients

Electric field gradients (EFG) are determined by the non-spherical contributions of the electronic charge density around a nucleus. Therefore, one can see the efg has a sensitive probe of the quality of electronic structure calculations. While the calculation of EFG has been already implemented for some time in

DFT codes like WIEN97 [57], it has been only recently implemented in the NRLMOL package by Jackson and Kortus [77]. Here we will give a few details and benchmark calculations for that implementation.

The EFG is due to the electrons and the other nuclei in the material. The EFG at nucleus X can be calculated as:

$$V^X_{\alpha,\beta} = \int d\mathbf{r}\rho(\mathbf{r})\frac{[3(r_\alpha - R_{X\alpha})(r_\beta - R_{X\beta}) - |\mathbf{r}-\mathbf{R}_X|^2\delta_{\alpha,\beta}]}{|\mathbf{r}-\mathbf{R}_X|^5} \quad (2.1)$$

$$-\sum_Y \frac{Z_Y 3(R_{Y\alpha} - R_{X\alpha})(R_{Y\beta} - R_{X\beta}) - |\mathbf{R}_Y - \mathbf{R}_X|^2\delta_{\alpha\beta}}{|\mathbf{R}_Y - \mathbf{R}_X|^5} \quad (2.2)$$

where $\rho(\mathbf{r})$ is the electronic charge density at position $\mathbf{r}$, the $\mathbf{R}$'s represent the positions of the nuclei and the Z's the corresponding atomic numbers. To evaluate $V^X_{\alpha,\beta}$, we compute the first integral numerically, and add the second term, which is a simple sum over the nuclei.

The Mössbauer quadrupole splitting arises from an interaction between the nuclear quadrupole moment and the EFG at the position of the Mössbauer nucleus. The quadrupole splitting for a $I = 3/2$ state is given by:

$$\Delta = eQV_{zz}\sqrt{(1+\eta^2/3)}/2 \quad (2.3)$$

where Q is the nuclear quadrupole moment, V_{zz} is the largest eigenvalue of the EFG tensor and η is the asymmetry parameter,

$$\eta = \frac{V_{yy} - V_{xx}}{V_{zz}} \quad (2.4)$$

Here the principle axes are chosen such that $|V_{zz}| \geq |V_{yy}| \geq V_{xx}$.

To test the reliability of our DFT approach, we have computed EFG components for several benchmark molecules that were studied recently using *ab initio* methods. In Table 2.2 we show a comparison of our DFT NRLMOL results and the corresponding values obtained at the Hartree-Fock (HF) and Møller Plesset second order perturbation theory (MP2) levels of theory [78]. The table shows the value of V_{zz} at each nucleus in the molecule, in atomic units. The *ab initio* results were obtained using extensive basis sets. The DFT results are reported for the default basis sets implemented in NRLMOL. The table shows very good agreement between the different methods. Typical differences between DFT and MP2 results are on the order of 10% or less. We tested the DFT results for basis set effects by recomputing the EFG components using extended basis sets, including additional diffuse single Gaussian orbitals for all angular momentum types. As shown in Table 2.2, the EFG parameters change only slightly with the larger basis.

Coming back to the solid state, the very delicate interplay between structural parameters and EFG in wurtzite semiconductors is discussed in Appendix

		ab initio		DFT	
		HF-SCF	MP2	default	extended
H_2		-0.342	-0.338	-0.350	-0.388
N_2		1.368	1.115	1.153	1.112
F_2		-6.944	-6.258	-6.516	-6.343
HF	H	-0.521	-0.546	-0.566	-0.538
	F	-2.860	-2.591	-2.788	-2.720
HCl	H	-0.293	-0.296	-0.294	-0.296
	Cl	-3.579	-3.402	-3.458	-3.469
CO	C	1.174	0.950	0.979	0.939
	O	0.724	0.779	0.705	0.684
HCN	H	-0.317	-0.319	-0.334	-0.322
	C	0.498	0.376	0.370	0.339
	N	1.201	0.946	1.008	0.979
HNC	H	-0.419	-0.421	-0.443	-0.424
	N	1.035	0.833	0.864	0.834
	C	-0.017	-0.048	-0.116	-0.130
H_2O	H	-0.472	-0.481	-0.501	-0.477
	O	1.836	1.624	1.763	1.713
NH_3	H	-0.392	-0.391	-0.407	-0.390
	N	0.957	0.838	0.973	0.941

Table 2.2: A comparison of calculated electric field gradient (EFG) parameters using *ab initio* (Ref. [78]) vs DFT NRLMOL results. The values quoted for each molecule represent V_{zz}, the largest eigenvalue of the EFG tensor, at the various atom positions shown. Values are quoted in atomic units. The *ab initio* results were obtained using extensive basis sets. The NRLMOL results are given for the default electronic structure basis sets and for an extended basis.

D. The wurtzite structure consists of two close packed sublattices which are displaced along the c direction by uc. There is a strong dependence of the A- and B-site EFG on this internal u parameter. A small change of u (0.2%) results in a large relative change (50%) of the EFG values at the A-site. For given hexagonal lattice parameters a and c one can determine a theoretical u parameter from minimization of the total energy. Theoretical values of u have been calculated for AlN, ZnO, CdS, GaN and ZnS. These values follow a linear dependence on the c/a ratio in agreement with earlier observations [79]. The experimental uncertainty of u from X-ray data could be minimized by checking the theoretical values against the measured and calculated EFG. A good agreement of the EFG would give direct experimental support for the theoretical u value.

2.3 Vibrational properties

This section will be mainly devoted to the discussion of vibrational properties which can also be obtained from DFT calculations. The examples include a naturally occurring mineral: melanophlogite, which is iso-structural to the type I gas hydrates. The guest host interaction in this clathrate significantly influences the Raman modes and their intensity. The other two examples are more chemical oriented and describe the vibrational properties of two high-energy molecules: octanitrocubane and azidopentazole. While the first one has been already synthesized the other one is still elusive. In case of octanitrocubane we discuss the interesting case of a failure of the usually used harmonic approximation.

2.3.1 Host guest interaction in a clathrate

Melanophlogite is a naturally occurring SiO_2-based clathrate structure which has the same structure as type I gas hydrates. Two types of voids are found in melanophlogite (Figure 2.4 and 2.5). The SiO_4 tetrahedra of the host form a three-dimensional framework consisting of two different kinds of cages. In fact, melanophlogite was the first known example of a silicate framework structure with the pentagonal dodecahedron as a framework element [80].

This framework contains two types of cages: two pentagondodecahedra (cage I) and six tetrakaidecahedra (cage II) per unit cell. The structure of the smaller cage I shown in Fig. 2.4 is well known from recent interest in carbon fullerenes. It is the natural occurring equivalent of silica to a C_{20} fullerene. However, due to the tetrahedral coordination preferred by Si atoms the cages share faces to satisfy the sp^3 bonding. The corners are occupied by silicon atoms, whereas the oxygen atoms are located on the middle of the edges. The free space within cage I can be approximately described by a sphere-like void with diameter $d \sim 5.7$ Å and a volume $V \sim$97 Å^3.

The structure of cage type II is presented in Fig. 2.5. The top and bottom faces are hexagons and the remaining faces are pentagons. The free space inside can be approximated by an ellipsoid with $d_1 \sim d_2 \sim$5.8 Å, $d_3 \sim 7.7$ Å and a volume of 136 Å^3. An interesting feature of cage II is how the stacking of cages lead to nanotube like structures, which may contain long chain-like molecules. The entire crystal structure may also be described as a three-dimensional array of stacked cages of type II.

Further, as in the case of the gas hydrates, melanophlogite traps gas molecules within the voids. This silica polymorph usually contains several guest molecules (e.g. CH_4, N_2 and CO_2) in varying amounts. In Appendix E we present a joint theoretical and experimental investigation of the CH_4 Raman spectra associated with the enclathrated CH_4 molecules.

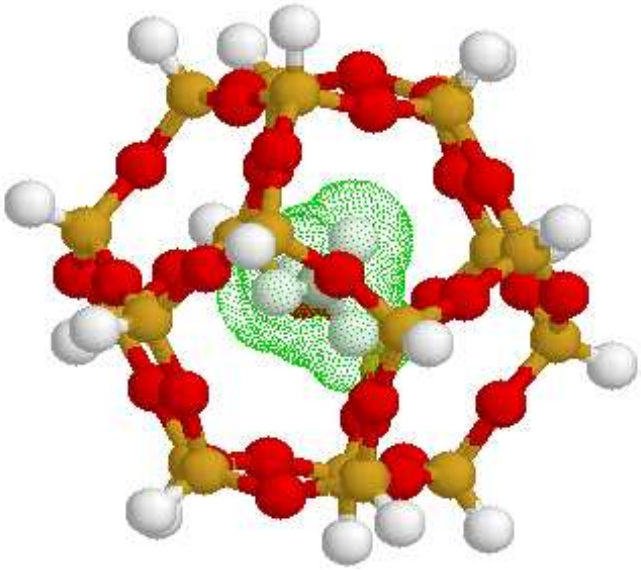

Figure 2.4: Cage I (pentagon dodecahedra) consists of 12 pentagonal faces. It is the natural occurring equivalent of silica to a C_{20} fullerene. The atoms on the corners are silicon atoms (lighter balls), whereas the atoms between are oxygen atoms (dark). The broken bonds are saturated by hydrogen atoms (very light balls). The guest molecule (methane) located inside this cage is presented too.

Raman spectroscopy provides a non destructive method for obtaining information about the kind of guests by observing their vibrational fingerprints. Further, if the Raman activity of the guest molecules is known, the density of the guests may be determined. Since, density-functional calculations provide a cost-effective *ab initio* means for determining the Raman activity of molecules the two methods combined give us a powerful tool for analyzing and characterizing the above mentioned structures.

We find that the Raman intensities of the totally symmetric hydrogen stretch modes are significantly perturbed by the presence of the clathrate cage and show that the calculated Raman spectra may be used to determine the concentration and location of the enclathrated gas molecules. Relative to the gas-phase structure we identify two effects which are responsible for the change in intensity of the enclathrated molecules relative to the gas phase. The polarizability of the surrounding cage acts to increase the Raman spectra of the stretch mode in the pentagondodecahedra cage. However, in the lower-symmetry tetrakaidecahedra cage, mixing between the hydrogen-stretch mode and other optically silent molecular vibrations counteracts this affect and accounts for the different Raman intensities observed for the two types of voids.

We suggest that similar calculations and experiments on the gas-hydrates

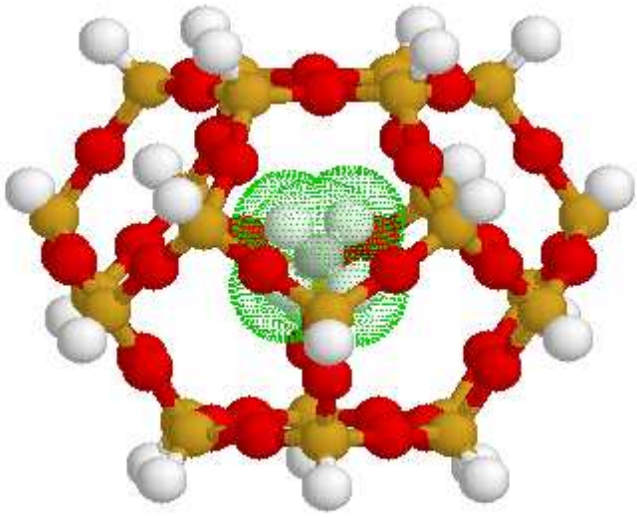

Figure 2.5: Cage II (tetrakaidecahedra) has two hexagonal faces on the top and bottom, remaining with 12 pentagonal faces. The atoms on the corners are silicon atoms (lighter balls), whereas the atoms between are oxygen atoms (dark). The broken bonds are saturated by hydrogen atoms (very light balls). The guest molecule (methane) located inside this cage is presented too.

may provide an in situ diagnostic tool for determining the amount of natural gas contained within the gas-hydrates on the sea floor.

2.3.2 Octanitrocubane

The well-known molecule cubane (C_8H_8), which was first synthesized by Eaton and Cole [81], is build from a cube of carbon atoms saturated with hydrogen atoms at each corner.

It has been suggested that cubane can be made more energetic by replacing its H atoms with nitro (NO_2) groups. [82,83] In fact, Zhang, Eaton, and Gilardi [84] have recently synthesized octanitrocubane (see Figure 2.6) where all the hydrogen atoms have been replaced by nitro groups.

In Appendix F we present an first-principles calculation of the optimized geometry of octanitrocubane, its molecular orbital energies and vibrational spectra. We show that the molecule, while stable, allows for large torsional displacements of the nitro groups and would release large amounts of energy upon dissociation into molecular N_2 and CO_2. Because octanitrocubane is significantly more electronegative than cubane there is the possibility of cation induced stabilization of the crystal through selective doping. The calculated infrared and Raman spectra should be useful in determining the presence of octanitrocubane and in confirming the symmetry lowering which apparently

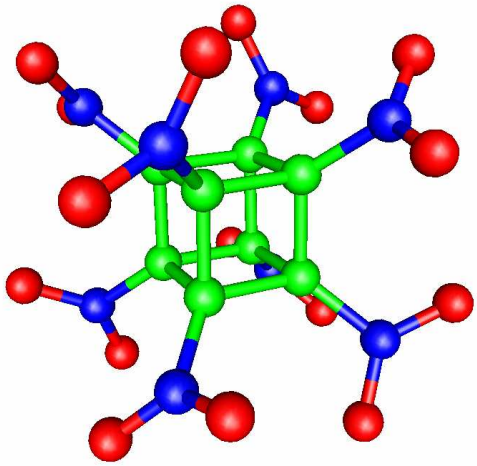

Figure 2.6: The molecular structure of octanitrocubane. The carbon atoms form a cube to which the nitro groups are connected on the corners.

occurs in the solid structure.

Further, one of the very soft torsional modes exhibits strong anharmonicity and is fundamentally interesting. This extremely soft concerted torsional vibration is associated with the rotation of NO_2 groups about the C-N bond axes. Interestingly, at the harmonic level we find a total of eighty-nine real frequencies and *seven* zero-frequency modes. While six of the zero-frequency modes correspond to the usual rotational and translational modes, the seventh zero-frequency harmonic mode requires a more in-depth discussion. For reasons that will become clear below, we refer to this mode as the quartic concerted torsional mode (QCTM) throughout the remainder of the discussion.

We start by noting that the harmonic analysis shows that this mode is entirely associated with torsional rotations of pairs of oxygen atoms about their respective C-N bonds. Finally, we note that we have performed frozen vibron calculations for both the energy and the force as a function of the displacement of that mode and the resulting potential energy curve is shown in Fig. 2.7. A detailed analysis of both the energy and forces as a function of the QCTM displacement confirms that the second derivative and all odd derivatives of this mode vanish identically.

In addition to the classical potential observed by the torsional mode, we

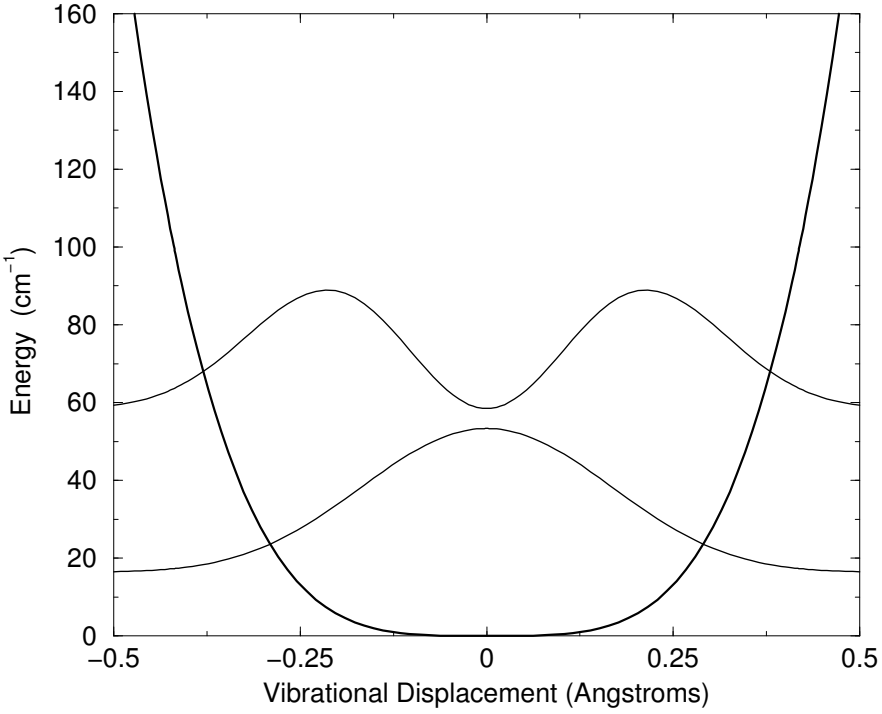

Figure 2.7: Potential as a function of vibrational displacement observed by the QCTM. Also included are the squares of the lowest eigenmodes of this predominantly quartic potential. The energy intercepts of the eigenmodes are shifted by their respective energies which shows a zero point energy of 16 cm^{-1} and a lowest excitation energy of 42 cm^{-1}.

have determined the anharmonic vibrational wavefunctions and energies associated with this mode and present the results in Fig. 2.7. Because of the quartic nature of the potentials, the anharmonic wavefunctions are flatter than what would be expected from a harmonic oscillator potential. The zero point energy associated with this mode is found to be 16.4 cm^{-1} and the first excited state is found to be 58.5 cm^{-1}, suggesting that the lowest observable excitation would be observed at 42 cm^{-1}. Because this mode is anharmonic, it might be detected by looking for second-harmonic generation in the Raman spectra which, according to our calculations, should occur at 102.1 cm^{-1}. Unfortunately, there are other strong Raman active modes which appear at both of these energies.

Since the potential associated with the QCTM is convex and since all other harmonic modes exhibit real frequencies, the symmetry of the molecule studied here corresponds to a locally stable geometry for the free molecule. To address the question of global stability we have performed calculations on two other reasonable symmetries of the molecule and have found that these symmetries lead to higher energies.

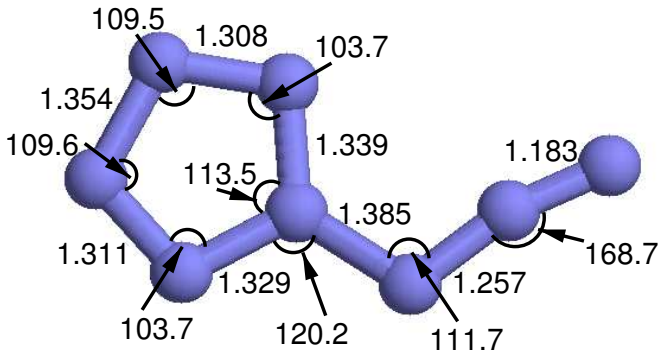

Figure 2.8: Optimized geometry of the ground state of azidopentazole which has C_s symmetry with the PBE gradient-corrected density functional. The bond lengths are given in Å and the angles in degrees.

2.3.3 Azidopentazole

Azidopentazole (N_8) is a polynitrogen high-energy molecule whose structural geometry is characterized by a five-membered ring with a three-atom nitrogen tail (see Figure 2.8). While this molecule has not yet been synthesized, there have been a number of theoretical calculations in the literature on the electronic and structural properties of azidopentazole.

Despite this possible limitation on its long-term stability, we still believe that azidopentazole is a possible candidate for a novel polynitrogen molecule, especially in light of the newly discovered N_5^+ cation by Christie *et al.* [85]. We report in Appendix G a first-principles all-electron density functional theory study of the electronic, structural, and vibrational properties of azidopentazole, in its ground state. While a structural optimization and vibrational analysis of azidopentazole have been previously reported in the literature [86–89], only calculated IR intensities have been reported [86]. The calculated bond lengths and bond angles are within 0.1Å and 1°, respectively, of the B3LYP/6-31G* results of Glukhovtsev, Jiao, and Schleyer [86]. This excellent agreement can be seen as a test of the accuracy of the PBE functional used in our work in comparison to the more commonly used functionals in quantum chemistry.

The results described in Appendix G include both a detailed analysis of the calculated IR spectra as well as a discussion of the predicted Raman spectra and their intensities. We hope that this information on the vibrational properties of azidopentazole will assist future experimental work in characterizing this elusive high-energy polynitrogen species.

2.4 Magnetic ordering

This section starts the discussion of magnetic properties of molecules and clusters, one of the main research interests of the author. In this section the author will focus on systems which are not single molecule magnets, which will be discussed more extensively in the last part of the present work. The first example discusses an exhaustive investigation of magnetic order and vibrational properties of an iron oxide cluster, which has been found recently in the gas phase. The second one is more concerned with the influence of alloying Fe and Co on the magnetic properties.

2.4.1 Magnetic and vibrational properties of the $Fe_{13}O_8$ cluster

Recently, Wang *et al.* [90] synthesized a new iron oxide cluster by reactive laser vaporization. From time of flight mass spectra and first-principles calculations [90, 91] they respectively concluded that this iron oxide cluster consists of 13 iron and 8 oxygen atoms with D_{4h} symmetry. Wang and coworkers [90] have emphasized the need for understanding the Fe-O interactions because of the role that such interactions play in corrosion, biological processes and oxide film formation.

Because of the coupling of the magnetic and structural degrees of freedom, consideration of ferro- ferri- and antiferromagnet ordering is an important issue from the standpoint of determining the ground state of a magnetic molecule. As such, the investigation of different possible spin orderings as well as total moments were the primary aims of the work in Appendix H. For the energetically most stable structure obtained we calculated the vibrational spectra which clarified some questions raised by the reported values of Sun and coworkers [91].

A way to determine whether a magnetic state is at least meta-stable is to examine the highest occupied molecular orbital (HOMO) and lowest unoccupied molecular orbital (LUMO) levels of the majority and minority spin. The spin gaps, defined as

$$\Delta_1 = -(\epsilon^{\text{maj}}_{\text{HOMO}} - \epsilon^{\text{min}}_{\text{LUMO}}) \quad (2.5)$$

$$\Delta_2 = -(\epsilon^{\text{min}}_{\text{HOMO}} - \epsilon^{\text{maj}}_{\text{LUMO}}), \quad (2.6)$$

correspond to the energy required to transfer an infinitesimal amount of charge from the HOMO of one spin to the LUMO of the other one. The system can only be magnetically stable if both spin gaps are positive. Further, if the spin gaps are not both positive they determine whether an increase or decrease of total moment will stabilize the system.

Within the constraint of the D_{4h} symmetry we performed a rather exhaustive search of the possible ferromagnetic states. First, using D_{4h} symmetry we

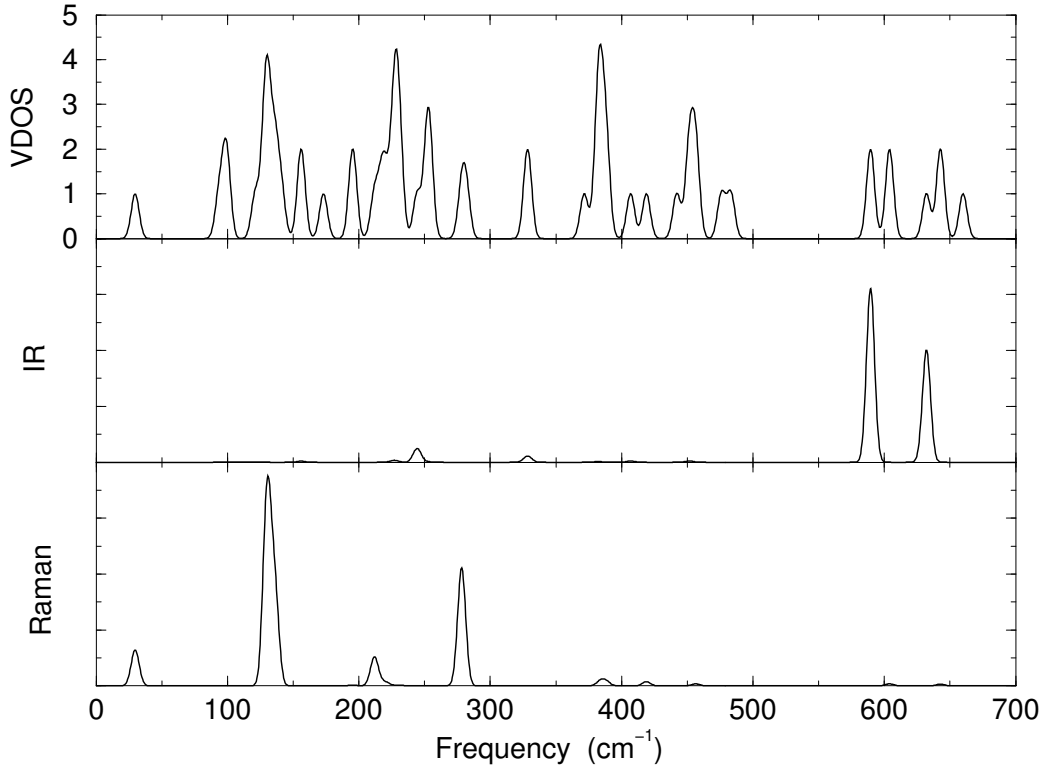

Figure 2.9: The upper panel displays the calculated vibrational density of states (VDOS), the middle the IR spectra and the lower panel the Raman spectra of the most stable ferromagnetic iron oxide $Fe_{13}O_8$ cluster with D_{4h} symmetry. The lowest frequency is 29.7 cm^{-1}. The IR and Raman intensities are in arbitrary units, a constant line width of 6 cm^{-1} was assumed.

optimized the geometry of the cluster with a ferromagnetic state corresponding to a total moment of 20 μ_B. Both spin gaps, $\Delta_1 = 0.516$ eV and $\Delta_2 = 0.012$ eV, are positive, which show that this state is at least meta-stable. However, Δ_2 is small, indicating that another ferromagnetic state obtained by transferring charge from the minority spins to the majority ones could also lead to a meta-stable state. Starting from this geometry we carried out 16 different calculations with fixed total moments of the cluster ranging between 20 μ_B and 52 μ_B. Using the above defined criteria of positive spin gaps for both spins we determined the magnetically meta-stable configurations for which we further optimized the geometry within the constraint of this given moment. In some cases one of the spin gaps became negative during the geometry optimization. In theses cases we changed the moment accordingly and relaxed the geometry further. This approach resulted in the identification of four meta-stable ferromagnetic states with total moments of 20 μ_B, 26 μ_B, 32 μ_B and 34 μ_B. The

magnetic states with 32 μ_B and 34 μ_B were found to be the most stable ones. These states are energetically nearly degenerate with the 34 μ_B state only 3 meV higher in energy. The most stable structure found, was the state with 32 μ_B.

If orbitals are spatially orthogonal and occupy the same region in space, parallel alignment of the spins leads to a larger exchange interaction energy and ferromagnetic coupling is subsequently favored. Antiferromagnetic coupling occurs in cases where the orbitals are spatially separated but nonorthogonal. In such cases anti-parallel alignment of the spins bypasses the need for spatial orthogonality and provides for a reduction in the kinetic energy.

Using the same approach as in the ferromagnetic case we started with 12 different fixed total moments between 0 μ_B and 20 μ_B. We find antiferromagnetic and several ferrimagnetic states with total moments 4, 8, 10, 12, 13, 14 and 15 μ_B to be meta-stable magnetic states for the iron oxide cluster. The ferrimagnetic states with 12, 13, 14 and 15 μ_B have two-fold states at the Fermi level, which are not fully occupied suggesting that Jahn-Teller distortions would lead to a reduction in symmetry.

All these states are close in energy and show similar behavior. The magnetic state with 14 μ_B is the lowest energy state exhibiting antiferromagnetic coupling between the Fe atoms. However, this state is 86 meV higher in energy than the ferromagnetic state with 32 μ_B .

In Figure 2.9 we show the vibrational spectra including IR and Raman intensities calculated from density-functional theory. We find that the ferromagnetic state with a moment of 32 μ_B per cluster is locally stable. Our frequencies range from 29.7 cm^{-1} as the lowest to 660 cm^{-1} as the highest frequency. These values differ by an order of magnitude from the frequencies given by Sun and coworkers. [91] A good test for the numerical accuracy of our calculations is the value of the trivial frequencies of the three translational and rotational modes which should be zero, which we also obtain from diagonalizing the dynamical matrix. The largest absolute value for one of these six modes is 0.000012 cm^{-1}.

2.4.2 Magnetic moment and anisotropy in Fe_nCo_m clusters

Appendix I presents electronic structure calculations on Fe_nCo_m (n+m=5 and 13) clusters in order to examine the effect of alloying on the magnetic moment and magnetic anisotropies.

In Fig. 2.10 we show the configurations studied in this work. The 5- and 13-atom clusters are chosen because they allow for uniaxial structures. For each of the pure uniaxial configurations it is possible to further enhance the uniaxial character via substitution of different transition metal atoms along the axis of symmetry. This procedure allows for iron-rich uniaxial clusters with compositions Fe_3Co_2, and $Fe_{10}Co_3$. Similar cobalt-rich uniaxial clusters with opposite

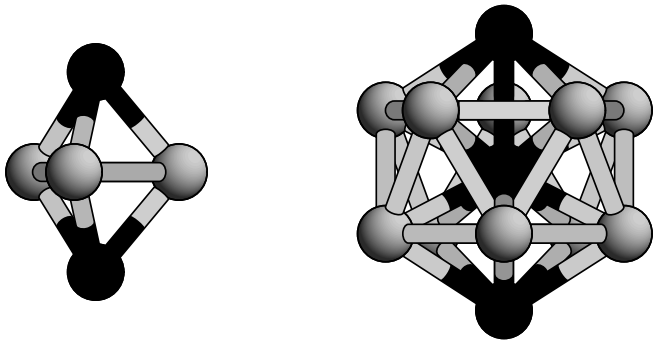

Figure 2.10: The uniaxial geometrical configurations studied here include triangular bipyramid geometries (N=5) and distorted icosahedrons (N=13). For the mixed clusters the dopant atoms were placed along the uniaxial axis as indicated by the darker atoms.

stoichiometries are also studied here. For the smaller clusters ($N = 5$), the uniaxially symmetric stable geometries have been further optimized for these stoichiometries with no symmetry constraints in order to find the influence of geometry on the magnetic anisotropy energy.

The density-functional studies show that many mixed clusters have moments comparable to or higher than the pure clusters. The anisotropy energy changes nonmonotonically with geometry and size. We show that shape, composition and compositional ordering must be considered for optimization of anisotropy energies. Phenomenological models where one uses the bulk anisotropy constants for determining the anisotropy energy in clusters may be deficient at small sizes. In addition to size, shape, composition and geometry, we have shown that the magnetic anisotropy in clusters can depend sensitively on temperature.

2.5 Molecular magnets

Magnetic materials play a very important role in todays information technology. In order to increase the capacity for information storage, the system size of the storage devices must be decreased and this eventually suggests the need for transitioning from bulk matter to nanoscale molecules and clusters.

The magnetic molecules of current interest are typically composed of one or more transition metal atoms which are locked at their lattice sites by a carefully arranged host consisting of organic molecules and ligands. The molecules in the solid phase may be characterized by very weak interactions between the molecular entities, so that the magnetic behavior probed by experiments will be determined by that of a single molecule.

In this size regime the temperature at which a magnetic device will retain its magnetic orientation is determined by the magnetic anisotropy energy (MAE) which is due to directional dependencies of the spin-orbit-coupling operator. Further, quantum physics becomes important as evidenced by the phenomenon of quantum tunneling of magnetization (QTM) [92]. In QTM, the hysteresis loops in the macroscopic samples of molecular magnets containing the clusters show discrete steps related to the quantum jump of the magnetization in different directions. Magnetic molecular clusters such as the manganese-oxo cluster with acetate ligands (Mn_{12}-ac) [93, 94] or the octanuclear iron(III) oxo-hydroxo cluster (Fe_8) [92, 95] are probably the most widely studied materials for which QTM has been observed [96–99]. Another very interesting cluster is the V_{15} spin system [100]. Besides the fundamental interest in understanding quantum effects in these nanomagnets they might be also relevant for implementations of quantum computers.

In general the properties of a nanoscale system of coupled spins depend directly on the strength of the exchange-parameters and on the strength of the spin-orbit coupling. When the exchange interactions are large enough, the lowest energy magnetic excitations in a many spin system are in fact due to the collective changes in spin-orbit coupling energy and this energy scale is known as the magnetic anisotropy energy [101]. The ability to accurately predict and modify the MAE is a key to understanding QTM and the temperature range at which a system will retain its magnetic orientation.

As pointed out early by van Vleck, [101] the magnetic anisotropy Hamiltonian, which ultimately controls the above tunneling resonances, arises because of spin-orbit coupling and other relativistic terms. For over a decade it has been recognized that the calculation of magnetic anisotropies are in principle possible within density-functional theory [102] and many researchers have performed such calculations on solids and films [103]. Problems associated with the accurate density-functional-based determination of MAE in the solid state have been identified and the role of incomplete orbital polarization has been shown to be one issue related to inaccuracies in the solid.

Calculations on such correlated systems present a challenge to mean-field frameworks such as density-functional theory because it is important to account for the strong ligand-metal interactions and to determine whether the behavior of a given spin system is mainly mediated by the anisotropy, by spin-spin coupling or by a combination of the two.

After some theoretical details on the calculation of the spin-orbit coupling and magnetic anisotropy energy the author will discuss several magnetic clusters with respect to their electronic structure, magnetic anisotropy and the V_{15} spin system, which is governed by spin-spin interactions.

2.5.1 Spin-orbit coupling and magnetic anisotropy energy

Recently, Pederson and Khanna have developed a method for accounting for second-order anisotropy energies [104, 105]. This method relies on a simple albeit exact method for spin-orbit coupling and a second-order perturbative treatment of the spin Hamiltonian to determine the dependence of the total energy on spin projection. In this method, a cartesian representation of the spin-orbit term is used which is exact and also is more adaptable for multi-center systems. According to this method, the spin-orbit coupling term

$$U(\mathbf{r}, \mathbf{p}, \mathbf{S}) = -\frac{1}{2c^2}\mathbf{S} \cdot \mathbf{p} \times \nabla\mathbf{\Phi}(\mathbf{r}) \tag{2.7}$$

can be incorporated as given below. Using single-particle wavefunctions expressed in terms of a basis set

$$\psi_{is}(\mathbf{r}) = \sum_{j,\sigma} C^{is}_{j\sigma}\phi_j(\mathbf{r})\chi_\sigma, \tag{2.8}$$

where the $\phi_j(\mathbf{r})$ are the spatial functions and χ are spin functions, the matrix elements can be expressed as

$$\begin{aligned} U_{j,\sigma,k,\sigma'} &= \langle \phi_j\chi_\sigma \mid U(\mathbf{r}, \mathbf{p}, \mathbf{S}) \mid \phi_k\chi_{\sigma'}\rangle & (2.9)\\ &= -i\langle \phi_j \mid V_x \mid \phi_k\rangle\langle \chi_\sigma \mid S_x \mid \chi_{\sigma'}\rangle & (2.10)\end{aligned}$$

where the operator V_x is defined as

$$\langle \phi_j \mid V_x \mid \phi_k\rangle = \frac{1}{2c^2}\left(\left\langle \frac{d\phi_j}{dz}\middle|\Phi\middle|\frac{d\phi_k}{dy}\right\rangle - \left\langle \frac{d\phi_j}{dy}\middle|\Phi\middle|\frac{d\phi_k}{dz}\right\rangle\right). \tag{2.11}$$

In the above, $\Phi(\mathbf{r})$ is the Coulomb potential. Thus this treatment uses matrix elements of the Coulomb potential with partial derivatives of the basis functions, thereby avoiding the time consuming task of calculating the gradient of the Coulomb potential directly.

Δ_{SO}	Ar		Kr	
	NRLMOL	Dirac	NRLMOL	Dirac
2p	0.0796	0.0817	1.8731	1.9635
3p	0.0063	0.0066	0.2775	0.2897
3d	—	—	0.0471	0.0479

Table 2.3: Spin-orbit splittings of energy levels (Δ_{SO} in Hartree) for Ar and Kr calculated with NRLMOL compared to results of a full relativistic numerical solution of the Dirac equation [106].

The implementation of the spin-orbit coupling has been tested on calculations of the energy level splittings of several free noble atoms because in that case one can compare with non spin polarized solutions of the Dirac equation [106]. Some results are shown in Table 2.3. Please note that the agreement improves significantly for the outer electronic shells, for which in general relativistic effects become less important. This is very important because a completely filled shell gives no contribution to the magnetic anisotropy energy. Only the states close to the Fermi level are important for the determination of the tunneling barriers.

Here we generalize some of the derivations from uniaxial symmetry to an arbitrary one. The same definitions and lettering of the symbols is used as in Ref. [105]. In the absence of a magnetic field, the second-order perturbative change to the total energy of a system with arbitrary symmetry can be expressed as

$$\Delta_2 = \sum_{\sigma\sigma'} \sum_{ij} M_{ij}^{\sigma\sigma'} S_i^{\sigma\sigma'} S_j^{\sigma'\sigma}, \tag{2.12}$$

which is the generalization of Eq. (19) of Ref. [105]. In the above expression, σ sums over the spin degrees of freedom and i, j sums over all the coordinate labels, x, y, z respectively. The matrix elements $S_i^{\sigma\sigma'} = \langle \chi^{\sigma} | S_i | \chi^{\sigma'} \rangle$ implicitly depend on the axis of quantization. The matrix elements $M_{ij}^{\sigma\sigma'}$ are given by

$$M_{ij}^{\sigma\sigma'} = -\sum_{kl} \frac{\langle \phi_{l\sigma} | V_i | \phi_{k\sigma'} \rangle \langle \phi_{k\sigma'} | V_j | \phi_{l\sigma} \rangle}{\varepsilon_{l\sigma} - \varepsilon_{k\sigma'}}, \tag{2.13}$$

where $\phi_{l\sigma}$ are occupied and $\phi_{k\sigma'}$ and unoccupied states and ε's are the energy of the corresponding states.

The above equation can be rewritten in a part diagonal in the spin index plus the non-diagonal remainder according to:

$$\Delta_2 = \sum_{ij} \sum_{\sigma} M_{ij}^{\sigma\sigma} S_i^{\sigma\sigma} S_j^{\sigma\sigma} + \sum_{ij} \sum_{\sigma \neq \sigma'} M_{ij}^{\sigma\sigma'} S_i^{\sigma\sigma'} S_j^{\sigma'\sigma}. \tag{2.14}$$

Using the following relation for the expectation value of a spin operator for a closed shell molecule with ΔN excess majority spin electrons

$$\langle 1|S_i|1\rangle = -\langle 2|S_i|2\rangle = \frac{\langle S_i\rangle}{\Delta N}, \tag{2.15}$$

the first term of Eq. (2.14) can be expressed as

$$\sum_{ij}(M_{ij}^{11} + M_{ij}^{22})\frac{\langle S_i\rangle\langle S_j\rangle}{(\Delta N)^2}. \tag{2.16}$$

With the help of

$$\begin{aligned}\langle 1|S_i|2\rangle\langle 2|S_j|1\rangle &= \langle 1|S_iS_j|1\rangle - \langle 1|S_i|1\rangle\langle 1|S_j|1\rangle \\ &= \langle 1|S_iS_j|1\rangle - \frac{\langle S_i\rangle\langle S_j\rangle}{(\Delta N)^2},\end{aligned} \tag{2.17}$$

and similar relation for $\langle 2|S_i|1\rangle\langle 1|S_j|2\rangle$, and a bit of algebra the second term of Eq. (2.14) becomes

$$\sum_{ij} -(M_{ij}^{12} + M_{ij}^{21})\frac{\langle S_i\rangle\langle S_j\rangle}{(\Delta N)^2} + \frac{1}{4}\sum_i M_{ii}^{12} + M_{ii}^{21}\ . \tag{2.18}$$

Therefore, the total second order shift Δ_2 together from Eq.(2.16) and Eq.(2.18) becomes

$$\begin{aligned}\Delta_2 &= \frac{1}{4}\sum_i M_{ii}^{12} + M_{ii}^{21} + \\ &\quad \sum_{ij}(M_{ij}^{11} + M_{ij}^{22} - M_{ij}^{12} - M_{ij}^{21})\frac{\langle S_i\rangle\langle S_j\rangle}{(\Delta N)^2}.\end{aligned} \tag{2.19}$$

As can be easily verified, the last equation gives the same result for uniaxial symmetry as Eq. (21) of Ref. [105], where the Cartesian off-diagonal M_{ij} matrices vanish and $M_{xx}^{\sigma\sigma'} = M_{yy}^{\sigma\sigma'}$. For the derivation of the above expression of Δ_2 we did not assume any particular symmetry, therefore the resulting expression is general.

A few relevant points about this method are that for electronic structure calculations which employ an analytical basis set such as Gaussians, it is easier to take the derivative of the basis functions rather than that of the Coulomb potential. The treatment uses the Cartesian formulation as given above which is exact and therfore accounts for all contributions from the nuclear and electronic potential which is a major part of the spin-other orbit effects. Further, although the spin-orbit coupling is not incorporated into the self-consistent cycle, the results are still quite accurate due to the fact that the first order perturbation

to density due to the operator $-i\mathbf{V}\cdot\mathbf{S}$ vanishes. This follows from the fact that the first order corrections to orbitals are purely imaginary.

Our calculations include all single-determinental two-electron interactions which have a classical origin due to the interaction of a moving spin 1/2 electron in a field of charge protons and electrons. It does not include any effects which are related to multi-determinental overlap. These effects may be small in the case that the metal-ion overlap is small as is the case for most single molecule magnets.

For gapless systems, direct diagonalization of the Hamiltonian including the spin-orbit operator can be used instead of second-order perturbation theory. The anisotropy hamiltonian is then determined by accounting for changes in the trace as a function of the axis of quantization or magnetization direction. Because of the small gaps in this problem we have used both exact diagonalization and second-order perturbation theory for the results presented here. However we find that the results do not strongly depend on the numerical treatment even though the gaps near the Fermi level are small. Typical differences between the perturbative and exact diagonalization treatment are approximately 2-4 percent. We believe the reason for the accuracy of the perturbative treatment is that the numerator in a second-order expansion vanishes as the square of the spatial overlap between states so that nearly degenerate pairs of occupied and unoccupied states which are spatially disparate will not contribute to the MAE.

2.5.2 Electronic structure of the Fe_8 magnet

Appendix J discusses the electronic structure of one of the most widely investigated single molecule magnet. The octanuclear iron(III) Fe_8-cluster has the chemical formula $[Fe_8O_2(OH)_{12}(tacn)_6]^{8+}$, with tacn = 1,4,7-trizacyclononane ($C_6N_3H_{15}$).

The structure of the Fe_8-cluster is shown in Figure 2.11. The approximate D_2 symmetry observed in the molecule [95], is formally broken by the presence of halide atoms and water of crystallization.

The central iron atoms are connected by oxo-hydroxo bridges to the four outer iron ions. The large spheres show the iron atoms, which are Fe(III) ions with a d^5 electron configuration. The ferrimagnetic coupling of spins between the eight Fe atoms results in an $S = 10$ spin ground state [107] and is illustrated by arrows inside the spheres. The organic tacn-rings are very important for stabilizing the magnetic core of the molecule because the three pairs of nitrogen dangling bonds complete a quasi six-fold environment for the Fe atoms. Further, the tacn-rings separate the Fe_8-clusters in the crystal, resulting in negligible intermolecular dipole fields which are typically of the order of 0.05T [99]. The resulting formal charge states are nominally Fe^{3+}, $(OH)^{-1}$ O^{-2}, and $tacn^0$ leading to a molecule with an overall formal charge state of +8 which may then

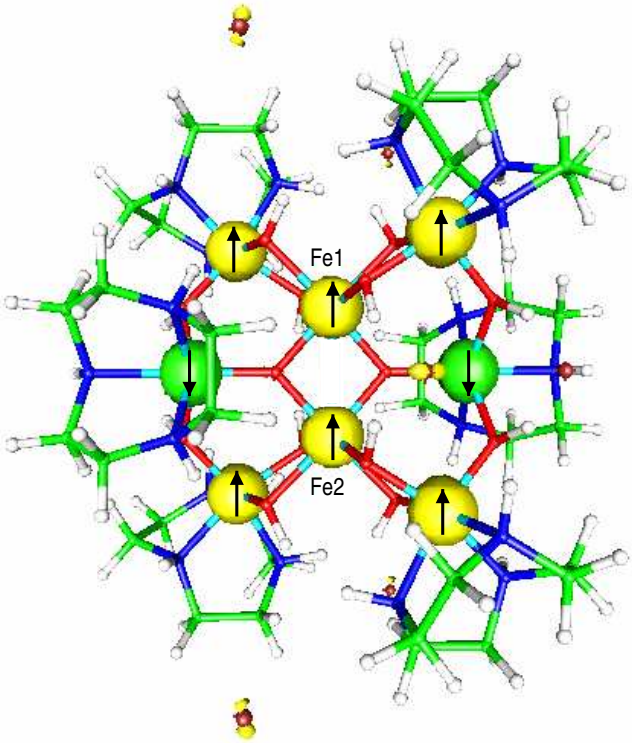

Figure 2.11: The geometry of the Fe_8 cluster. The large balls show isosurfaces of the spin density at $\pm 0.08 e/a.u.^3$. the arrows represent the ferrimagnetic spin ordering in the cluster. On top and bottom a fluorine atom can be seen, which also has small spin polarization.

be compensated by the eight negatively charged halide ions.

In the molecular crystal the positive (+8) charged Fe_8-cluster is neutralized by eight Br ions. However in our Br calculations we found that the Fe to Br charge transfer was incomplete. The incomplete charge transfer lead to a competition between ferrimagnetic and ferromagnetic ordering with the ferromagnetic state lying lower. The incomplete charge transfer was confirmed by a density of states plot, similar to Fig. 2.12, which showed Br valence p states at the Fermi level. This physically incorrect hybridization of the Br p and Fe d states may be due to several effects. First, at least one of the Br atoms in the crystal is surrounded by waters of crystallization which polarize when placed in close proximity to a Br ion. We find that the HOMO level of a $(Br\text{-}H_2O)^{-1}$ anionic complex, while still predominantly Br(4p), is decreased by 0.70 eV as compared to an isolated Br^{-1} anion. Further the induced (electrical) dipole moment on the H_2O molecules decreases the Br valence p states by approximately 0.70 eV and decreases the Hubbard U from approximately 4.12 to 3.59 eV according to our DFT calculations. This is a large effect. For example, within

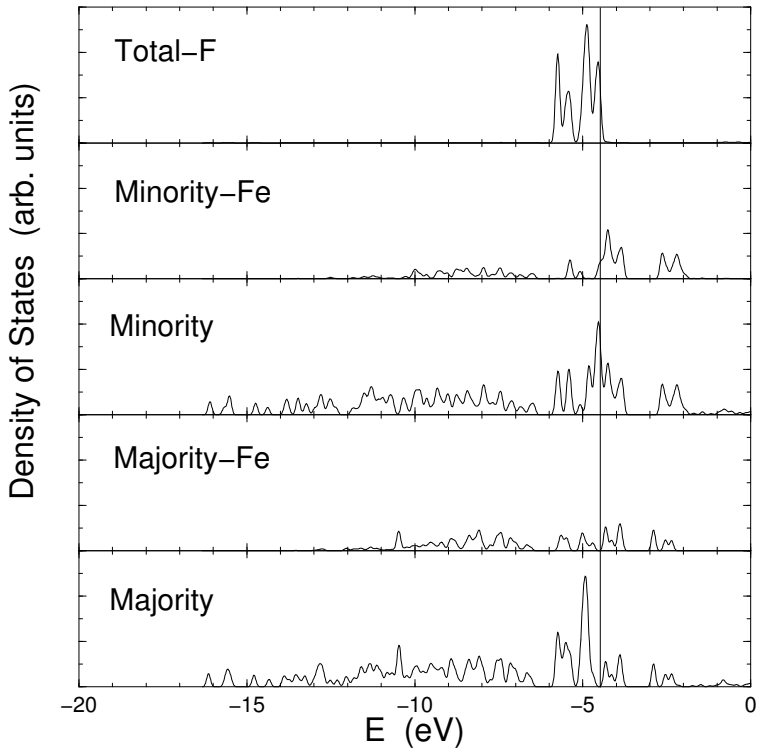

Figure 2.12: The total and projected density of states for the fluorinated Fe_8 complex near the Fermi level as calculated within GGA. The F $2p$ states appear at the Fermi level.

GGA, an isolated Br-H_2O complex prefers full charge transfer compared to an isolated Br ion. Another possible source for incomplete charge transfer could be the need for either self-interaction corrections or LDA+U methods. Inclusion of such corrections could enhance the charge transfer from the Fe to Br atoms. Finally, the Madelung contributions which are complete in the crystal would act to increase the ionicity of each of the components of the molecular complex. While we were unable to stabilize a ferrimagnetic $S = 10$ state for the isolated brominated molecular complex, we found that the application of any small spin-independent external potential which favored the Br atoms over the Fe atoms would allow for the experimentally observed magnetic state.

The considerations from the above paragraph lead us to the view that a fluorinated version of the molecule would provide a better starting point for calculations on this system. Flourine is more electro-negative and therefore allows for a more complete charge transfer. With the F atoms the calculations converged to the experimentally observed ferrimagnetic state with $S = 10$ without an external potential. However, the metallic behavior at the Fermi level with a strong peak due to the fluorine p states near the Fermi level remained.

Molecule	S	D(K)		E(K)		type	References	
		Theory	Expt.	Theory	Expt.		Theory	Expt.
Mn_{12}	10	-0.56	-0.56	0	0	uniaxial	[108]	[109]
Mn_{10}	13	-0.06	-0.05	0	0	uniaxial	[110]	[111]
Fe_4	5	-0.56	-0.57	0.06	0.05	triaxial		[112]
Cr_1	3/2	-2.49	-2.66	0	0	uniaxial		[113]

Table 2.4: Comparison of the calculated and experimental magnetic anisotropy parameters for the single molecule magnets discussed in the text.

This is shown in Fig. 2.12. We have used a Fermi-function with an electronic temperature of 0.001 a.u. for the occupation of states near the Fermi level.

2.5.3 Magnetic anisotropy in single molecule magnets

Up to second order, the spin Hamiltonian can in general be expressed as

$$H = \sum_{i,j} \gamma_{ij} S_i S_j, \tag{2.20}$$

where i, j sum over x, y, z. Diagonalizing this particular anisotropy Hamiltonian defines the set of principal axes and in the most general case identifies the easy, medium and hard axes. Using the eigenvalues one can rewrite (2.20) in the more often used standard form which differs from (2.20) by an insignificant additional constant

$$H = DS_z^2 + E(S_x^2 - S_y^2), \tag{2.21}$$

where D and E are known as axial and transverse anisotropy parameters.

In Table 2.4 we present the calculated D and E parameters for a few single molecule magnets and compare with the available experimental values. We refer to these molecules in the text by their transition metal core since it is these atoms which are responsible for their magnetic behavior. In all the cases presented here the spin ordering is in agreement with experiment. In all cases except Fe_4, the geometries were optimized till the forces on the atoms became negligible. The geometry optimizations were carried out at the all-electron level and to reduce computational costs, the symmetry of the molecule was exploited whenever possible.

The calculated D and E parameters for Mn_{12}, Mn_{10}, the ferric star Fe_4 and Cr-amide molecular magnets are in excellent agreement with experimental values. The single molecule magnets are in general characterized by a high spin ground-state. However, as can be seen from Table 2.4, a high spin state does not necessarily correlate with a high anisotropy barrier.

Some detailed discussion of these results will be given below.

Mn_{12}-acetate

The Mn_{12} molecule has S_4 symmetry and therefore the calculations were carried out using only 25 inequivalent atoms. Moreover, in Mn_{12}, the acetate units were replaced by formate groups (OOCH) so as to reduce the computational efforts while keeping the core of the molecule the same. This molecule has ferrimagnetic spin ordering with an inner core of Mn_4O_4 of minority spin atoms and an outer ring of Mn_8O_8 majority spin atoms. The inner-core Mn atoms have spin magnetic moment of $-3\mu_B$ whereas the outer ones have 4 μ_B thus leading to a net magnetic moment of 20 μ_B.

The HOMO and the LUMO belong to the majority spin channel and the gap is quite small 0.45 eV [105]. The density of states near the Fermi level are dominated by the Mn 3d states and has also some contribution from oxygen 2p states. Although the states near the Fermi level belong to the majority spin channel, it is actually the majority occupied and minority unoccupied states which contribute nearly 65% of the anisotropy barrier. For more information see [104, 105, 108, 114, 115].

Mn_{10} cluster

The $[Mn_{10}O_4$(2,2'-biphenoxide)$_4Br_{12}]^{4-}$ functional unit is compensated by cluster with a single Mn center $[Mn(CH_3CN)_4(H_2O)_2]$. Experimental results suggest that the magnetic anisotropy is due to the localized valence electrons of the ten Mn atoms and our calculations on the $[(CH_3CH_2)_3NH]_2[Mn(CH_3CN)_4(H_2O)_2]$ confirm that this unit behaves as a charge compensating paramagnetic spectator. High-field EPR measurements have determined that the molecule in its ground state has spin $S = 12$. However, our calculations have shown that this spin state would not be magnetically stable since there would be no common Fermi level in the majority and minority channels. As a result we obtained a $S = 13$ spin state. This is consistent with experiment since it is difficult to differentiate between the two possibilities experimentally [116].

The majority gap is also in the case of Mn_{10} much smaller than the minority one [110]. In Mn_{10}, all matrix elements from the occupied majority electrons prefer an easy-axis system whereas the matrix elements from the occupied minority spin channel would result in an easy-plane system. There is a competition between these possibilities and due to the larger contribution from the occupied majority spin channel the system ends up as an easy-axis system. Therefore, in spite of the fact that Mn_{10} possesses a high-spin state, the anisotropy barrier in this system is small. The calculated barrier height of 9.5K compares reasonably well with the experimental value of 7.7K [111]. We found that the removal of subsets of the Br ions will change the magnetic anisotropy drastically by changing the electronic structure. However, neutralizing the electric field due to Br ions by an external potential in the calculations changed the

anisotropy barrier by less than 1 K. Therefore, we conclude that the electric fields created by the Br ions do not have a significant effect on the magnetic properties of the molecule in contrast to chemical interactions. A detailed discussion of that system is given in Appendix K.

Fe_4-star

While the molecular structure of the other examples is well known or has been discussed in detail in an earlier publication it seems to be worthwhile to give the structure for this case to demonstrate the magnetic ordering. In the Ferric star or the Fe_4 cluster shown in Fig. 2.13, all iron atoms are Fe^{3+}-ions, the inner Fe is coupled antiferromagnetically to the outer Fe atoms, resulting in a ferrimagnetic spin-ordering with total $S = 5$. The calculated values in Table 2.4 for the Fe_4 show very good agreement with experimental data. This calculation has been a real test of the accuracy of the theoretical approach because it was carried out in form of a blind test. The magnetic parameters have been determined experimentally at the University Erlangen [112]. The DFT calculation has been carried out without that information and in that respect can be regarded as a true theoretical prediction.

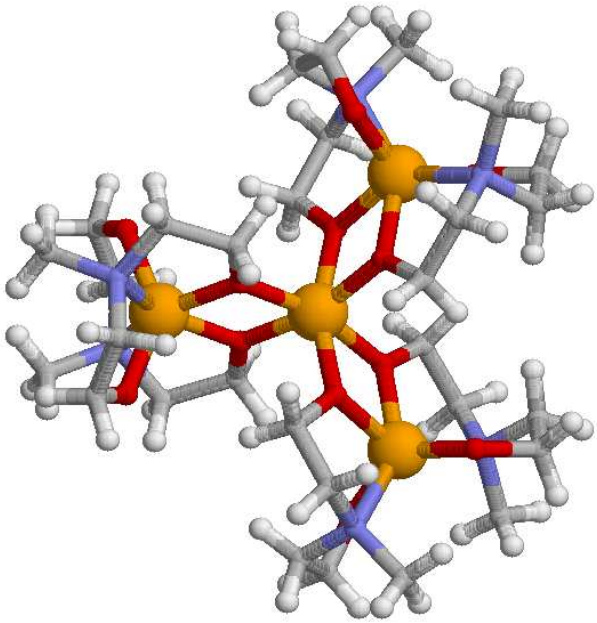

Figure 2.13: The molecular structure of the Fe_4-star. The four Fe atoms are shown by large spheres.

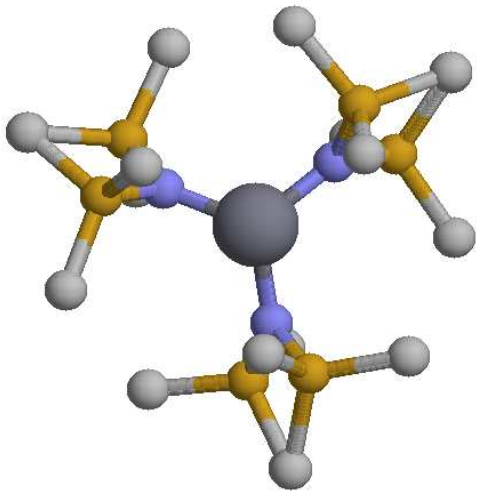

Figure 2.14: The molecular structure of the Cr-amide. The Cr atom in the center is shown by the large sphere. Hydrogens are not displayed for clarity.

Cr-amide

The Cr-amide $Cr[N(Si(CH_3)_3)_2]_3$ contains only a single magnetic center (Cr^{3+}) located in the middle of the molecule threefold coordinated by nitrogen atoms (see Fig. 2.14). The charge state is confirmed by calculating the spin density within a sphere around the Cr atom. A sphere with radius of 1.2 Å contains already 2.7 majority electron, clearly confirming the Cr^{3+} charge state. The electronic density of states obtained from Gaussian broadened molecular levels is presented in Fig. 2.15. The HOMO comes from Cr majority 3d states at around -5 eV. The Cr-molecule has large majority and minority gaps on the order of 2 eV and 2.5 eV respectively. The anisotropy barrier in this molecule is small (Table 2.4) which can be attributed to the large HOMO-LUMO gap. In this case the spin density is well localized on the Cr atom. The HOMO and LUMO states are definitely Cr(3d) and there is some covalent bonding between the Cr states and the ligands. The magnetic behavior is completely determined by the Cr states. This is an interesting case. Since the spin is small (3/2) there is only one magnetic field at which resonant tunneling of magnetization would be achieved. However, no such experimental measurements have been reported so far. The calculated magnetic anisotropy barrier of 5.6 K agrees well with the experimental value of 6 K obtained from electron spin resonance measurements [113].

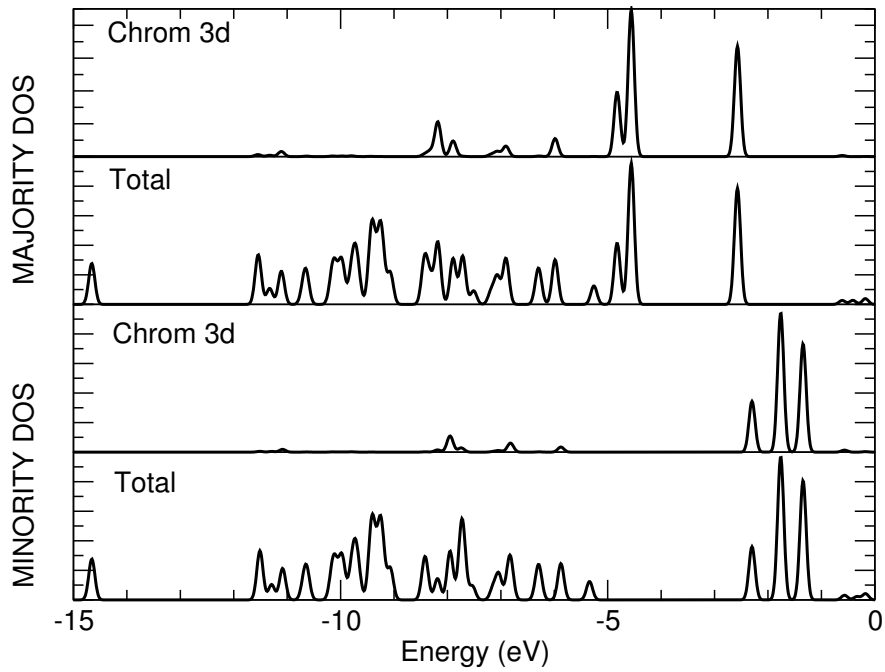

Figure 2.15: The electronic density of states of the Cr-amide. The HOMO is derived from Cr majority 3d spin states at -5 eV. The molecular levels have been broadened by a Gaussian.

2.5.4 The V_{15} spin system

The $K_6[V_{15}As_6O_{42}(H_2O)]\ 8H_2O$ molecular crystal, first synthesized by Müller and Döring [100], represents a transition-metal spin system in the same size regime as the Mn_{12} and Fe_8 molecular crystals. In contrast to Mn_{12} and Fe_8 molecules, the V_{15} molecule is thought to behave as a weakly anisotropic magnet composed of 15 spin s=1/2 particles which couple together to form a molecule with a total spin S=1/2 ground state. Calculations on such correlated systems present a challenge to mean-field frameworks such as density-functional theory because it is often not possible to construct a single collinear reference state which preserves the inherent symmetry of the system and has the correct spin quantum numbers. Appendix J presents some results on the electronic structure calculations of this system.

The work in Appendix L utilizes an efficient coupled multilevel analysis which relies on fitting density-functional energies to mean-field Heisenberg or Ising energies in order to determine the exchange parameters. The approximate exchange parameters gleaned from the first N Ising configurations were used to find the next lowest energy Ising configuration and subsequently to improve the parameterization of the exchange parameters. "Self Consistency" of this approach is determined when the predicted Ising levels are unchanged

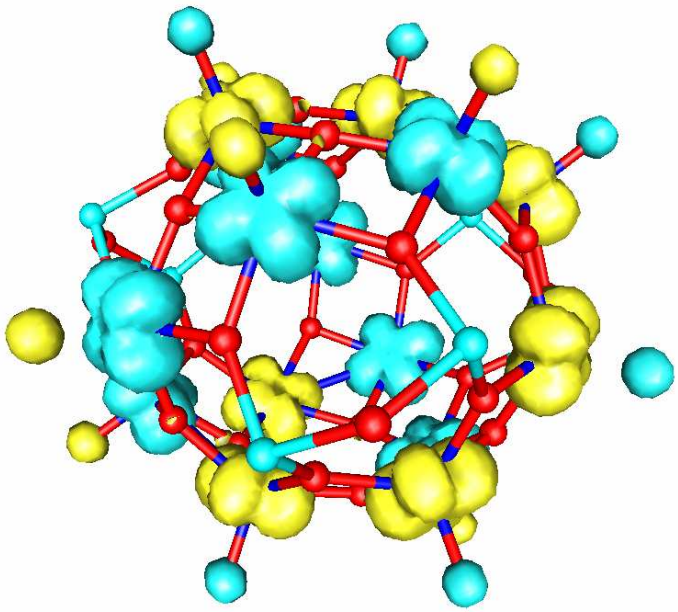

Figure 2.16: The spin density of the V_{15} cluster. The picture shows clearly the single d-electron of a V^{4+} ion. Most of the spin density is localized at the V, less than 1% of the spin density is on the oxygen atoms which are on top of the V. The dark balls represent oxygen and the lighter ones arsenic.

by the addition of data from new Ising configurations. The coupling of the density-functional method to a classical Ising representation allowed us to determine the exchange parameters by considering only several spin configurations. Further, the resulting ground-state spin configuration within density-functional theory exhibits the correct spin projection of $1/2$. With the exchange parameters determined, we diagonalize the complete many-body Heisenberg Hamiltonian to calculate the susceptibility and spin correlation functions for comparison with experiment. The many-body basis is complete, so all states are allowed including non-collinear spin arrangements and quantum disordered phases.

All of the data displayed in Table 2.5 has been used to determine the exchange parameters from a least square fit to the mean-field solution of the Heisenberg Hamiltonian

$$H = \sum J_{ij} \mathbf{S}_i \cdot \mathbf{S}_j. \tag{2.22}$$

E	Fit	J	J'	J''	$J1$	$J2$	$J3$	Spin	Label	δ (K)
-78.37	-78.44	-6	2	-2	6	-6	-1	1/2	I	0.8
-73.39	-73.63	-6	2	-2	4	-4	-1	1/2	II	
-35.48	-35.08	-6	-2	2	4	-4	-1	1/2	III	
-34.89	-34.53	-6	-2	2	4	-4	3	3/2	IV	
0.00	-0.79	-6	-6	6	6	-6	3	3/2	V	1.5
8.38	8.28	-6	-6	6	2	-2	-1	1/2	VI	1.3
28.14	28.08	-6	-6	6	-6	6	3	3/2	VII	
126.32	126.14	-4	-4	6	4	-6	3	1/2	VIII	
129.17	128.88	-4	-4	2	6	-4	3	5/2	IX	
278.35	278.50	-2	-6	2	4	-4	3	3/2	X	
434.22	435.78	0	0	6	6	0	3	9/2	XI	1.6
760.75	760.76	6	6	6	-6	-6	3	9/2	XII	1.6
873.11	872.35	6	6	6	6	6	3	15/2	XIII	1.8

Table 2.5: DFT energies (E in meV) of calculated Ising configurations, energies obtained from the fit, and $4\langle S_i^q S_j^q \rangle$ along each of the six bonds. Also included is the anisotropy shift δ for the $M_s = S$ state of each Ising configuration. A least square fit of this data leads to exchange parameters of J=290.3, J'=-22.7, J"=15.9, $J1$=13.8, $J2$=23.4 and $J3$=0.55 meV.

The fit is very good with errors ranging from 0.1-1.55 meV. The fit leads to exchange parameters of J = 290.3 meV, J'= -22.7 meV, J''=15.9 meV, $J1$ = 13.8 meV, $J2$ = 23.4 meV and $J3$ = 0.55 meV, where positive numbers correspond to AF and negative ones to FM interactions. The *ferromagnetic* interaction J' is a surprising result and deserves further discussion since it is qualitatively different from earlier assumptions based on entirely AF interactions [100,117]. Ferromagnetic coupling is possible without polarizing the oxygens through a 4'th order process similar to super-exchange. In super-exchange, the intermediate state has the lowest d-orbital on the V doubly occupied with up and down electrons [118]. However, electrons can also hop to higher energy d-orbitals on the V's. In this case both parallel and antiparallel spins are allowed without violating the Pauli exclusion principle, but Hund's rule coupling prefers parallel alignment. The super-exchange process (same d-orbital) completely excludes the process with same-spin electrons while the FM process (different d-orbitals) merely favors FM alignment. Thus a FM coupling is obtained if the V-O hopping matrix elements into the higher d-orbital are significantly larger than the matrix elements for the hopping of O electrons into the lowest energy d-orbital. The occurrence of such interactions are possible in a low-symmetry system such as the one studied here.

Even with this FM interaction, our spin Hamiltonian yields an S=1/2 ground

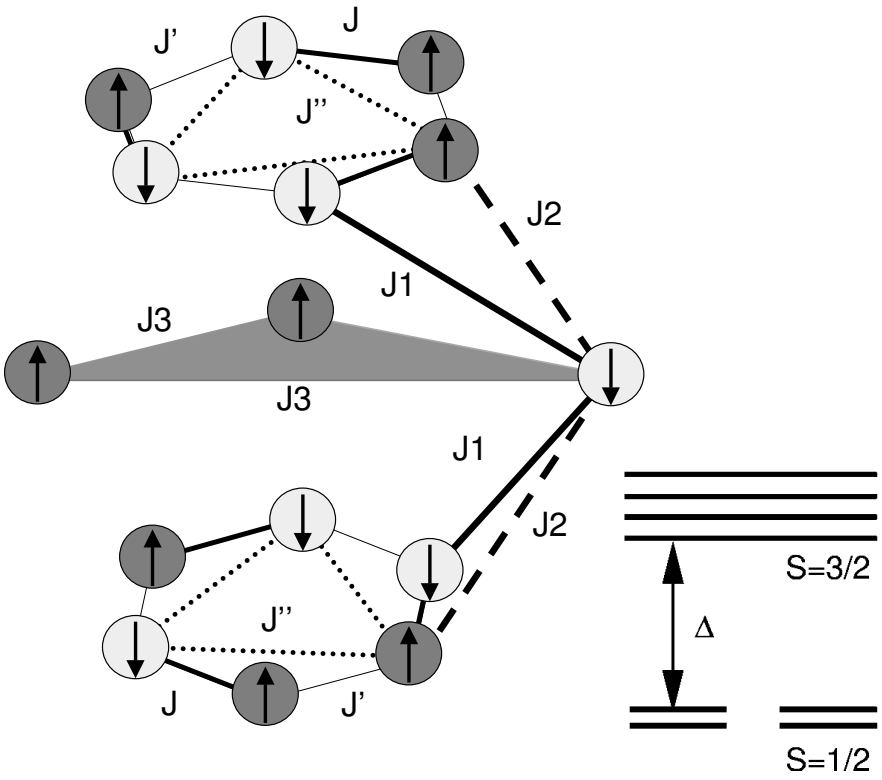

Figure 2.17: The 15 magnetic vanadium atoms of the $K_6[V_{15}As_6O_{42}(H_2O)]$ molecule. They form two hexagonal layers and an inner triangular layer of vanadium atoms sandwiched within. The arrows show the lowest energy spin configuration found from DFT calculations. The six exchange parameters used in the Heisenberg Hamiltonian are shown as lines. Schematically displayed are energy levels of the Kramer doublet (S=1/2) ground state and the low lying quadruplet (S=3/2) separated by Δ.

state composed largely of Ising configurations similar to the one depicted in Fig. 2.17. This Ising configuration was predicted from the J's from earlier fits to DFT energies and corresponds to the ground state DFT configuration (I).

Comparing our calculated susceptibility with experiment [117], we find the low-temperature behavior indicates our doublet-quadruplet gap $\Delta \approx 10$K to be significantly larger than the experimental value of $\Delta \approx 3.7$K, while the high-temperature behavior shows our calculated value of J is too large. Both of these discrepancies can be explained almost entirely by a J that is too large within the density-functional-based treatment. We note that only the V-V bond length corresponding to J obtained from our DFT optimized geometry (GGA) is too short compared with experiment [119]. The large value of J can be attributed to both exchange processes through the oxygens and to direct exchange between the V. If direct exchange is important, the value of J will be

influenced greatly by the overlap between the V atoms. Similarly, the high temperature behavior will be greatly influenced by changes in geometry, effectively making J temperature dependent. At higher temperatures more high spin configurations get populated, which will have a different geometry than the low temperature $S = 3/2$ configuration used for geometry optimization. Geometry relaxation will influence the ferromagnetic configuration (XII) most, which is also responsible for the large J, making J significantly smaller. Similarly, self-interaction-corrections (SIC) will decrease J because it will localize the vanadium d-orbitals more, decreasing the overlap of the wavefunctions.

In order to determine if our enhanced J may be due to spurious on-site repulsions associated with the DFT, we have approximately accounted for the effects of self-interaction-corrections (SIC) in model calculations on V dimers (V_2 and V_2O_{10}) with electronic structure constrained to match that of the dimers in the V_{15} cluster. The results, while preliminary, show that SIC induced changes in the wavefunctions could decrease the direct contributions to J by a factor of 3 which supports the reduction of J to yield better agreement between experiment and theory.

Chapter 3

Summary

This work presented selected publications of the author in the field of electronic structure calculations. The author carried out all density functional theory calculation for the systems discussed in the Appendices by himself and is responsible for a major part of the theoretical interpretations.

After a short introduction to DFT the author discussed the NRLMOL program package which has been used in most of the cases discussed later in the work. The author contributed actively to the development of NRLMOL by implementing several new features as calculations of hyperfine fields, electric field gradients, simple thermodynamic properties, local charges and spin densities and arbitrary external potentials. Further, he was involved to a great extent in the parallelization of the code and testing and implementation of the spin-orbit capability. The last two achievements have been the basic prerequisite for investigations of single molecule magnets.

The discussion in Section 2.1 focuses on the electronic structure as a measureable quantity itself. There are now several experimental techniques available to probe the electronic structure directly. Basically all these standard methods have been used for the superconductor MgB_2. While any single method always leaves some doubts, the overall excellent agreement of the from DFT theoretically predicted electronic structure with all the experimental methods gives us great confidence in the calculations. This is very important, because most of the theories trying to explain the superconductivity or optical and transport properties rely on this electronic structure.

Electric field gradients do not probe the band structure directly but rather the quality of the obtained charge density. Obviously, these two quantities are closely connected as evident by the Kohn-Sham equation. Modern DFT implementations give very accurate values of the EFG, so that theoretical calculations are often an integral part for the interpretation of experimental data. Similarly, vibrational properties offer a deep insight in materials as shown in Section 2.3. The calculation of vibrational frequencies and IR and Raman intensities from DFT is well established by now. Therefore first-principles calculations become

also here a very important tool in understanding experiments. The examples have been selected to show how this kind of calculation can be used for explaining experimental results, but also that there is enough confidence in the method to make predictions. Certainly, the author hopes that chemists will be able to synthesize azidopentazole and can confirm the predicted properties.

Magnetic materials play a very important role in many areas of technology. In Section 2.4 and 2.5 the author presents results of his work in that field. Most of the work is directed towards the calculation and understanding of the magnetic anisotropy energy. The ability to quantitatively determine which electrons are important for forming the anisotropy energy allows to investigate how chemical and physical modification of assembled arrays of molecular magnets will effect thermal reorientation barriers and spin-tunneling fields. The understanding of the magnetic properties from fundamental research does not only provide information to chemists in order to design novel materials, but can also help to suggest new solutions in other technologically interesting areas. The study of the quantum effects and the dynamics of the magnetization might also help to understand the transition from pure magnetic quantum systems to macroscopic magnetism.

New and interesting physics nearly always arises if different phenomena appear at the same time. The coupling of the vibrational degrees of freedom, the phonons, to the electronic degrees of freedom, the electrons, gives rise to superconductivity, which can be also understood from DFT. Superconductivity in MgB_2, driven by the electron-phonon coupling, has been a major research area of the author [44, 45, 69–76], only publications directly concerned with electronic structure properties have been discussed here. The magnetic ordering is sensitive to the vibrations. The coupling of vibrational degrees of freedom to the magnetic ones giving rise to fourth-order magnetic anisotropy has also been part of the authors research [120].

What have all these examples in common? The used methods cover finite systems, molecules and clusters, as well as infinite systems, solids with periodic crystal structure. The author wanted to show that the DFT can be applied successfully in very different areas. The good agreement of first-principles calculations with experimental results without using any experimental data as input allows for real predictions. Predictions of new materials with customized properties made on a computer. The progress in this field gives us enough confidence to use the term *computer experiments* as a fertile option for the future. Besides the classical division of physics in experimental and theoretical physics, physics on the computer may be a third column on which physics rests.

Bibliography

[1] C. Kittel *Introduction to Solid State Physics*, John Wiley and Sons, (New York, 1963).

[2] P. Hohenberg and W. Kohn, Phys. Rev. **136**, B864 (1964).

[3] W. Kohn and L. J. Sham, Phys. Rev. **140**, A1133 (1965).

[4] R. O. Jones and O. Gunnarsson, Rev. Mod. Phys. **61**, 689 (1989).

[5] O. K. Andersen, *Band structure of transition metals*, Mont Tremblant international summer school 1973; O. K. Andersen *Electronic structure of metals* Lecture Notes 1977/78; (The yellow LMTO bibels).

[6] Lecture Notes in Physics, Ed. D. Joubert, *Density functionals*, Springer (Heidelberg) 1998.

[7] R. M. Dreizler and E. K. U. Gross, *Density functional Theory*, Springer (Berlin) 1990.

[8] H. Eschrig, *The Fundamentals of Density Functional Theory*, Teubner (Stuttgart, Leipzig) 1996.

[9] O. Gunnarsson and B. I. Lundqvist, Phys. Rev. B **13**, 4274 (1976).

[10] D. M. Ceperley and B. J. Alder, Phys. Rev. Lett. **45**, 566 (1980).

[11] W. M. C. Foulkes, L. Mitas, R. J. Needs and G. Rajagopal, Rev. Mod. Phys. **73**, 33 (2001)

[12] U. von Barth and L. Hedin, J. Phys. C **5**, 2064 (1972).

[13] S. H. Vosko, L. Wilk, and M. Nusair, Can. J. Phys. **58**, 1200 (1980).

[14] J. P. Perdew and A. Zunger, Phys. Rev. B **23**, 5048 (1981).

[15] J. P. Perdew, K. Burke and M. Ernzerhof, Phys. Rev. Lett. **77**, 3865 (1996).

[16] J. P. Perdew, J. A. Chevary, S. H. Vosko, K. A. Jackson, M. R. Pederson, D. Singh and C. Fiolhais, Phys. Rev. B **45**, 6671 (1992).

[17] A. Becke, Phys. Rev. A **38**, 3098 (1988);A. D. Becke, J. Chem. Phys. 98 (1993) 13

[18] C. Lee, W. Yang, and R. G. Parr, Phys. Rev. B 37, 785-789 (1988).

[19] B.Delley, J.Chem.Phys.**92** 508 (1990); ibid. **94** 7245 (1991); ibid **113** 7756 (2000): B. Delley, J. Phys. Chem. **100** 6107 (1996).

[20] E. Wimmer, H. Krakauer, M. Weinert and J. Freeman, Phys. Rev. B **24**, 864 (1981).

[21] O. K. Andersen, Phys. Rev. B **12**, 3060 (1975).

[22] J. A. Pople *et al*, GAUSSIAN94 (Gaussian, Inc., Pittsburgh PA, 1994).

[23] E. E. Lafon and C. C. Lin, Phys. Rev. **152**, 579 (1966).

[24] G. S. Paynter and F. W. Averill, Phys. Rev. B **26**, 1781 (1982).

[25] B. I. Dunlap, J. W. Connolly, and J. R. Sabin, J. Chem. Phys. **71**, 3396 (1979).

[26] J. Andzelm, E. Radzio and D. R. Salahub, J. Comput. Chem. **6**, 520 (1985).

[27] R. Jones and A. Sayyash, J. PHys. C **19**, L653 (1986).

[28] W. J. Hehre, L. Radom, P. V. R. Schleyer, and J. A. Pople, *Ab-Initio Molecular Orbital Theory*, John Wiley and Sons Inc, New York (1986).

[29] M. R. Pederson and C. C. Lin, Phys. Rev. B **35**, 2273 (1987).

[30] M. R. Pederson and K. A. Jackson, Phys. Rev. B **41**, 7453 (1990).

[31] K. A. Jackson and M. R. Pederson, Phys. Rev. B **42**, 3276 (1990).

[32] M. R. Pederson and K. A. Jackson, Phys. Rev. B **43**, 7312 (1991).

[33] A. A. Quong, M. R. Pederson and J. L. Feldman, Sol. Stat. Comm. **87**, 535 (1993).

[34] M. R. Pederson, J. Q. Broughton and B. M. Klein, Phys. Rev. B **38**, 3825 (1988).

[35] D. V. Porezag and M. R. Pederson, Phys. Rev. B **54**, 7830 (1996).

[36] A. Briley, M. R. Pederson, K. A. Jackson, D. C. Patton, and D. V. Porezag, Phys. Rev. B **58**, 1786 (1998).

[37] D. Porezag and M. R. Pederson, Phys. Rev. A **60**, 2480, (1999).

[38] M. R. Pederson, D. V. Porezag, J. Kortus and D. C. Patton, phys. stat. sol. (b) **217**, 197 (2000).

[39] See D.D. Johnson, Phys. Rev. B **38**, 12807 (1988) and references therein.

[40] H. Hellmann, *Einführung in die Quantentheorie*, Deuticke, Leipzig, (1937); R. P. Feynman, Phys. Rev. **56**, 340 (1939); P. Pulay, Mol. Phys. **17**, 197 1969).

[41] J. Nagamatsu, N. Nakagawa, T. Muranaka, Y. Zenitani and J. Akimitsu, Nature (London) **410**, 63 (2001).

[42] M. L. Kulic, Phys. Rep. **338**, 1-264 (2000)

[43] E. G. Maksimov, Uspek. Fiz. Nauk **170**, 1033-1061 (2000).

[44] J. Kortus, I.I. Mazin, K.D. Belashchenko, V.P. Antropov, and L.L. Boyer, Phys. Rev. Lett. **86**, 4656 (2001).

[45] A. Y. Liu, I. I. Mazin and J. Kortus, Phys. Rev. Lett. **87**, 087005 (2001).

[46] Y. Kong, O.V. Dolgov, O. Jepsen, and O.K. Andersen, Phys. Rev. B **64**, 20501 (2001).

[47] E. A. Yelland, J. R. Cooper, A. Carrington, N. E. Hussey, P. J. Meeson, S. Lee, A. Yamamoto, S. Tajima, Phys. Rev. Lett. **88**, 217002 (2002).

[48] H. Uchiyama, K.M. Shen, S. Lee, A. Damascelli, D.H. Lu, D.L. Feng, Z.-X. Shen, and S.Tajima, Phys. Rev. Lett. **88**, 157002 (2002).

[49] J.M. An and W.E. Pickett, Phys. Rev. Lett. **86**, 4366 (2001).

[50] *Electrons at the Fermi surface*, Ed. M. Springford, Cambridge University Press 1980.

[51] H. Rosner, J. M. An, W. E. Pickett, S.-L. Drechsler, Phys. Rev. B **66**, 024521 (2002).

[52] R. Courths, S. Hüfner, Phys. Rep. **112**, 53 (1984).

[53] S. Hüfner, *Photoelectron Spectroscopy*, Springer (Berlin) 1995.

[54] V. D. P. Servedio, S.-L. Drechsler, and T. Mishonov, Phys. Rev. B **66**, 140502 (R) (2002).

[55] A. Alexandrov, cond-mat/0104413

[56] E. Cappellutti, S. Ciuchi, C. Grimaldi, L. Pietronero, and S. Strässler, Phys. Rev. Lett. **88**, 117003 (2002).

[57] P. Blaha, K. Schwarz, and J. Luitz, WIEN97, A FLAPW package for calculating crystal properties (Vienna Austria, ISBN 3-9501031-0-4) 1999; Vienna University of Technology, 1997. Improved and updated version of the original copyrighted WIEN code, which was published by P. Blaha, K. Schwarz, P. Sorantin, and S. B. Trickey, Comput. Phys. Commun. 59, 399 (1990).

[58] U. von Barth and G. Grossmann, Solid State Commun. **32**, 645 (1979); U. von Barth and G. Grossmann, Phys. Rev. B **25**, 5150 (1982).

[59] H. Suhl, B. T. Matthias, and L. R. Walker Phys. Rev. Lett. **3**, 552-554 (1959).

[60] S. V. Shulga, S.-L. Drechsler, H. Eschrig, H. Rosner, and W.E. Pickett, cond-mat/0103154.

[61] F. Giubileo, D. Roditchev, W. Sacks, R. Lamy, D.X. Thanh, J. Klein, S. Miraglia, D. Fruchart, J. Marcus, and Ph. Monod, Phys. Rev. Lett. **87**, 177008 (2001); F. Giubileo, D. Roditchev, W. Sacks, R. Lamy, J. Klein, cond-mat/0105146.

[62] Y. Bugoslavsky, Y. Miyoshi, G.K. Perkins, A.V. Berenov, Z. Lockman, J.L. MacManus-Driscoll, L.F. Cohen, A.D. Caplin, H.Y. Zhai, M.P. Paranthaman, H.M. Christen, and M. Blamire, cond-mat/0110296.

[63] P. Szabó, P. Samuely, J. Kacmarcík, T. Klein, J. Marcus, D. Fruchart, S. Miraglia, C. Marcenat, and A.G.M. Jansen, Phys. Rev. Lett. **87**, 137005 (2001).

[64] S. Tsuda, T. Yokoya, T. Kiss, Y. Takano, K. Togano, H. Kito, H. Ihara, and S. Shin, Phys. Rev. Lett. **87**, 177006 (2001).

[65] X.K. Chen, M.J. Konstantinović, J.C. Irwin, D.D. Lawrie, and J.P. Franck, Phys. Rev. Lett. **87**, 157002 (2001).

[66] Y. Wang, T. Plackowski, and A. Junod, Physica C **355**, 179 (2001); F. Bouquet, R.A. Fisher, N.E. Phillips, D.G. Hinks, and J.D. Jorgensen, Phys. Rev. Lett. **87**, 047001 (2001); H.D. Yang, J.-Y. Lin, H.H. Li, F.H. Hsu, C.J. Liu, S.-C. Li, R.-C. Yu, and C.-Q. Jin , Phys. Rev. Lett. **87**, 167003 (2001).

[67] Ch. Niedermayer, C. Bernhard, T. Holden, R.K. Kremer, K. Ahn, Phys. Rev. B **65**, 094512 (2002).

[68] C. Buzea and T. Yamashita, Supercond. Sci. Technol. **14**, R115(2001).

[69] A. A. Golubov, J. Kortus, O. V. Dolgov, O. Jepsen, Y. Kong, O. K. Andersen, B. J. Gibson, K. Ahn, R. K. Kremer, J. Phys.: Cond. Mat. **14**, 1353 (2002).

[70] E. Z. Kurmaev, I. I. Lyakhovskaya, J. Kortus, A. Moewes, N. Miyata, M. Demeter, M. Neumann, M. Yanagihara, M. Watanabe, T. Muranaka, and J. Akimitsu, Phys. Rev. B **65**, 134509 (2002).

[71] I. I. Mazin and J. Kortus, Phys. Rev. B **65**, 180510 (R) (2002).

[72] A. B. Kuz'menko, F. P. Mena, H. J. A. Molegraaf, D. van der Marel, B. Gorshunov, M. Dressel, I. I. Mazin, J. Kortus, O. V. Dolgov, T. Muranaka, and J. Akimitsu, Solid State Commun. **121,** 479 (2002).

[73] A. Brinkman, A. A. Golubov, H. Rogalla, O. V. Dolgov, J. Kortus, Y. Kong, O. Jepsen, and O. K. Andersen, Phys. Rev. B **65**, 180517 (R) (2002).

[74] A. A. Golubov, A. Brinkman, O. V. Dolgov, J. Kortus, and O. Jepsen, Phys. Rev. B **66**, 054524 (2002)

[75] I. I. Mazin, O. K. Andersen, O. Jepsen, O. V. Dolgov, J. Kortus, A. A. Golubov, A. B. Kuz'menko, and D. van der Marel, Phys. Rev. Lett. **89**, 107002 (2002).

[76] E. G. Maksimov, J. Kortus, O. V. Dolgov, and I. I. Mazin, Phys. Rev. Lett. **89**, 129703 (2002).

[77] K. A. Jackson, S. Srinivas, J. Kortus, and M. R. Pederson, Phys. Rev. B **65**, 214201 (2002)

[78] D. M. Bishop and S. M. Cybulski, J. Chem. Phys. **100**, 6628 (1994).

[79] S. Unterricker and F. Schneider, Hyperfine Interactions **39**, 39 (1988).

[80] B. Kamb, Science **148**, 232 (1965).

[81] P.E. Eaton and T.W. Cole, Jr., J. Am. Chem. Soc. **86** (1964) 3158.

[82] P.C. Hariharan, J.J. Kaufman, A.H. Lowrey, and R.S. Miller, Int. J. Quantum Chem. **28** (1985) 39.

[83] D.A. Chapman, J.J. Kaufman, and R.J. Buenker, Int. J. Quantum Chem. **1** (1991) 389.

[84] M-X. Zhang, P.E. Eaton, and R. Gilardi, Angew. Chem. Int. Ed.**39** (2000) 401.

[85] K.O. Christie, W.W. Wilson, J.A. Sheehy and J.A. Boatz, Angew. Chem. Int. Ed. 38 (1999) 2004.

[86] M.N. Glukhovtsev, H. Jiao, P.v.R. Schleyer, Inorg. Chem. 35 (1996) 7124.

[87] M.T. Nguyen and T.K. Ha, Chem. Ber. 129 (1996) 1157.

[88] G. Chung, M.W. Schmidt, and M.S. Gordon, J. Phys. Chem. 104 (2000) 5647.

[89] L. Gagliardi, S. Evangelisti, A. Bernhardsson, R. Lindh, B.O. Roos, Int. J. Quantum Chem., 77 (2000) 311; L. Gagliardi, S. Evangelisti, P.-O. Widmark, B.O. Roos, Theor. Chem. Acc. 97 (1997) 136.

[90] Q. Wang, Q. Sun, M. Sakurai, J. Z. Yu, B. L. Gu, K. Sumiyama and Y. Kawazoe, Phys. Rev. B **59**, 12672 (1999).

[91] Q. Sun, Q. Wang, K. Parlinski, J. Z. Yu, Y. Hashi, X. G. Gong and Y. Kawazoe, Phys. Rev. B **61**, 5781 (2000); see also Erratum **62**, 16176 (2000).

[92] A.-L. Barra, P. Brunner, D. Gatteschi, Ch. E. Schulz, and R. Sessoli, Europhys. Lett. **35**, 133 (1996).

[93] T. Lis, Acta Crystallogr. Soc. B**36**, 2042 (1980).

[94] R. Sessoli, D. Gatteschi, A. Caneschi, and M. A. Novak, Nature (London) **365**, 141 (1993); A. Caneschi, D. Gatteschi, C. Sangregorio, R. Sessoli, L. Sorace, A. Cornia, M. A. Novak, C. Paulsen and W. Wernsdorfer, J. Magnetism and Magnetic Mat. **200**, 182 (1999).

[95] K. Wieghardt, K. Pohl, I. Jibril and G. Huttner Angew. Chem., Int. Ed. Engl.,**23**, (1984) 77; Cambridge Crystallographic Data Centre; Refcode: COCNAJ; http://www.ccdc.cam.ac.uk/

[96] J. Friedman, M. P. Sarachik, J. Tejeda, J. Maciejewski and R. Ziolo, Phys. Rev. Lett. **76**, 3820 (1996); L. Thomas, F. Lionti, R. Ballou, D. Gatteschi, R. Sessoli and B. Barbara, Nature (London) **383**, 145 (1996).

[97] C. Sangregorio, T. Ohm, C. Paulsen, R. Sessoli and D. Gatteschi, Phys. Rev. Lett. **78**, 4645 (1997).

[98] W. Wernsdorfer and R. Sessoli, Science **284**, 133 (1999).

[99] W. Wernsdorfer, T. Ohm, C. Sangregorio, R. Sessoli, D. Mailly and C. Paulsen, Phys. Rev. Lett. **82**, 3903 (1999).

[100] D. Gatteschi, L. Pardi. A. L. Barra, A. Müller and J. Döring, Nature **354**, 463 (1991).

[101] J. Van Vleck, Phys. Rev. **52**, 1178 (1937).

[102] Z.Q. Gu and W.Y. Ching, Phys. Rev. B **36**, 8545 (1987).

[103] For example see: G. Schneider and H. J. F. Jansen, J. Appl. Phys. **87** 5875 (2000) and references therein, H. J. F. Jansen, Phys. Rev. B **38**, 8022 (1988); A. Shick *et al.* J. Mag. and Mag. Mat. **177** (1216) (1998) and references therein; X.F. Zhong, W.Y. Ching and W. Lai, J. Appl. Phys. 70(10), 6146 (1991).

[104] M. R. Pederson and S. N. Khanna, Phys. Rev. B **59**, 693 (R) (1999).

[105] M. R. Pederson and S. N. Khanna, Phys. Rev. B **60**, 9566 (1999).

[106] http://physics.nist.gov/PhysRefData/DFTdata/contents.html

[107] R. Caciuffo, G. Amoretti, A. Murani, R. Sessoli, A. Caneschi and D. Gatteschi, Phys. Rev. Lett. **81**, 4744 (1998)

[108] M. R. Pederson and S. N. Khanna, Chem. Phys. Lett. **307**, 253, (1999).

[109] K. M. Mertes, Y. Suzuki, M. P. Sarachik, Y. Paltiel, H. Shtrikman, E. Zeldov, E. Rumberger, D. N. Hendrickson, and G. Christou, Phys. Rev. Lett. **87**, 227205 (2001).

[110] J. Kortus, T. Baruah, N. Bernstein, and M. R. Pederson, Phys. Rev. B. **66**, 092403 (2002).

[111] A. L. Barra, A. Caneschi, D. Gatteschi, D. P. Goldberg, and R. Sessoli, J. Solid State Chemistry **145**, 484 (1999).

[112] S. Schromm, O. Waldmann, P. Müller, University Erlangen, private communication.

[113] D. C. Bradley, R. G. Copperthwaite, S. A. Cotton, K. D. Sales, J. F. Gibson, J. Chem. Soc., Dalton Trans. 2 (1973) 191.

[114] M. R. Pederson, J. Kortus and S. N. Khanna, *Cluster and Nanostructure Interfaces*, Eds. P. Jena, S. N. Khanna and B. K. Rao, World Scientific Publishing, Singapore 2000, 159-173, ISBN 981-02-4219-0

[115] M. R. Pederson, D. V. Porezag, J. Kortus and S. N. Khanna, J. Appl. Phys. **87**, 5487 (2000).

[116] R. Sessoli, private communication.

[117] I. Chiorescu, W. Wernsdorfer, A. Müller, H. Bögge and B. Barbara, Phys. Rev. Lett. **84**, 3454 (2000).

[118] J. B. Goodenough, *Magnetism and the Chemical Bond* (Wiley, New York, 1963).

[119] D. Gatteschi, L. Pardi. A. L. Barra and A. Müller, Mol. Engin. **3**, 157 (1993).

[120] M. R. Pederson, N. Bernstein and J. Kortus, Phys. Rev. Lett. **89**, 097202-1/4 (2002).

Acknowledgment

Without the help of many friends, collaborators and colleagues I would have not been able to come so far.

I would like to thank Prof. J. Monecke for his continued interest in my scientific progress. He has always been available whenever I needed his help or advise.

Mark R. Pederson placed enough trust in me to invite me to join his group at the Center for Computational Materials Science at the Naval Research Laboratory in Washington DC. During the two years there, working on and with NRLMOL he has been a great teacher and real friend. Without his support this work would not have been possible.

Igor Mazin taught me everything I know about superconductivity, but also several things about life. The collaboration with him has been very fruitful and successful. I can only recommend to every postdoc to spent lunch time with Igor, if he offers a PRL just yell.

Working at NRL was a great experience for me, I had the pleasure to work with many outstanding scientists and found a few friends. I would like to thank Marco Fornari for all the time we spent together and John Pask for many interesting discussions.

I had the luck to continue my work at another great place for electronic structure calculations, Abteilung Andersen at MPI FKF in Stuttgart. Ole K. Andersen allowed me to continue to work on things I found interesting and showed lots of understanding for my teaching duties in Freiberg. Many things I thought I do understand I had to revise after talking to Ole. I enjoyed to work with Ove Jepsen and Oleg Dolgov. In particular I thank Ove Jepsen for critically reading the manuscript. Further, I have to thank Olle Gunnarsson for many discussions. Whatever my question was, he always gave a very enlightening answer.

There are many more people which I have to thank, they are just too numerous to be listed here by name.

Last, but not least, I thank Katrin for her support and patience with me over all the years.

Appendix A

Kortus J., Mazin I.I., Belashchenko K.D., Antropov V.P., and Boyer L.L.

Superconductivity of metallic boron in MgB_2

Phys. Rev. Lett. **86**, 4656-4659 (2001)

Superconductivity of Metallic Boron in MgB_2

J. Kortus,[1,2,*] I. I. Mazin,[2] K. D. Belashchenko,[3] V. P. Antropov,[3] and L. L. Boyer[2]
[1]*Georgetown University, Washington, D.C. 20057*
[2]*Center for Computational Materials Science, Code 6390, Naval Research Laboratory, Washington, D.C. 20375*
[3]*Ames Laboratory, ISU, Ames, Iowa 50011*
(Received 29 January 2001)

Boron in MgB_2 forms stacks of honeycomb layers with magnesium as a space filler. Band structure calculations indicate that Mg is substantially ionized, and the bands at the Fermi level derive mainly from B orbitals. Strong bonding with an ionic component and considerable metallic density of states yield a sizable electron-phonon coupling. Together with high phonon frequencies, which we estimate via zone-center frozen phonon calculations to be between 300 and 700 cm^{-1}, this produces a high critical temperature, consistent with recent experiments. Thus MgB_2 can be viewed as an analog of the long sought, but still hypothetical, superconducting metallic hydrogen.

DOI: 10.1103/PhysRevLett.86.4656 PACS numbers: 74.20.Fg, 71.18.+y, 74.25.Jb, 74.70.Ad

Before the discovery of high-temperature superconductors much effort was devoted to boosting the critical temperature of conventional, BCS-Eliashberg superconductors [1]. An exotic and appealing idea going back to the early 1960's was that of metallic hydrogen [2]. The arguments were very simple: due to the light mass, the phonon frequencies in metallic hydrogen would be very high, of the order of several thousand degrees Kelvin, and the prefactor in the BCS formula would be very large, so that even a moderate coupling constant would provide a sizable T_c. This idea can be quantified as follows: for monatomic solids, the electron-phonon coupling (EPC) constant, λ, which enters the BCS equation, can be written in the so-called McMillan-Hopfield form [3], $\lambda = N(0)\langle I^2\rangle/M\langle\omega^2\rangle$, where $N(0)$ is the density of states (DOS) at the Fermi level per spin per atom, $\langle I^2\rangle$ is the properly averaged electron-ion matrix element squared, M is the atomic mass, and $\langle\omega^2\rangle$ is (again, properly averaged) the phonon frequency. The product $M\langle\omega^2\rangle$ does not depend on the mass, but on the force constants only [1], while $\eta = N(0)\langle I^2\rangle$, also known as the Hopfield factor, is a purely electronic property. Correspondingly, light elements, everything else being the same, are beneficial for superconductivity.

Lacking metallic hydrogen, attention was focused upon compounds with light elements: carbides, nitrides (arguably, the superconductivity in fullerenes was a discovery along this road). Indeed, many of them were "high-T_c superconductors" on the contemporary scale: 10–15 K. It was pointed out [4] that $\langle I^2\rangle$ is rather large in these materials due to the relatively high ionicity (although not as high as in MgB_2), but $N(0)$ is rather small. This led to the suggestion of cubic MoN, which would have a larger $N(0)$ than existing nitrides and carbides, as a hypothetical superconductor with $T_c > 30$ K [5].

The recently discovered medium-T_c superconductor MgB_2 [6] with $T_c \gtrsim 39$ K is clearly a continuation of the same idea. The main component, B, is even lighter than C and N. Furthermore, electronic structure calculations show that the compound is not only quite ionic with a sizable DOS, but also has strong covalent B-B bonding (the bonding-antibonding splitting due to in-plane B-B hopping is about 6 eV) and thus exhibits strong electron-phonon interactions. Interestingly, unlike carbides and nitrides, and similar to metallic hydrogen, electrons at the Fermi level (and below) are predominantly B like. Mg s states are pushed up by the B p_z orbitals and fully donate their electrons to the boron-derived conduction bands. In the following we will describe the physics of such "metallic" boron in detail, present an estimate of the EPC constant, and propose some routes for optimizing T_c in this kind of compound.

MgB_2 occurs in the so-called AlB_2 structure. Borons form a primitive honeycomb lattice, consisting of graphite-type sheets stacked with no displacement. The borons form hexagonal prisms with the base diameter of 3.5 Å nearly equal to the height. This creates large, nearly spherical pores for Mg. As in graphite, the intraplanar B-B bonds are much shorter than the distance between the planes, and hence the B-B bonding is strongly anisotropic. However, the interplane bonds are only twice as long as the intraplane ones, as compared to the ratio of 2.4 in graphite, allowing for a significant interplane hopping.

We have calculated the electronic structure of MgB_2 using a general potential LAPW code [7]. For the rigid atomic spheres calculations we used the Stuttgart LMTO code [8]. For the exchange-correlation potential, the generalized gradient approximation of Ref. [9] was employed. Despite the rather simple crystal structure, very few electronic structure calculations for MgB_2 have been reported (a model TB calculation of Burdett and Miller [10] and a recent full-potential LMTO study [11]), and these have concentrated mainly on chemical bonding, paying hardly any attention to transport and electronic properties. The results of our LAPW calculations are shown in Figs. 1 and 2. We note first that there is almost no valence charge inside the Mg muffin-tin (MT) sphere (less than $0.2e$). About half of the total valence charge resides inside the B spheres, and about the same amount in the interstitials. This is partially due to the fact that the chosen LAPW setup employs

 0031-9007/01/86(20)/4656(4)$15.00

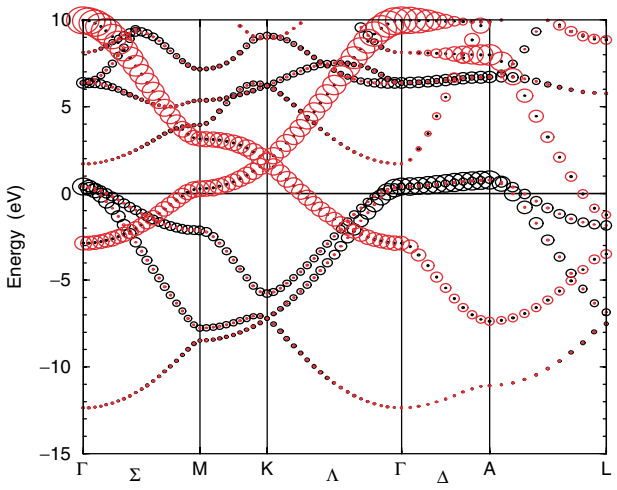

FIG. 1 (color). Band structure of MgB_2 with the B p character. The radii of the red (black) circles are proportional to the B p_z (B $p_{x,y}$) character.

rather small MT spheres for Mg. For the LMTO calculations we used an atomic sphere of nearly the size of the free Mg atom (up to $3.13a_B$), and obtained, as expected, a larger charge of 2.8 electrons. However less than 25% of the charge has s character. The remaining charge of p, d, and f character arises not from Mg electrons but rather from the tails of the B p orbitals and contributions from the interstitials. In fact, one can say that Mg is fully ionized in this compound, however the electrons donated to the system are not localized on the anion, but rather are distributed over the whole crystal.

The resulting band structure can be easily understood in terms of the boron sublattice. The character of the bands is plotted in Fig. 1. We show only the B p character, since other contributions near the Fermi level are very small. Observe two B band systems: two bands are derived from B p_z states and four from B $p_{x,y}$. All these bands are highly dispersive (light), the former being quite isotropic and the latter more two dimensional. Both p_z bands cross the Fermi level (in different parts of the Brillouin zone), but only two bonding $p_{x,y}$ bands do so, and only near the Γ point. They form two small cylindrical Fermi surfaces around the Γ-A line (Fig. 3). However, due to their 2D character, they contribute more than 30% to the total $N(0)$.

In contrast, the p_z bands have 3D character, since the smaller intraplane distance compensates for a smaller ($pp\pi$ vs $pp\sigma$) hopping. In the nearest neighbor tight binding (TB) model their dispersion is $\varepsilon_{\mathbf{k}} = \varepsilon_0 + 2t_{pp\sigma} \times \cos ck_z \pm t_{pp\pi}\sqrt{3 + 2\cos\mathbf{a}_1\mathbf{k} + 2\cos\mathbf{a}_2\mathbf{k} + 2\cos\mathbf{a}_3\mathbf{k}}$ where $\mathbf{a}_{1,2,3}$ are the smallest in-plane lattice vectors. The on-site parameter ε_0 can be found from the eigenvalue at the K point and is ~1.5 eV above the Fermi energy. We estimated $t_{pp\sigma}$ and $t_{pp\pi}$ from the LMTO calculations as ~2.5 and ~1.5 eV, respectively. This model gives a very good description of the p_z band structure near and below the Fermi level, although the antibonding band acquires some additional dispersion by hybridizing with the Mg p band. The role of Mg in forming this band structure can be elucidated by removing the Mg atoms from the lattice entirely and repeating the calculations in this hypothetical structure. The in-plane dispersion of both sets of bands at and below the Fermi level changes very little ($pp\pi$ bands are hardly changed, while the $pp\sigma$ in-plane dispersion changes by ~10%). The k_z dispersion of the p_z bands is increased in MgB_2 as compared with the hypothetical empty B_2 lattice by about 30%, and these bands shift down with respect to the $p_{x,y}$ bands by approximately 1 eV. This shift, as well as the additional dispersion, comes mainly from the hybridization with the empty Mg s band, which is correspondingly pushed further up, increasing the effective ionicity. Substantial k_z dispersion of the p_z bands

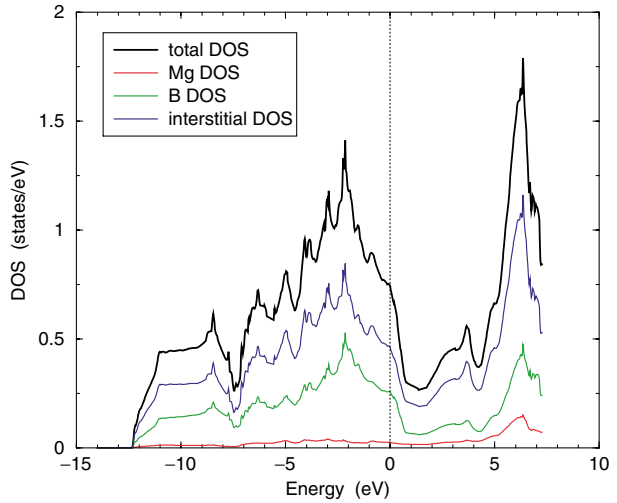

FIG. 2 (color). Total density of states (DOS) and partial DOS for the MgB_2 compound. The small Mg DOS is partially due to the small r_{MT} of $1.8a_B$ used.

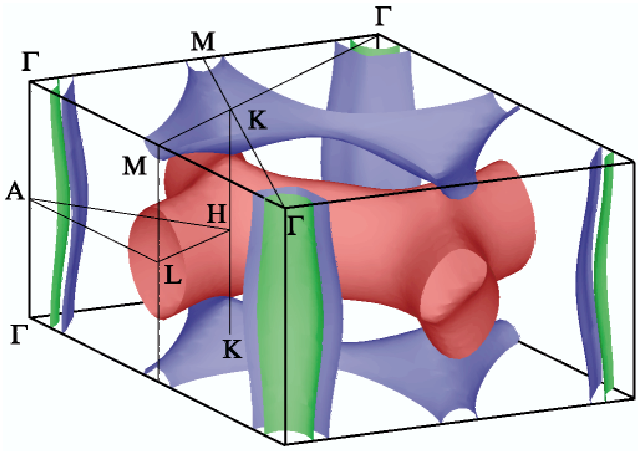

FIG. 3 (color). The Fermi surface of MgB_2. Green and blue cylinders (holelike) come from the bonding $p_{x,y}$ bands, the blue tubular network (holelike) from the bonding p_z bands, and the red (electronlike) tubular network from the antibonding p_z band. The last two surfaces touch at the K point.

produces the Fermi surface which is approximately mirror reflected with respect to a plane between the $k_z = 0$ and $k_z = \pi/c$ planes, one pocket (electronlike) coming from the antibonding and the other (holelike) from the bonding p_z band. The two surfaces touch at one point on the K-H line and form a honeycomb tubular network, replicating in reciprocal space the boron lattice in real space.

The resulting bands are fairly 3D: the average Fermi velocities are $v_{x,y} = 4.90 \times 10^7$ cm/s and $v_z = 4.76 \times 10^7$ cm/s. The plasma frequencies are $\omega_{px,y} = 7.1$ eV and $\omega_{pz} = 6.9$ eV. Correspondingly, we predict fairly isotropic high-temperature electrical resistivity, with the linear slope $d\rho/dT \approx 0.08\lambda_{\rm tr}\ \mu\Omega$ cm/K. The total DOS at the Fermi level is $N(0) = 0.36$ states/spin f.u.

The above described band structure is typical for an sp metal. What is *not* typical is that this particular sp metal is held together by covalent bonding with a substantial ionic component [12], which inevitably leads to a strong electron-phonon interaction. In the following we present a semiquantitative estimate of the corresponding coupling constant, and argue that the fortunate combination of strong bonding, sizable $N(0)$, and high phonon frequency is responsible for the high transition temperature in this compound.

In its most rigorous formulation the McMillan-Hopfield formula reads [1]

$$\lambda = n^{-1} \sum_{ij} \langle N I_{i\alpha} I_{j\beta} \rangle (\Phi^{-1})_{i\alpha,j\beta}\,, \qquad (1)$$

where the indices i, j run over all n ions in the crystal; α, β are Cartesian indices; $\langle N I_{i\alpha} I_{j\beta} \rangle$ is the electron-ion matrix element averaged over the Fermi surface; and $\Phi_{i\alpha,j\beta}$ is the standard force matrix. While this expression is exact, a number of simplifications are needed to make it more practical. One usually neglects the nondiagonal terms and reduces Eq. (1) to one unit cell. The standard justification makes use of the large size of the Fermi surface; see Ref. [1]:

$$\lambda \approx \sum_i \langle N I^2 \rangle_i \Phi_{ii}^{-1} = \sum_i \eta_i (\Phi_{ii})^{-1}. \qquad (2)$$

The quantity $\Phi_{ii} = \partial^2 E_{\rm tot} \partial R_i^2$ is a local quantity, which can be calculated from the total energy differences of frozen zone-center phonons. The Hopfield factor can be calculated in the rigid muffin-tin (or rigid atomic sphere) approximation [13] (RMTA), assuming that the change of the crystal potential due to an ion's displacement can be described by shifting the electronic charge distribution rigidly inside the corresponding atomic sphere. Although expressions for η have been derived for arbitrary site symmetry [14], these are complicated and we will use here simplified formulas [13] formally correct for cubic site symmetry. Then η can be readily calculated from the LMTO potential parameters and partial DOS's. We show the results in Table I.

TABLE I. Partial LMTO DOS, $N(0)$, in eV^{-1}/spin and partial Hopfield factors, η, in mRy/a_B^2, for Mg and B (per atom).

	$N(0)$					η	
l	s	p	d	f	sp	pd	df
Mg	0.018	0.043	0.078	0.019	<1	2	3
B	0.003	0.199	0.010	···	<1	135	···

In order to get an estimate of the phonon spectrum of the system, we calculated all zone-center modes, using the full-potential LAPW method. There are four distinct modes [15]: one silent mode, B_{1g} (two borons displaced along z in opposite directions), one doubly degenerate Raman mode, E_{2g} (in-plane displacements of borons), and two infrared-active modes, which do not involve changes of in-plane bonds: A_{2u} (B and Mg planes moving against each other), and a doubly degenerate E_{1u} mode (B and Mg planes sliding along x, y). Their frequencies are, respectively, 690, 515, 390, and 320 cm^{-1}, and their force constants are 390, 220, 70, and 44 mRy/a_B^2/atom. All calculations were carried out at the experimental lattice constant and c/a ratio [16]. The E_{2g} mode shows strong anharmonicity. While the harmonic frequency calculated from the second derivative of the total energy with respect to the phonon coordinate yields 515 cm^{-1}, a numeric solution for the calculated anharmonic potential results in an anharmonic frequency of 590 cm^{-1}.

Given the physics of the electronic structure described above, it seems likely that the lowest mode couples little with the electrons and that its softness is derived from its in-plane acoustic character. Thus, we excluded it from the calculations of λ below. Correspondingly, the average inverse force matrix for boron is $(\Phi_B)^{-1} = M_B^{-1}\langle\omega^{-2}\rangle = 7.1 a_B^2$/Ry, corresponding to $\langle\omega^{-2}\rangle^{-1/2} \approx 400$ cm^{-1}. Together with the above value for η this gives $\lambda \approx 0.7$ and the logarithmically averaged frequency of the same three modes is $(690 \times 515^2 \times 390)^{0.25} = \langle\omega_{\log}\rangle \approx 500$ cm$^{-1} \approx 700$ K. We can now estimate the critical temperature according to the McMillan formula, $T_c = \frac{\langle\omega_{\log}\rangle}{1.2} \exp[-1.02(1+\lambda)/(\lambda - \mu^* - \mu^*\lambda)]$. Using for the Coulomb pseudopotential μ^* the commonly accepted value 0.1, we obtain $T_c \approx 22$ K.

TABLE II. Comparison of the electron-phonon coupling in Al and in MgB_2. The entries labeled by a question mark are obtained by scaling the RMTA λ by the ratio of $\lambda_{\rm exp}/\lambda_{\rm rmt}$ in Al. $q_{\rm TF}$ is the Thomas-Fermi screening parameter in a_B^{-1}. T_c was calculated by the McMillan formula with $\mu^* = 0.1$. LAPW $N(0)$ is given in eV^{-1}/spin, η in mRy/a_B^2, and $\langle M\omega^2\rangle$ in Ry/a_B^2.

	$N(0)$	$\eta_{\rm rmt}$	$\langle\omega_{\log}\rangle$	$\langle M\omega^2\rangle$	$\lambda_{\rm rmt}$	$T_c(\lambda_{\rm rmt})$	$\lambda_{\rm exp}$	$T_c(\lambda_{\rm exp})$	$T_{c,\rm exp}$	$q_{\rm TF}$
Al	0.15	27	250	0.135	0.2	0	0.4	1.3	1.3	0.73
MgB_2	0.18 (per B)	135	500	0.141	0.7	22	1.4?	70?	39	0.70

It is instructive to compare the calculation above with a typical sp superconductor, Al (Table II). RMTA usually underestimates the electron-ion scattering in sp metals due to the weaker screening than in d metals. Also in Al, λ is underestimated by a factor of 2. The screening properties of MgB_2 are similar to those of Al (they have similar Thomas-Fermi screening lengths), and the electronic properties are similar as well. It is therefore tempting to scale the calculated λ for MgB_2 by the same factor. The scaled results are also shown in Table II and the corresponding T_c is approximately 70 K. Let us emphasize that these numbers should be regarded only as rough estimates. The RMTA in MgB_2 is clearly a worse approximation than in Al. The boron site symmetry is far from cubic and, moreover, large differences in the atomic sphere radii lead to artificial potential jumps at the sphere boundary, a problem for which there is no remedy in RMTA. In other words, with regard to EPC, our calculations should be considered as a qualitative indication of a strong electron-phonon interaction. We can nevertheless be confident of our main qualitative conclusions.

Our main conclusion is that MgB_2, being essentially metallic boron held together by covalent B-B and ionic B-Mg bonding, is electronically a typical sp metal with a typical DOS. Strong bonding induces strong electron-ion scattering and hence strong electron-phonon coupling. An additional benefit is the high frequency of the boron vibrations (while the force constants remain reasonably soft). Superconductivity is mainly due to boron. The light mass and correspondingly large zero-point vibrations ($>0.1a_B$) suggest a possibility of anharmonic and/or nonlinear EPC, and possible deviation of the isotope effect from 100%. Isovalent doping may be beneficial if it increases the density of states $N(0)$. Lattice expansion due to Ca doping should lead to an overall increase of the density of states, and may provide the additional benefit of reduced p_z-s-p_z hopping. Another interesting dopant is Na, which should not only expand the lattice, but also decrease the Fermi level, exposing more of the $p_{x,y}$ bands, which may provide an additional contribution to λ.

Finally, let us outline the directions for further theoretical investigation. First, EPC calculations beyond the RMTA (e.g., in the linear response formalism) are highly desirable and computationally feasible. Second, calculations with full structure optimization for (hypothetical) CaB_2 and BeB_2, and virtual crystal calculations for Na doping should elucidate the effect of isovalent and hole doping, giving some hints toward further optimizing T_c. Work along these lines is currently in progress.

We are thankful to J. E. Pask, C. S. Hellberg, and D. J. Singh for critical reading of the manuscript. This research was supported in part by ONR and by DOE under Contract No. W-7405-82.

Note added.—Since this paper was submitted, a sizable, but incomplete, isotope shift for B [17] (but not for Mg) was obtained, supporting the picture described above.

*Current address: MPI für Festkörperforschung, Postfach 80065, D-70506 Stuttgart, Germany.

[1] *The Problem of High Temperature Superconductivity,* edited by V. L. Ginzburg and D. A. Kirzhnits (Consultant Bureau, New York, 1982).

[2] B. Adler, in *Progress in Very High Pressure Research,* edited by T. Bundy (Wiley, New York, 1960); N. Ashcroft, Phys. Rev. Lett. **21**, 1748 (1968).

[3] W. L. McMillan, Phys. Rev. **167**, 331 (1968).

[4] B. M. Klein and D. A. Papaconstantopulos, Phys. Rev. Lett. **32**, 1193 (1974).

[5] D. A. Papaconstantopulos *et al.,* Nature (London) **308**, 494 (1984).

[6] J. Nagamatsu *et al.,* Nature (London) **410**, 63 (2001).

[7] P. Blaha, K. Schwarz, and J. Luitz, computer code WIEN97, Vienna University of Technology, Vienna, 1997. Improved and updated of original code published by B. Blaha, K. Schwarz, P. Sorantin, and S. B. Trickey, Comput. Phys. Commun. **59**, 399 (1990). We used for all calculations $r_{\mathrm{MT}} \times k_{\max} = 8.0, l_{\max} = 10$, and $G_{\max} = 20$, r_{MT} Mg 1.8 and B $1.5a_B$.

[8] We used two different LMTO setups throughout this work. One was carefully selected to reproduce the full-potential LAPW results near the Fermi surface nearly exactly, and was used essentially as a tool for interpolating the LAPW bands. The relevant parameters were $r_{\mathrm{Mg}} = 3.13$, $r_{\mathrm{B}} = 2.01$. The other was produced by the *lmhart* program (part of the Stuttgart TB-LMTO 4.7 package) which selects the sphere so as to minimize discontinuity in the Hartree potential ($r_{\mathrm{Mg}} = 3.23$, $r_{\mathrm{B}} = 1.87$). The latter is more physical and was used for the EPC calculations. Because of the large Mg sphere, it is important to include f states on Mg, and to perform the final run with the linearization parameters E_ν set to the Fermi level.

[9] J. P. Perdew and Y. Wang, Phys. Rev. B **45**, 13 244 (1992).

[10] J. K. Burdett and G. J. Miller, Chem. Mater. **2**, 12 (1989).

[11] A. I. Ivanovskii and N. I. Medvedeva, Russ. J. Inorg. Chem. **45**, 1234 (2000).

[12] More detailed discussion of bonding in MgB_2 can be found in K. D. Belashchenko, M. van Schilfgaarde, and V. P. Antropov, cond-mat/0102290.

[13] G. Gaspari and B. Gyorffy, Phys. Rev. Lett. **28**, 801 (1972).

[14] I. I. Mazin, S. N. Rashkeev, and S. Y. Savrasov, Phys. Rev. B **42**, 366 (1990).

[15] H. T. Stokes and D. M. Hatch, *Isotropy Subgroups of the 230 Crystallographic Space Groups* (World Scientific, Singapore, 1988).

[16] $a = 3.083$ Å, $c/a = 1.142$; A. Lipp and M. Roder, Z. Anorg. Allg. Chem. **344**, 225 (1966). Calculated numbers differ from these by -0.4 and 0.6%, respectively.

[17] S. L. Bud'ko *et al.,* Phys. Rev. Lett. **86**, 1877 (2001).

Appendix B

Mazin I.I. and Kortus J.

Interpretation of the de Haas - van Alphen experiments in MgB_2

Phys. Rev. B **65**, 180510-1/4 (R) (2002)

PHYSICAL REVIEW B, VOLUME 65, 180510(R)

Interpretation of the de Haas–van Alphen experiments in MgB_2

I. I. Mazin*
Code 6391, Naval Research Laboratory, Washington, DC 20375-5000

Jens Kortus†
Max-Planck-Institut für Festkörperforschung, Heisenbergstrasse 1, D-70569 Stuttgart, Germany
(Received 15 January 2002; published 30 April 2002)

Recent reports on quantum oscillations in MgB_2 provide valuable information on three important aspects of this material: (i) electronic structure near the Fermi level, (ii) disparity of the electron-phonon interaction between the two systems of bands, and (iii) renormalization of spin susceptibility. However, extraction of most of this information requires highly accurate band-structure calculations of the relevant quantities. In this paper we provide such calculations and use them to analyze the experimental data.

DOI: 10.1103/PhysRevB.65.180510 PACS number(s): 74.25.−q, 71.18.+y, 74.70.−b

MgB_2, a superconductor with $T_c \approx 40$ K, has attracted enormous attention in the last year. The most popular model, suggested by Liu *et al.*[1] and Shulga *et al.*,[2] and elaborated upon by Choi *et al.*,[3] is the two-gap model, which, based on the very large interband disparity of the electron-phonon interaction (first noted in Ref. 4), predicts two different gaps for the two different band systems. The calculations[1,3] yield an effective (including an enhancement due to gap variation) electron-phonon coupling constant of the order of 1. On the other hand, the two-gap theory has a serious conceptual problem: Two distinctive gaps may exist only if the interband impurity scattering is very weak. That seems to be in contrast to the experimental observation that even poor quality, high-resistivity samples have very good superconducting properties. It has been argued[5,6] that the specificity of the electronic and crystal structures of MgB_2 results in a peculiar relation among the three relevant relaxation rates, namely that the impurity scattering inside the so-called π band is much stronger than inside the σ band, and the latter, in turn, is much stronger than the interband scattering. However, there has been no direct experimental confirmation of this claim.

On the other hand, some authors[7] argue that the calculated band structure is strongly renormalized by electron-electron interactions not accounted for in the local-density calculations, so that the plasma frequency is a factor of 5 smaller than the calculated one. This would imply an electron-phonon coupling constant less than 0.2. There are claims that infrared spectroscopy supports this point of view,[8,9] although other researchers in the field[5] dispute the interpretation accepted in Refs. 8 and 9. In any case, the fact that all optical experiments until now have been performed on polycrystalline samples undermines their value as a decisive test for the electronic structure calculations.

Single-crystal angular-resolved photoemission spectroscopy[10] (ARPES) measurements agree very well with the calculations.[11] However, some calculated bands were not observed, and, furthermore, ARPES probes only a very thin surface layer and is therefore often not representative of the bulk electronic structure.

Historically, the most reliable probe of the bulk electronic structure has been the de Haas–van Alphen effect (dHvA). Recent observation of this effect in MgB_2 single crystals[12] provides key information to assess the validity of the standard band-structure calculation. Given the fact that most theoretical papers rely on this band structure, the importance of a proper analysis of these data can hardly be overestimated. It must be emphasized that such an analysis requires highly accurate band-structure calculations, i.e., the use of a much finer k-point mesh in the Brillouin zone and a much more accurate integration than is customary in other applications of the band theory. In this paper we present such calculations and show that both Fermiology and effective masses (and hence the Fermi velocities and plasma frequencies) produced by conventional band-structure calculations are in excellent agreement with the experiment, thus giving a strong foundation for the widespread use of this band structure. Furthermore, we show that the calculational predictions of a strong disparity of the electron-phonon interaction in the two-band systems in MgB_2 are supported by the de Haas–van Alphen experiment, and that the scattering rates inside the σ band and between σ and π bands are probably much smaller than inside the π bands.

The Fermi surface of MgB_2 consists of four sheets.[13] Two sheets come primarily from the boron p_x and p_y states, and form slightly (nearly sinusoidally) warped cylinders, σ (bonding) and σ^* (antibonding),[14] and two tubular networks, the bonding one, π, in the Γ ($k_z=0$) plane, and the antibonding one, π^*, in the A ($k_z=\pi/c$) plane. There are six extremal cross sections for the field parallel to k_z (along the ΓA line). These are (1) σ in the Γ plane, (2) σ^* in the Γ plane, (3) π in the Γ plane (''holes'' between the tubes), (4) σ in the A plane, (5) σ^* in the A plane, and (6) π^* in the Γ plane. For a field parallel to k_y (perpendicular to the ΓAM plane) there are two extremal cross sections (tubes' necks), for the π surface (7) and for the π^* surface (8).

We performed highly accurate and well-converged full potential linear augmented plane-wave (LAPW) calculations, using the WIEN-97 package,[15] including local orbitals[16] to relax the linearization errors. We used the generalized gradient approximation of Perdew-Wang[17] for the exchange-correlation potential. By comparing the results with linear muffin-tin orbitals calculations, we found that for a proper description of the σ orbits it is essential to use a full potential method. It is furthermore essential to use a very fine mesh in

TABLE I. Calculated de Haas–van Alphen parameters from present work ($F_{\rm calc}$) compared to the experimental data ($F_{\rm exp}$) of Ref. 12. The masses are given in free-electron mass units.

	Orbit	$F_{\rm calc}$ (T)	$m^{\rm calc}$	$dm^{\rm calc}/dE$ ($\rm Ry^{-1}$)	λ^{a}	$\lvert(1+\lambda)m\rvert^{b}$	$F_{\rm exp}$ (T)	$\lvert(1+\lambda)m\rvert^{\rm exp}$
(1)	σ Γ plane	730	−0.251	1.1	1.25	0.56	540	0.54
(2)	σ^* Γ plane	1589	−0.543	2.7	1.16	1.17		
(3)	π Γ plane	34630	1.96	23	0.43	2.80		
(4)	σ A plane	1756	−0.312	1.2	1.25	0.70	1530	0.66
(5)	σ^* A plane	3393	−0.618	2.3	1.16	1.33		
(6)	π^* Γ plane	31130	−1.00	4.1	0.47	1.47		
(7)	π ΓAM plane	458	−0.246	1.5	0.43	0.35		
(8)	π^* ΓAM plane	2889	0.315	0.8	0.47	0.46	2685	0.45

[a]Computed from Tables 1 and 2 of Ref. 1.
[b]Computed from the preceding columns.

k space; we employed a 38×38×27 mesh, corresponding to 1995 inequivalent **k** points. To achieve sufficient accuracy for the small areas of the orbits 1, 2, 4, 5, 7, and 8, we used an integration engine built in the SURFER program,[18] which internally interpolates the integrand with splines.

The bare (band) masses in the third column of Table I were then calculated by varying the Fermi energy and using the standard formula,

$$m_{\rm dHvA}=\frac{\hbar^2}{2\pi}\frac{dA}{dE}. \tag{1}$$

Here and below we use the notation A for the areas of the orbits in standard units and F for those in Tesla units. In order to obtain the energy derivatives we fitted the calculated $A(E)$ by quadratic polynomials in the ranges of about 0.03 Ry around the Fermi energy. The experimentally observed ''thermal masses'' differ from the ''band'' masses by a renormalization factor of $(1+\lambda)$, where λ is the coupling constant for the interaction of electrons with phonons or other low-energy excitations. For Table I we used the values of λ computed in the following way (see, e.g., Ref. 19): we assumed that the matrix elements of the electron-phonon interaction are constant within each of the four bands (a good approximation, see Ref. 3), but different among the bands and for different interband transitions. If the matrix of the electron-phonon interaction is U_{ij}, where i,j are the band indices, then the mass renormalization in the band i is

$$\lambda_i=\sum_j U_{ij}N_j, \tag{2}$$

where N_j is the partial density of states per spin for the ith band. Recall that the conventional Eliashberg coupling constant is $\lambda=\Sigma_{ij}U_{ij}N_iN_j/\Sigma_iN_i$. The matrix U and the vector N calculated in Ref. 1 were used to compute the fifth column in Table I.

The agreement between the calculated and measured thermal masses can be characterized as excellent. Very importantly, *this agreement is so good only because the calculated electron-phonon coupling differs by a factor of 3 between the σ and π bands*. This is a direct demonstration of this important effect. The agreement between the calculated areas F and the experiment is also very good. Although F_1, F_2, and F_3 are overestimated by 35%, 15%, and 8%, respectively, the absolute values of these errors are only 0.5% (or less) of the total area of the corresponding Brillouin-zone cross sections. Even better appreciation of the significance of these errors can be gained from the observation that shifting the σ band by 6.3 mRy down, and the π^* band by 5.5 mRy up brings the calculated areas to full agreement with the experiment. It is not at all clear whether or not such a small discrepancy with the experiment is meaningful. It is interesting, nevertheless, that after such an adjustment of the band positions the calculated masses agree with the experiment even better: for the three orbits in question the electron-phonon coupling constants deduced from the experiment by taking the ratio of the measured masses to the calculated masses are, respectively, 1.15, 1.12, and 0.43. After the Fermi-level adjustment, they are 1.22, 1.18, and 0.45. It is also worth noting that, for instance, a change in the c/a ratio of 1.5% shifts the σ and π bands with respect to each other by $\approx$12 mRy, or that a shift of the Fermi level by 6 mRy corresponds to a 0.05 e change in the number of electrons. This shows how sensitive the de Haas–van Alphen results are to the crystallography and stoichiometry.

Another important observation reported in Ref. 12 is the so-called ''spin zero.'' This is a suppression of the de Haas–van Alphen amplitude when the difference in the areas (in Tesla units) of the spin-split (by the external field H) cross sections is exactly $H/2$. This effect has been observed for orbit (8) in the field $H=17$ T, when the field was tilted with respect to the crystallographic axis by $\phi=15-18°$. This means that $(F_8^{\uparrow}-F_8^{\downarrow})/\cos(\phi)=8.5$ T, or $\Delta F_8=F_8^{\uparrow}-F_8^{\downarrow}\approx 8.1$ T (note that the angle itself does not depend on the field in which the measurements are performed, but only on the Fermi-surface geometry and Stoner renormalization). It is easy to estimate this splitting in the first approximation, using the data from Table I and the Stoner renormalization of 33%, calculated in Ref. 21: $\Delta A_8=2\pi m\Delta E_{xc}$, where $\Delta E_{xc}=2\mu_B H(1+S)$ is the induced spin splitting of the bands near the Fermi level, enhanced by a Stoner factor $(1+S)$. This formula gives $\Delta F_8\approx 7.1$ T. A caveat here is that the induced spin splitting need not be the same for all bands, in other words, while the *average* S is 0.33, individual S's may

vary from orbit to orbit. To avoid this problem, we performed self-consistent LAPW calculations in an external field of 1.8 kT (still well within the linear-response regime) and measured $d\Delta A_8/dH$ explicitly. Using these results, we found that for the actual field of 17 T, $\Delta F_8 = 6.7$ T, close to, but slightly smaller than the above estimate of 7.1 T. In other words, the calculated Stoner factor for this orbit is $S_8 = 0.26$, smaller than the average over all bands, which is 0.33. Note that the experimental number of 8.1 T can be reconciled with the calculated mass, if S_8 were ≈ 0.5, fairly close to the electron-phonon coupling constant for the same band, 0.47. We, however, believe that the coincidence is accidental, although we do not have any plausible explanation for the noticeable underestimation of the Stoner factor for this orbit. No ''spin-zero'' effect has been observed for the orbit (4), which has essentially the same mass as orbit (8). Our calculations for this orbit give $\Delta F_4 = 6.9$ T; that is, the calculated Stoner factor for this orbit is $S_4 = 0.31$. At the same time, the actual Stoner factor must be either larger than 0.60 or smaller than 0.18, for this orbit not to exhibit the ''spin-zero'' effect [this is neglecting deviations from a cylindrical shape, which are noticeably stronger expressed for this orbit than for the orbit (8)]. Further experimental studies on better samples should give more insight into this problem.

Finally, we would like to discuss the problem of the ''missing orbits.'' The amplitude of the de Haas–van Alphen signal is proportional to[22]

$$H^{-1/2}\frac{X}{\sinh X}\exp\frac{-c\hbar\sqrt{\pi A}}{eHl}\cos\frac{\pi\Delta F}{H}X = \pi^2 mc(1+\lambda)k_B T/\hbar eH,$$

where l is the mean free path for the orbit in question. Thus, it is not surprising that the large orbits (3) and (6) are not observed; the Dingle exponent $c\hbar\sqrt{\pi A}/eHl$ is at least ten times larger than for the other orbits. However, the question remains for the orbits (2), (5), and (7). Let us start with the first two. We observe that, compared to the orbits (1) and (3), both the Dingle factor and the thermal factor are reduced. The latter is smaller because the effective mass $m(1+\lambda)$ is twice larger, which reduces the maximal temperature at which these orbits can be observed by a factor of 2. The former is reduced because both the orbit size, $\sqrt{A}$, is larger, and the mean free path, $l \propto v_F$, (assuming the relaxation time is the same for both σ and σ^* bands), is smaller [from Table 1 of Ref. 21, $v_F(\sigma)/v_F(\sigma^*) \approx 1.4$]. The total reduction of the Dingle exponent compared to orbit (4) is by a factor of 2 for orbit (5), and of 1.4 for orbit (2).

The absence of a signal from the orbit (7) seems puzzling. Its area and its thermal mass are the smallest of all orbits, and the average velocity for this band is the highest (50% higher than for the σ band). A very plausible explanation is that, as conjectured in Ref. 5 and elaborated upon in Ref. 6, the impurity scattering rates differ drastically between the bands. If the dominant defects reside in the Mg plane (e.g., Mg vacancies), then such defects are very weak scatterers for the σ bands for the simple reason that those bands have very little weight at the Mg atoms. However, this simple picture does not explain why orbit (8), originating from the π^* band, apparently has a small relaxation time and therefore is seen in experiment. Its velocity is close to (in fact, 15% smaller than) that of the π band and its linear size is more than twice larger than that of orbit (7), so the scattering rate has to be at least five times larger. We do not have a plausible answer as to why the impurity scattering appears to be so suppressed for this orbit. Possibly, this is related to its parity (while the π band is even with respect to the $z \rightarrow -z$ reflection, the π^* band is odd).

To conclude, we presented highly accurate calculations of the de Haas–van Alphen parameters for MgB_2. Comparison with the experiment reveals (i) absence of any mass (velocity) renormalization apart from that due to phonons; (ii) a good agreement of the calculated cross-section areas with the experiment; (iii) excellent agreement of the calculated electron-phonon coupling with the dHvA mass renormalization, including very large disparity between the coupling of the σ and π bands, which clearly confirms the basic assumption of the two-gap model for superconductivity in MgB_2; (iv) some underestimation, despite a good qualitative agreement, of the calculated and measured Stoner factors for the π bands, (v) indirect evidence of substantially different impurity scattering rates in the σ and π bands, and (vi) a problem that remains to be understood, the total suppression of the neck orbit, associated with the bonding π band, given a clear observation of the much larger orbit from the electronically similar π^* band.

After this work was finished, we learned about similar works by Rosner *et al.*[20] and Harima.[23] Their results, particularly those of Ref. 20, are quite close to ours. Both papers employ similar methods and take full care of the k-mesh convergence. The remaining difference is a good gauge of how reliable such calculations are, in a technical sense.

We are grateful to A. Carrington and J. R. Cooper for numerous extremely enlightening discussions regarding their paper,[12] as well as to O. K. Andersen, O. Jepsen, and O. V. Dolgov for many discussions of the electronic structure and transport properties of MgB_2. We also thank R. Hayn, H. Rosner, and S.-L. Drechsler for their useful comments. J.K. would like to thank the Schloeßmann Foundation for financial support. The work was partially supported by the Office of Naval Research.

*Electronic address: mazin@dave.nrl.navy.mil

†Electronic address: j.kortus@fkf.mpg.de

[1] A.Y. Liu, I.I. Mazin, and J. Kortus, Phys. Rev. Lett. **87**, 087005 (2001).

[2] S.V. Shulga, S.-L. Drechsler, H. Eschrig, H. Rosner, and W. Pickett, cond-mat/0103154 (unpublished).

[3] H.J. Choi, D. Roundy, H. Sun, M.L. Cohen, and S.G. Louie, cond-mat/0111182 (unpublished); cond-mat/0111183 (unpublished).

[4] J.M. An and W.E. Pickett, Phys. Rev. Lett. **86**, 4366 (2001); Y.

Kong, O.V. Dolgov, O. Jepsen, and O.K. Andersen, Phys. Rev. B **64**, 020501 (2001); K.-P. Bohnen, R. Heid, and B. Renker, Phys. Rev. Lett. **86**, 5771 (2001).

[5] A.B. Kuz'menko, F.P. Mena, H.J.A. Molegraaf, D. van der Marel, B. Gorshunov, M. Dressel, I.I. Mazin, J. Kortus, O.V. Dolgov, T. Muranaka, and J. Akimitsu, Solid State Commun. **121**, 479 (2002).

[6] I. I. Mazin, O. K. Andersen, O. Jepsen, O. V. Dolgov, J. Kortus, A. A. Golubov, A. B. Kuzmenko, and D. van der Marel, cond-mat/0204013 (unpublished).

[7] F. Marsiglio, Phys. Rev. Lett. **87**, 247001 (2001).

[8] R.A. Kaindl, M.A. Carnahan, J. Orenstein, D.S. Chemla, H.M. Christen, H.Y. Zhai, M. Paranthaman, and D.H. Lowndes, Phys. Rev. Lett. **88**, 027003 (2001).

[9] J.J. Tu, G.L. Carr, V. Perebeinos, C.C. Homes, M. Strongin, P.B. Allen, W.N. Kang, E.-M. Choi, H.-J. Kim, and S.-I. Lee, Phys. Rev. Lett. **87**, 277001 (2001).

[10] H. Uchiyama, K.M. Shen, S. Lee, A. Damascelli, D.H. Lu, D.L. Feng, Z.-X. Shen, and S. Tajima, Phys. Rev. Lett. **88**, 157002 (2002).

[11] V.D.P. Servedio, S.-L. Drechsler, and T. Mishonov, cond-mat/0111434 (unpublished).

[12] E.A. Yelland, J.R. Cooper, A. Carrington, N.E. Hussey, P.J. Meeson, S. Lee, A. Yamamoto, and S. Tajima, cond-mat/0112392 (unpublished).

[13] J. Kortus, I.I. Mazin, K.D. Belashchenko, V.P. Antropov, and L.L. Boyer, Phys. Rev. Lett. **86**, 4656 (2001).

[14] Formally speaking, there are four σ bands, of which two are bonding in the sense of covalent bonds, and two are antibonding. Of the two bonding bands, one is more bonding than the other (except at the Γ point) due to a favorable combination of p_x and p_y orbitals. In this paper, we call this band σ, and the other $p_{x,y}$ band, crossing the Fermi level, σ^*.

[15] P. Blaha, K. Schwarz, and J. Luitz, Computer code WEIN-97 (Vienna University of Technology, 1997), improved and updated version of the code published by P. Blaha, K. Schwarz, and P. Sorantin, Comput. Phys. Commun. **59**, 399 (1990).

[16] D. Singh, Phys. Rev. B **43**, 6388 (1991).

[17] J.P. Perdew and Y. Wang, Phys. Rev. B **45**, 13 244 (1992).

[18] http://www. goldensoftware.com/products/surfer/surfer. shtml

[19] I.I. Mazin, A.I. Liechtenstein, C.O. Rodriguez, O. Jepsen, and O.K. Andersen, Physica C **209**, 125 (1993).

[20] H. Rosner, J.M. An, W.E. Pickett, and S.-L. Drechsler, cond-mat/0203030 (unpublished); S. Elgazzar, P.M. Oppeneer, S.-L. Drechsler, R. Hayn, and H. Rosner, cond-mat/0201230 (unpublished).

[21] E. Pavarini and I.I. Mazin, Phys. Rev. B **64**, 140504 (2001).

[22] A. Wasserman and M.S. Springford, Adv. Phys. **45**, 471 (1996).

[23] H. Harima, cond-mat/0201452 (unpublished).

Appendix C

Kurmaev E.Z., Lyakhovskaya I.I., Kortus J., Moewes A., Miyata N., Demeter M., Neumann M., Yanagihara M., Watanabe M., Muranaka T. and Akimitsu J.

Electronic structure of MgB_2: X-ray emission and absorption studies

Phys. Rev. B **65** 134509-1/4 (2002)

Electronic structure of MgB_2: X-ray emission and absorption studies

E. Z. Kurmaev,[1] I. I. Lyakhovskaya,[2] J. Kortus,[3] A. Moewes,[4] N. Miyata,[5] M. Demeter,[6] M. Neumann,[6] M. Yanagihara,[5] M. Watanabe,[5] T. Muranaka,[7] and J. Akimitsu[7]

[1]*Institute of Metal Physics, Russian Academy of Sciences-Ural Division, 620219 Yekaterinburg, Russia*

[2]*Institute of Physics, St. Petersburg State University, 198504 St. Petersburg, Russia*

[3]*Max-Planck-Institut für Festkörperforschung, D-70569 Stuttgart, Germany*

[4]*Department of Physics and Engineering Physics, University of Saskatchewan, 116 Science Place, Saskatoon, Saskatchewan, Canada S7N5E2*

[5]*Research Institute for Scientific Measurements, Tohoku University, Sendai 980-8577, Japan*

[6]*University of Osnabrück, Sektion of Physik, D-49069 Osnabrück, Germany*

[7]*Department of Physics, Aoyama-Gakuin University, Tokyo 157-8572, Japan*

(Received 28 August 2001; published 19 March 2002)

Measurements of x-ray emission and absorption spectra of the constituents of MgB_2 are presented. The results obtained are in good agreement with calculated x-ray spectra, with dipole matrix elements taken into account. The comparison of x-ray emission spectra of graphite, AlB_2, and MgB_2 in the binding energy scale supports the idea of charge transfer from σ to π bands, which creates holes at the top of the bonding σ bands and drives the high-T_c superconductivity in MgB_2.

DOI: 10.1103/PhysRevB.65.134509 PACS number(s): 74.70.Ad, 74.25.Jb, 78.70.Dm, 78.70.En

I. INTRODUCTION

The recent discovery of superconductivity in MgB_2 with a T_c close to 40 K (Ref. 1) was an unexpected experimental achievement. Up to now, it is the highest T_c value reported for any binary compound.[2] This value of T_c is much higher than previously expected within the context of BCS theory.[3] Not surprisingly, its discovery has given rise to much experimental and theoretical activity, having raised the possibility of a whole new class of superconductors.

The experimentally observed B isotope shift of T_c (Ref. 4) and other experimental data[5] suggest conventional BCS *s*-wave electron-phonon coupling. However, careful analysis of the temperature and magnetic field dependence of the specific heat[6] suggests anisotropic or multiple gaps. The reported values of $2\Delta/k_BT_c=1.2-4$ from tunneling measurements[7] also raise the possibility of multiple gaps, although the values below the BCS weak coupling limit of 3.5 have been attributed to surface effects. Even though there is growing evidence for conventional BCS *s*-wave electron-phonon coupling, the experimental picture is not yet entirely clear. In addition to theoretical explanations based on BCS theory,[8–10] an alternative explanation based on hole superconductivity has been proposed.[11] Both theories are based on the results of band structure calculations of MgB_2.

X-ray emission and absorption spectroscopies are powerful probes of the electronic structure of solids. Photon emission and absorption involve a transition between electronic states. In the soft x-ray regime, one of the states is a localized, dispersionless core level. This allows for the interpretation of the measured spectra in terms of unoccupied states for absorption and occupied states for emission. Since dipole selection rules govern the transitions to or from the core level, it is actually the angular-momentum-resolved density of states (DOS) that is measured. Furthermore, since the core level is associated with a specific element in the compound, x-ray absorption and emission are also element specific. Finally, they have the advantage of being relatively insensitive to the quality of the sample surface, unlike x-ray photoelectron spectroscopy (XPS) or ultraviolet photoemission, where in order to measure the bulk electronic structure it is necessary to prepare atomically clean, stoichiometric, and ordered surfaces, which are impossible to realize for sintered samples such as MgB_2.

Recently, a high-resolution photoemission study of a sintered powder sample of MgB_2 was carried out,[12] however, the behavior of the spectral function was analyzed only in the vicinity of the Fermi level. In the present paper, the x-ray emission and absorption spectra (XES and XAS) of the constituents have been studied in MgB_2 and related compounds (graphite and AlB_2). The results obtained are compared with the partial density of states and first-principles calculations of the intensities of x-ray spectra which take dipole matrix elements and selection rules into account.

II. EXPERIMENTAL DETAILS

Both pressed powder and sintered polycrystalline MgB_2 samples were used for measurements of the XES. The sintered polycrystalline sample was prepared as described in Ref. 1. X-ray diffraction measurements show that the sample is single phased and electrical resistivity and dc magnetization measurements confirm the onset of a sharp superconducting transition at 39.5 K. The B *K* emission and absorption spectra were studied on Beamline 8.0.1 at the advanced light source (ALS) at Lawrence Berkeley National Laboratory employing the soft x-ray fluorescence endstation.[13] Emitted radiation was measured using a Rowland circle type spectrometer with spherical gratings and a multichannel two-dimensional detector. The measurements of the Mg *L*-emission spectra were performed using an ultrasoft x-ray grating spectrometer ($R=1$ m,$n=600$ l/mm) with electron excitation.[14] The B $K\alpha$ and Mg $L_{2,3}$ XES were measured with excitation energies far from the B $1s$ and Mg $2p$ thresh-

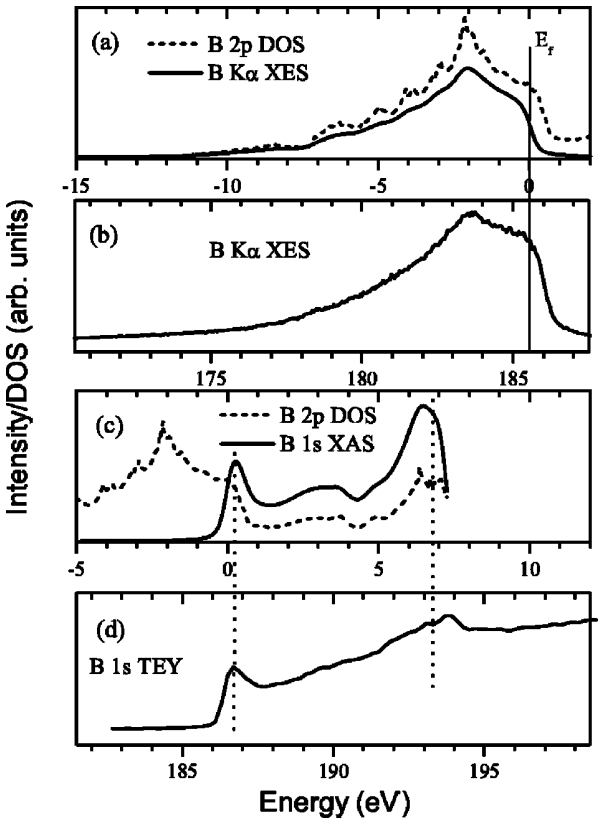

FIG. 1. Calculated (a,c) and experimental (b,d) B *K* emission and absorption spectra of MgB_2. The emission spectrum was obtained from electron excitation far from resonance and is an accumulation of several scans. The absorption spectrum was recorded from the total electron yield (TEY) sample drain current using photons from a synchrotron source.

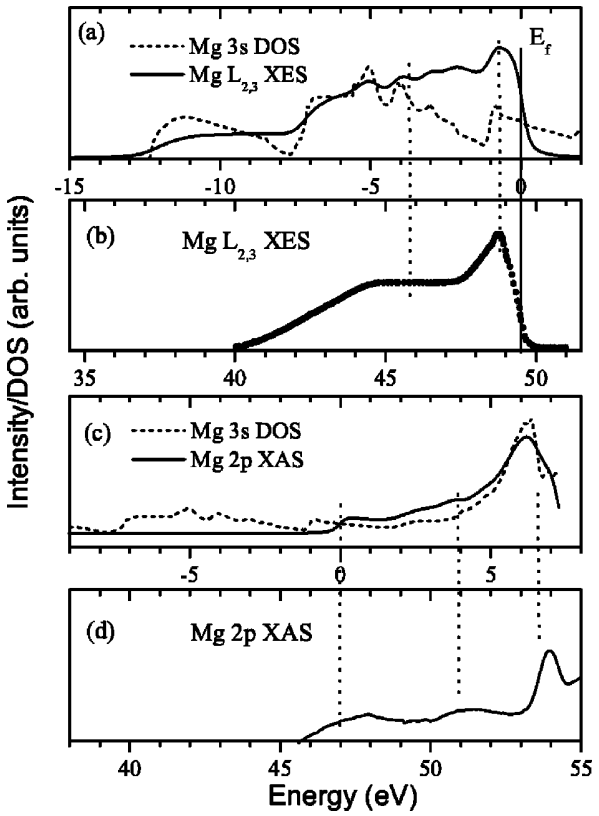

FIG. 2. Calculated (a,c) and experimental (b,d) Mg *L* emission and absorption spectra of MgB_2. The density of states is significantly changed by the dipole matrix elements, which are necessary in order to recover the experimental XES shape.

olds (nonresonant spectra), with an energy resolution of 0.3 eV.

The Mg $2p$ absorption spectra were measured at the beamline BL-12A at the Photon Factory in KEK using photons from a synchrotron source. The energy resolution near the Mg $2p$ threshold (50 eV) is 0.5 eV, using a 0.1 mm monochromator slit width. For Mg $2p$ measurements, we used a Si filter despite the Si $2p$ absorption threshold at about 100 eV because at this beamline non-negligible second order light is included in this energy region. The absorption spectra were taken by recording the total electron yield (TEY) sample drain current. To remove surface contamination before the measurements, the sample was scraped with sandpaper and then striped off with vinyl tape repeatedly until the mark left on the tape was uniform. The vacuum was below 1.0×10^{-6} Torr and the measurements were carried out at room temperature.

In order to determine the position of the Fermi level and convert x-ray spectra to the binding energy scale of XPS (difference of measured XES energies and a selected XPS core level energy), B $1s$ and Mg $2p$ core levels were measured. As mentioned above, XPS for valence band states is very sensitive to surface contamination, nevertheless the binding energies of core levels can be determined after cleaning the surface. The XPS measurements have been carried out with an ESCA spectrometer manufactured by Physical Electronics (PHI 5600 ci). The monochromatized Al $K\alpha$ radiation had a full width at half maximum (FWHM) of 0.3 eV and combined with the energy resolution of the analyzer (1.5% of the pass energy) results in an estimated energy resolution of somewhat less than 0.35 eV. XPS measurements of a MgB_2 sample fractured in high vacuum have shown less oxygen content on the surface than those of sintered material. Further reduction of the oxygen content was achieved by ion etching. After cleaning the surface, we obtained the following values for the binding energies associated with the core levels: B $1s$ (185.5 eV) and Mg $2p$ (49.5 eV). These results agree well with recent XPS studies of MgB_2 (the Mg $2p$ core level energy agrees within 0.2 eV)[15] which shows that the XPS core levels are not significantly influenced by oxidized surfaces, as shown in this study by comparing as-grown and etched surfaces in which the oxidized layer is effectively removed. This supports the use of these values in Fig. 3 to convert XES spectra to the binding energy scale.

III. RESULTS AND DISCUSSION

The states at the Fermi level derive primarily from B and so the resulting band structure can be understood in terms of the boron sublattice. Mg can be described as ionized (Mg^{2+})

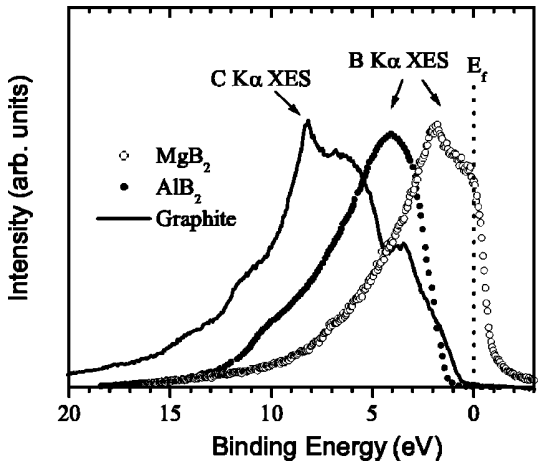

FIG. 3. Comparison of x-ray emission spectra of hexagonal graphite, AlB_2, and MgB_2 using the binding energy scale (difference of XES energies and the $2p$ core level energy obtained from XPS). The major maximum originates from σ (sp^2) states in all materials. The observed shift from graphite to MgB_2 supports the theoretical results of Ref. 9.

in this compound. However, the electrons donated to the system are not localized on the anions, but rather are distributed over the whole crystal. The σ (sp^2) bonding states which have B p_{xy} character are unfilled, in contrast to graphite where the σ states are completely filled and form strong covalent bonds. These σ states form two small cylindrical Fermi surfaces around the Γ-A line and the holes at the top of the bonding σ bands are believed to couple strongly to optical B-B modes and to play a key role in the superconductivity of MgB_2.

Using the full potential LAPW code WIEN97,[16] we calculated the near edge absorption and emission spectra. According to the final-state rule formulated by von Barth and Grossmann,[17] accurate XES and XAS of simple metals may be obtained from ordinary one-electron theory if the relevant dipole matrix elements are calculated from valence functions obtained in the potential of the final state of the x-ray process: in other words, a potential reflecting the fully screened core hole for absorption but not for emission. Because we neglected core relaxation effects in our calculations, we expect significantly better agreement between theory and experiment for emission spectra. The calculated spectra are Lorentz broadened with a spectrometer broadening of 0.35 eV, with additional lifetime broadening for emission spectra.

Theoretical B K emission and absorption spectra of MgB_2, which according to dipole selection rules ($1s \rightarrow 2p$ transition) probe B $2p$ occupied and unoccupied states, respectively, are presented in Figs. 1(a),1(c). These calculations show that the intensity distributions of B K emission and absorption follow the B $2p$ partial density of states very closely because the radial dipole matrix elements are monotonically increasing functions of energy within the valence and conduction bands. The experimental B K emission and absorption spectra [Figs. 1(b),1(d)] are in good agreement with the calculated spectra. Note that the position of the Fermi level of XAS cannot be determined with the help of XPS measurements of core levels due to the different final states. The experimental and calculated XAS spectra shown in Figs. 1 and 2 are compared by aligning the Fermi levels. Our results are also in good agreement with other recent experimental studies.[18,19] Callcott *et al.*[18] have reported soft x-ray fluorescence measurements and also XAS for the K edge of B in MgB_2. Comparing their results to our TEY [Fig. 1(d)] we find similar structures around 187 and 193 eV as observed in Ref. 18. Similar results were also obtained by Nakamura *et al.*[19] We do not find the peak labeled C in Ref. 18 around 195 eV, which was associated with boron oxide. We also obtained good agreement comparing our XES results with other B K-emission experimental data.[18,19]

Calculated Mg L emission and absorption spectra which probe occupied and unoccupied Mg $3s$ states are shown in Figs. 2(a),2(c). The intensity distribution associated with the Mg L emission differs somewhat from the Mg $3s$ partial DOS. The DOS is significantly changed by the dipole matrix elements which are necessary in order to recover the experimental XES shape. The contribution to the x-ray intensity is larger for states near the Fermi level relative to those at the bottom of the valence band, in accordance with the energy dependence of the radial dipole matrix elements. Again, we note reasonable agreement between the calculated [Figs. 2(a),2(c)] and experimental spectra [Figs. 2(b),2(d)].

All density-functional calculations appear to agree that Mg is substantially ionized.[8–10] In order to provide direct experimental evidence for charge transfer from Mg, we compared the Mg L emission spectrum in MgB_2 to that in pure Mg metal. The shift of the Mg core $2p$ level with respect to the Fermi level contains this information and will be called chemical shift. This does not involve counting of electrons in order to obtain the chemical potential, which would depend critically on the shape of the bands. Normally, one would expect a core level shift towards higher binding energies (positive shift) in losing valence charge because less electrons screen the Coulomb potential weaker and therefore the electrons are bound stronger.

Band structure calculations reveal, the Mg $2p$ level shows significant hybridization with the B p_z level, which raises the former while lowering the latter, in difference to the simple picture outlined above. The mechanism is similar to an interacting two-level system, where new states are formed, one level is lowered in energy and the other level is pushed up in energy proportional to the overlap (hybridization) between the states.

A negative chemical shift of about 0.5 eV is found in the MgB_2 spectrum with respect to that of pure Mg, which we hold as evidence for charge transfer from Mg to B atoms in this compound. The same negative chemical shift of 0.5 eV has been observed recently in XPS measurements[15] as well.

This is a very important effect because it lowers the π (p_z) bands relative to the bonding σ (sp^2) bands. This lowering of the B π bands relative to the σ bands, compared to graphite, causes $\sigma \rightarrow \pi$ charge transfer and σ-band hole doping, driving the superconductivity in MgB_2.[9] To investigate this prediction further, we compared the $K\alpha$ XES ($2p \rightarrow 1s$ transition) for graphite, AlB_2, and MgB_2 by alignment of the Fermi levels which were determined in the binding

energy scale using XPS measurements of core levels. B $1s$ (MgB_2) = 185.5 eV, B $1s$ (AlB_2) = 188.5 eV,[20] and C $1s$ (graphite) = 284.5 eV (Ref. 20) (Fig. 3). As the figure shows, the major maximum originating from σ states is shifted in MgB_2 towards the Fermi level with respect to that of graphite. AlB_2 occupies an intermediate position due to the higher electron concentration compared to MgB_2 which results in filling of the σ bands, decreasing $N(E_f)$ and finally destroying superconductivity.

IV. CONCLUSION

In conclusion, we have measured x-ray emission and absorption spectra of the constituents of the new superconductor MgB_2 and found good agreement with results of band structure calculations and in particular calculations of intensities of x-ray spectra taking the necessary matrix elements into account. Further, according to our findings magnesium is positively charged in this compound, which supports the results of electronic structure calculations. The comparison of x-ray emission spectra of graphite, AlB_2, and MgB_2 supports the idea of superconductivity driven by hole doping of the covalent σ bands. While the experimental results of our study cannot give direct insight into the mechanism of the superconductivity, they do support and lend credence to the standard band structure methods used in the theoretical analysis of this new and exciting material. This information could prove important in understanding and answering the questions which still exist.

ACKNOWLEDGMENTS

We thank I. I. Mazin and O. Gunnarson for helpful discussions and comments and J. E. Pask for a critical reading of the manuscript. The Russian State Program on Superconductivity, Russian Foundation for Basic Research (Project No. 00-15-96575) and NATO Collaborative Linkage Grant supported this work. J.K. would like to thank the Schloeßmann Foundation for financial support. Funding by the President's NSERC fund of the University of Saskatchewan is gratefully acknowledged.

[1] J. Nagamatsu, N. Nakagawa, T. Muronaka, Y. Zenitani, and J. Akimitsu, Nature (London) **410**, 63 (2001).

[2] S.V. Vonsovsky, Yu.A. Izyumov, and E.Z. Kurmaev, *Superconductivity of Transitional Metals, Their Alloys and Compounds* (Springer, Berlin, 1982).

[3] W.L. McMillan, Phys. Rev. **167**, 331 (1968).

[4] S.L. Bud'ko, G. Lapertot, C. Petrovic, C.E. Cunningham, N. Anderson, and P.C. Canfield, Phys. Rev. Lett. **86**, 1877 (2001).

[5] D. K. Finnemore, J. E. Ostenson, S. L. Bud'ko, G. Lapertot, and P. C. Canfield, Phys. Rev. Lett. **86**, 2420 (2001); B. Lorenz, R. L. Meng, and C. W. Chu, Phys. Rev. B **64**, 012507 (2001); P. C. Canfield, D. K. Finnemore, S. L. Bud'ko, J. E. Ostenson, G. Lapertot, C. E. Cunningham, and C. Petrovic, Phys. Rev. Lett. **86**, 2423 (2001).

[6] R.K. Kremer, B.J. Gibson, and K. Ahn, cond-mat/0102432 (unpublished); Y. Wang, T. Plackowski, and A. Junod, Physica C **355**, 179 (2001); F. Bouquet, R. A. Fisher, N. E. Phillips, D. G. Hinks, and J. D. Jorgensen, Phys. Rev. Lett. **87**, 047001 (2001).

[7] G. Karapetrov, M. Iavarone, W. K. Kwok, G. W. Crabtree, and D. G. Hinks, Phys. Rev. Lett. **86**, 4374 (2001); G. Rubio-Bollinger, H. Suderow, and S. Vieira, *ibid.* **86**, 5582 (2001); H. Schmidt, J. F. Zasadzinski, K. E. Gray, and D. G. Hinks, Phys. Rev. B **63**, 220504(R) (2001); A. Sharoni, I. Felner, and O. Millo, *ibid.* **63**, 220508(R) (2001).

[8] J. Kortus, I.I. Mazin, K.D. Belashenko, V.P. Antropov, and L.L. Boyer, Phys. Rev. Lett. **86**, 4656 (2001); A.Y. Liu, I.I. Mazin, and J. Kortus, Phys. Rev. Lett. **87**, 087005 (2001).

[9] J.M. An and W.E. Pickett, Phys. Rev. Lett. **86**, 4366 (2001).

[10] Y. Kong, O.V. Dolgov, O. Jepsen, and O.K. Andersen, Phys. Rev. B **64**, 020501(R) (2001).

[11] J.E. Hirsch, Phys. Lett. A **282**, 392 (2001).

[12] T. Takahashi, T. Sato, S. Souma, T. Muranaka, and J. Akimitsu, Phys. Rev. Lett. **86**, 4915 (2001).

[13] J. J. Jia, T. A. Callcott, J. Yurkas, A. W. Ellis, F. J. Himpsel, M. G. Samant, J. Stöhr, D. L. Ederer, J. A. Carlisle, E. A. Hudson, L. J. Terminello, D. K. Shuh, and R. C. C. Perera, Rev. Sci. Instrum. **66**, 1394 (1995).

[14] A.P. Lukirsky, Izv. Akad. Nauk SSSR, Ser. Fiz. **25**, 913 (1961).

[15] R. P. Vasquez, C. U. Jung, M.-S. Park, H.-J. Kim, J. Y. Kim, and S.-I. Lee, Phys. Rev. B **64**, 052510 (2001).

[16] P. Blaha, K. Schwarz, and J. Luitz, WIEN97, a FLAPW package for calculating crystal properties, Vienna, Austria, 1999.

[17] U. von Barth and G. Grossmann, Solid State Commun. **32**, 645 (1979); U. von Barth and G. Grossmann, Phys. Rev. B **25**, 5150 (1982).

[18] T. A. Callcott, L. Lin, G. T. Woods, G. P. Zhang, J. R. Thompson, M. Paranthaman, and D. L. Ederer, Phys. Rev. B **64**, 132504 (2001).

[19] J. Nakamura, N. Yamada, K. Kuroki, T. A. Callcott, D. L. Ederer, J. D. Denlinger, and R. C. C. Perera, Phys. Rev. B **64**, 174504 (2001).

[20] J.F. Moulder, W.F. Stickle, P.E. Sobol, and K.D. Bomben, *Handbook of X-ray Photoelectron Spectroscopy* (Perkin-Elmer, Eden Prairie, MN, 1992).

Appendix D

Dietrich M., Kortus J., Cordts W. and Unterricker S.

Electric Field Gradients in Wurtzite - Type Semiconductors

phys. stat. sol. (b) **207**, 13-17 (1998)

phys. stat. sol. (b) **207**, 13 (1998)

Subject classification: 71.15.–m; 76.20.+q; S7; S8; S10

Electric Field Gradients in Wurtzite-Type Semiconductors

M. DIETRICH (a), J. KORTUS (b), W. CORDTS (b), and S. UNTERRICKER (a)

(a) Institut für Angewandte Physik and (b) Institut für Theoretische Physik,

Technische Universität Bergakademie Freiberg, Bernhard-von-Cotta-Str. 4, D-09596 Freiberg, Germany
phone: +49-3731-392593; Fax: +49-3731-394004; e-mail: unterr@tu-freiberg.de

(Received December 18, 1997)

Electric field gradients (efg) in binary wurtzite-type semiconductors have been calculated self-consistently by application of the program WIEN 95 which is based on the LAPW method. The results were compared with measured efg at the A- and B-sites. All efg are small and they are largely influenced by the parameter u, which describes the displacement of the anion and cation sublattices and which has a low experimental accuracy. From the minimum of the total energy the reliable u parameters can be determined for substances where no experimental values exist. These u parameters show a linear dependence on the axis ratio c/a.

1. Introduction

By the nuclear quadrupole interaction the microscopic environment of suitable probe nuclei in noncubic solids especially semiconductors can be investigated. Thereby the quadrupole frequencies depend on the electric field gradient (efg) V_{zz} at the probe site and on the nuclear quadrupole moment Q. Methods like nuclear magnetic resonance (NMR), double resonance (ENDOR), Mössbauer effect and perturbed angular correlations (PAC) can be used. One of the aims of these investigations is the study of defects in semiconductors [1]. On the other side the efg at the position of a nuclear probe can be used to test very sensitively the quality of a calculated electronic charge distribution. This holds for nuclear probes which can be both impurities and host atoms in the semiconductors investigated. Thereby the calculation of the host atom case is much simpler and it is a prerequisite for realistic calculations of impurity configurations.

There is a group of binary semiconductors of types $A^{III}B^{V}$, $A^{II}B^{VI}$ and $A^{I}B^{VII}$ which crystallize in the noncubic wurtzite structure. Quadrupole coupling constants $\nu_Q = eQV_{zz}/h$ are known for many of the cations and anions in such semiconductors. The theoretical interpretation of the measured efg was carried out in the past by simple point charge estimations or more realistically with regard to the polarization of the ions [2 to 4]. Today it is possible to calculate by first principle methods the electronic structure and the efg in such compounds considering all electrons. Thereby computations with suitable clusters [5] or with periodic lattices are performed. We used the WIEN 95-code of Blaha and Schwarz [6,7] which is based on the LAPW-method (full potential linearized augmented plane waves).

The wurtzite structure consists of two hexagonal close packed sublattices which are displaced in c-direction by uc. The structure parameters of the wurtzite compounds are the lattice constant a, the axis ratio c/a and the parameter u. For most of the com-

pounds the *c*/*a* ratio differs more or less from the ideal value $\sqrt{8/3} = 1.633$, and also the parameter *u* deviates from its ideal value 3/8 = 0.375. This means that the tetrahedra of next neighbours are slightly distorted. Only the lattice constant *a* and the *c*/*a* ratio can be determined from the positions of the X-ray reflections with high accuracy. For the evaluation of the parameter *u* a structure refinement is necessary. Thereby the intensities of the reflections must be determined accurately and the corresponding structure amplitudes have to be fitted to those of the real wurtzite structure with a defined *u* parameter. Such a procedure has a limited accuracy. Therefore, the *u* parameter has a larger uncertainty than the lattice parameters *a* and *c*/*a*. Beside this all lattice parameters are slightly influenced by the growth conditions and the defect concentration of the specimens.

2. Calculation of Charge Distributions and Electric Field Gradients

The electric field gradient (efg) at the position of a probe nucleus is a traceless symmetric tensor which is determined by the anisotropy of the charge distribution around the probe. It is defined by the second derivative of the electric potential leading to the principal component of the tensor V_{zz} and the asymmetry parameter $\eta = (V_{xx} - V_{yy})/V_{zz}$. In the wurtzite lattice we have a threefold axis and therefore $\eta = 0$. The quadrupole frequencies depend only on V_{zz}.

Today it is possible to calculate the charge distribution $\varrho(\mathbf{r})$ in a crystal self-consistently considering the full electronic structure. Electric field gradients at the positions of lattice points can be calculated in an adequate manner. In the WIEN 95-code [7] the full potential is determined from the self-consistent charge density distribution. In the LAPW method a scalar relativistic version without spin–orbit coupling was used.

Well converged solutions were found for $R_{\mathrm{cut}}K_{\mathrm{max}} \leq 8$, where K_{max} is the plane wave cut-off and R_{cut} is the smallest of all atomic sphere radii. Partial waves up to $l = 12$ inside atomic spheres and 24 *k*-points in the irreducible wedge of the Brillouin zone

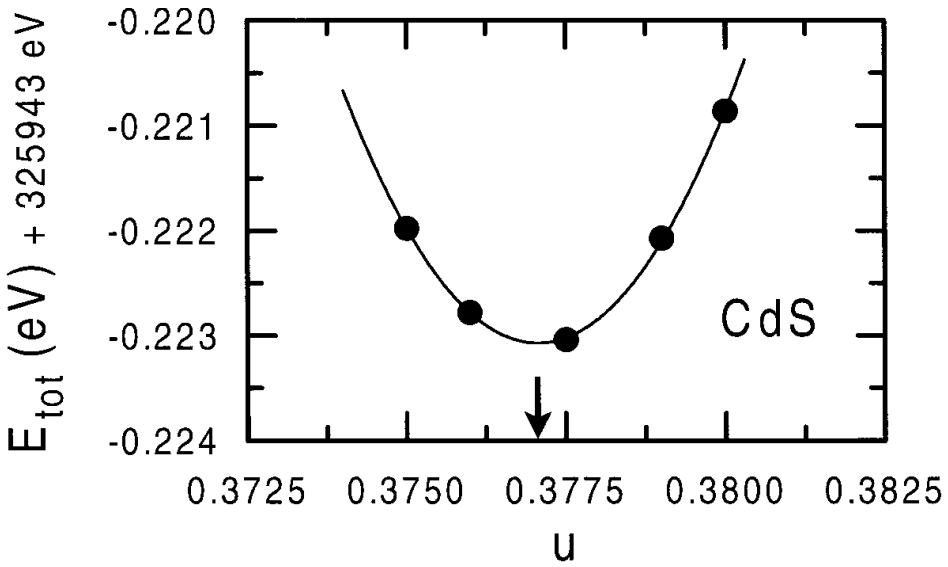

Fig. 1. The total energy in dependence on the parameter *u* for CdS. The minimum (arrow) is nearby the experimental value *u* = 0.3775 [18]. The relative depth of the minimum is very small. The total binding energy of all electrons of the two Cd- and the two S-atoms in the elementary cell is about 325943 eV

were used in maximum. The convergence was checked by the use of different basis sets. The exchange and correlation effects are treated within density functional theory by the standard exchange correlation potential suggested by Perdew and Wang [8].

The efg V_{zz} is strongly influenced by the u parameter which has a relatively large uncertainty. For some of the substances there are no experimental values available. Therefore, we determined a reliable u parameter from the minimum of the total energy on the basis of the experimental a and c/a parameters. For this the iteration was stopped, when the energy convergence was one order of magnitude better than the total energy changes introduced by varying the u parameter. Fig. 1 shows such an $E_{\mathrm{tot}}(u)$ dependence for the case of CdS. The minimum (u = 0.3771) is nearby the experimental u parameter (u = 0.3775). In ZnO we have the same situation. This encouraged us to take the theoretical u parameters for the calculation of the efg in the cases of AlN (u = 0.3818), GaN (u = 0.3770) and ZnS (u = 0.3748), where we could not find any experimental u parameters in the literature.

3. Results

We have calculated the efg in AlN, ZnO, BeO, CdS, GaN, CdSe, AgI and ZnS by the WIEN 95-code [7]. The results for the A- and B-positions are listed in Table 1.

There are linear dependences of the A- and B-efg on the u parameters. This result is also known from qualitative theories [2,3]. The slope of $V_{zz}(u)$ is positive for cations and negative for anions. This is demonstrated for CdS in Fig. 2.

The experimental efg can also be found in Table 1. In some cases the quadrupole coupling constants were determined by different methods and with high accuracy (ZnO: ^{67}Zn Mössbauer results [9], ^{67}Zn NMR results [4] and ^{67}Zn as well as ^{17}O double resonance results [10]). In other cases the efg could only be estimated from

Table 1

Theoretical and experimental efg V_{zz} (in 10^{21} V/m^2) at A- and B-sites for eight binary semiconductors with wurtzite-type structure. The substances are arranged with increasing c/a ratio. Only in the case of ZnO at the A-site the sign of the experimental efg is known from Mössbauer investigations [9]. The theoretically estimated u parameters are marked by an asterisk

	substance	AlN	ZnO	BeO	CdS	GaN	CdSe	AgI	ZnS
	c/a	1.601	1.602	1.622	1.623	1.626	1.631	1.635	1.637
	u	*0.3818	0.3826	0.3786	0.3775	*0.3770	0.3767	0.3747	*0.3748
A-site V_{zz}	theor.	+0.47	+0.91	+0.041	+0.41	+0.46	+0.47	−0.015	+0.025
	exp.	0.61	+0.66	0.032	0.36	0.705	0.24		<0.14
	probe	^{27}Al	^{67}Zn	^{9}Be	^{111}Cd	^{71}Ga	^{111}Cd		^{67}Zn
	ref.	[12]	[9, 10]	[13, 14]	[3, 15]	[10]	[3, 16]		[4]
B-site V_{zz}	theor.	−0.010	−0.38	+0.12	−0.16	+0.019	−0.053	+0.44	+0.18
	exp.		0.23		<0.65	0.079		0.53	0.32
	probe		^{17}O		^{33}S	^{14}N		^{127}I	^{33}S
	ref.		[10]		[11]	[10]		[17]	[4]

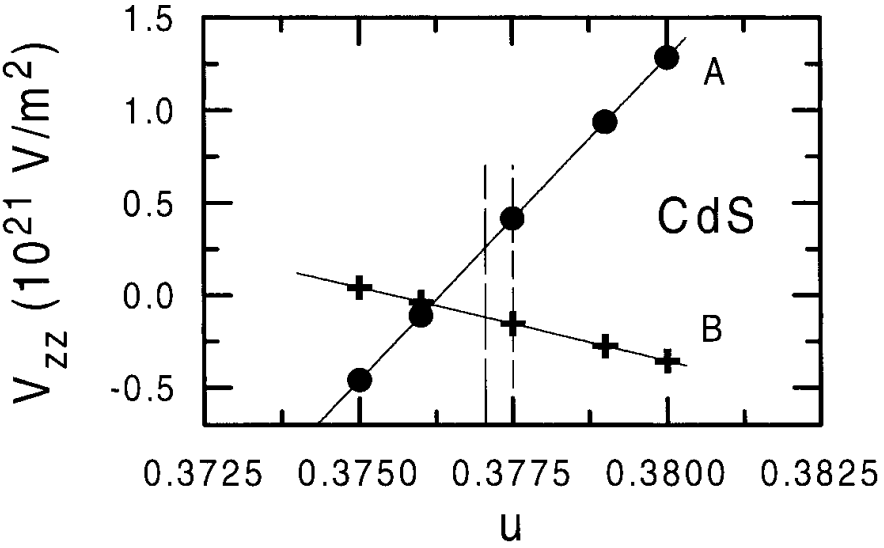

Fig. 2. The calculated efg V_{zz} for CdS at the A- and B-sites in dependence on the parameter u. The vertical lines correspond to the experimental (0.3775) and the theoretical (0.3771) u parameter (calculated from the minimum of the total energy, Fig. 1)

the line broadening (ZnS: ^{67}Zn NMR result [4]). We could not consider all experimental results from the literature in Table 1. For most of the experimental efg the signs are unknown.

4. Discussion

The wurtzite structure and the cubic zincblende structure are very similar. In both cases we have a tetrahedral coordination of next neighbours and some of the compounds are dimorphous (e.g. ZnS, AgI). In the zincblende structure the efg at the lattice sites vanish because of the cubic symmetry. Therefore, the efg in the wurtzite compounds are very small in most cases and they show a strong dependence on the structure parameters. This situation is described in a point charge model by a small difference of two large values, the efg of the cation and the anion sublattices.

If we compare the theoretical and experimental efg V_{zz} in Table 1, we have to consider that the nuclear quadrupole moments, the quadrupole frequencies and the structure parameters have larger uncertainties in some cases. The situation for CdS is represented in Fig. 2. We see a very strong dependence of the A- and B-site efg on the u parameter. A small change of u results in a large relative change of V_{zz}. Although the difference of the experimental (0.3775) and the theoretical (0.3771) u parameter is small the corresponding A-site-efg of 0.41×10^{21} V/m^2 and 0.25×10^{21} V/m^2 differ significantly. The experimental efg (0.36×10^{21} V/m^2) lies in between. At the B-site we could only find $V_{zz} < 0.65\times10^{21}$ V/m^2 from a ^{33}S-NMR experiment [11]. Therefore, in these cases of very small efg the calculated values respond very sensitively to crystallographic uncertainties. The situation is much better if we have compound semiconductors with large efg [19]. As a whole the correspondence between theory and experiment is satisfying also for wurtzite-type compounds (Table 1).

Further essential results are the theoretical u parameters determined by the minima of the total energy. By given lattice parameters a and c/a the total energy of all electrons in the elementary cell depends on the u parameter. For the correct structure the

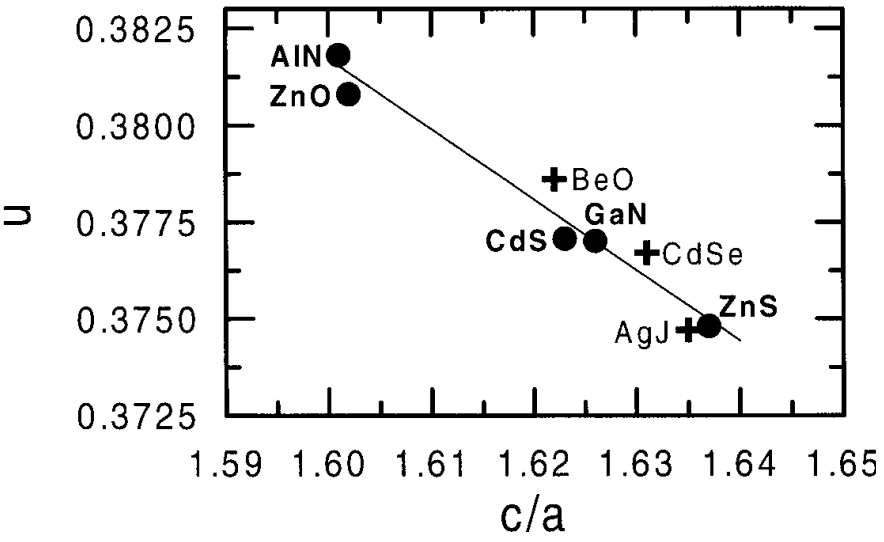

Fig. 3. Correlation between u and the axis ratio c/a. Full circles: theoretical u parameters for AlN, ZnO, CdS, GaN and ZnS, crosses: experimental u values

$E_{\text{tot}}(u)$ dependence must have a minimum. This minimum is very flat if we compare its depth with the total energy. Nevertheless the minimum has the correct position for substances where experimental u parameters exist. Theoretical u parameters were determined for the substances AlN, ZnO, CdS, GaN and ZnS. These u parameters show a linear dependence on the axis ratio c/a whereby the experimental u parameters of other substances are consistent with this linear dependence (Fig. 3). Such a linear dependence between u and c/a was assumed in [3] too.

References

[1] G. Langouche (Ed.), Hyperfine Interaction of Defects in Semiconductors, Elsevier Publ. Co., Amsterdam 1992.
[2] T. T. Taylor and T. P. Das, Phys. Rev. **133**, A1327 (1964).
[3] S. Unterricker and F. Schneider, Hyperfine Interactions **39**, 39 (1988).
[4] T. J. Bastow and S. N. Stuart, phys. stat. sol. (b) **145**, 719 (1988).
[5] D. W. Mitchell, S. B. Sulaiman, N. Sahoo, T. P. Das, W. Potzel, and G. M. Kalvius, Phys. Rev. B **44**, 6728 (1991).
[6] K. Schwarz and P. Blaha, Z. Naturf. **47a**, 197 (1992).
[7] P. Blaha, K. Schwarz, P. Dufek, and R. Augustyn, WIEN 95, Technical University of Vienna, 1995.
[8] J. P. Perdew and Y. Wang, Phys. Rev. B **45**, 1324 (1992).
[9] C. Schäfer, W. Potzel, W. Adlassnig, P. Pötting, E. Ikonen, and G. M. Kalvius, Phys. Rev. B **37**, 7247 (1988).
[10] G. Denninger and D. Reiser, Phys. Rev. B **55**, 5073 (1997).
[11] T. Kushida and A. H. Silver, Phys. Rev. **137**, A1591 (1965).
[12] Oc Hee Han, H. K. C. Timken, and E. Oldfield, J. Chem. Phys. **89**, 6046 (1988).
[13] G. J. Troup and J. A. Walter, J. Nuclear Mater. **14**, 272 (1964).
[14] J. F. Hon, Phys. Rev. **124**, 1368 (1961).
[15] E. Berthold, M. Frank, F. Gubitz, W. Kreische, C. Ott, B. Roseler, F. Schwab, K. Stammler, and G. Weeske, Appl. Phys. Lett. **58**, 461 (1991).
[16] H. Barfuss, G. Böhnlein, H. Hohenstein, W. Kreische, H. Niedrig, H. Appel, R. Heidinger, J. Randies, G. Then, and W. G. Thies, Z. Phys. B **47**, 99 (1982).
[17] S. L. Segel, J. A. Walter, and G. J. Troup, phys. stat. sol. **31**, K43 (1969).
[18] S. L. Mair and Z. Barnea, Acta Cryst. **A31**, 201 (1975).
[19] J. Kortus, W. Cordts, M. Dietrich, S. Unterricker, A. Burchard, M. Deicher, and R. Magerle, Annu. Rep. 1996, University of Konstanz, Nukleare Festkörperphysik (p. 56).

Appendix E

Kortus J., Irmer G., Monecke J. and Pederson M.R.

Influence of cage structures on the vibrational modes and Raman activity of methane

Modelling Simul. Mater. Sci. Eng. **8**, 403-411 (2000)

Modelling Simul. Mater. Sci. Eng. **8** (2000) 403–411. Printed in the UK PII: S0965-0393(00)12934-1

Influence of cage structures on the vibrational modes and Raman activity of methane

J Kortus†§, G Irmer†, J Monecke† and Mark R Pederson‡

† Institute of Theoretical Physics, Freiberg University of Mining and Technology, B.-v.-Cotta-Strasse 4, 09596 Freiberg, Germany

‡ Center for Computational Materials Science—6392, Naval Research Laboratory, Washington DC 20375-5000, USA

Received 24 January 2000, in final form 20 March 2000

Abstract. Melanophlogite is a naturally occurring SiO_2-based clathrate structure which has the same structure of type I gas hydrates. Two types of voids are found in melanophlogite. Furthermore, as in the case of the gas hydrates, melanophlogite traps gas molecules within the voids. In this work we present a joint theoretical and experimental investigation of the CH_4 Raman spectra associated with the enclathrated CH_4 molecules. We find that the Raman intensities of the totally symmetric hydrogen stretch modes are significantly perturbed by the presence of the clathrate cage and show that the calculated Raman spectra may be used to determine the concentration and location of the enclathrated gas molecules. Relative to the gas-phase structure we identify two effects which are responsible for the change in intensity of the enclathrated molecules relative to the gas phase. The polarizibility of the surrounding cage acts to increase the Raman spectra of the stretch mode in the pentagondodecahedra cage. However, in the lower-symmetry tetrakaidecahedra cage, mixing between the hydrogen stretch mode and other optically silent molecular vibrations counteracts this effect and accounts for the different Raman intensities observed for the two types of voids. We suggest that similar calculations and experiments on the gas hydrates may provide an *in situ* diagnostic tool for determining the amount of natural gas contained within the gas hydrates on the sea floor.

(Some figures in this article are in colour only in the electronic version; see `www.iop.org`)

1. Introduction

Structures containing large voids of free space have been the subject of great scientific interest due to their large-scale application in the chemical industry and the possibility for studying basic interactions between the host structure and the guests which fill the voids. Examples of these cage structures are fullerenes [1, 2], clathrate structures such as gas hydrates [3] or zeolites.

Zeolites are of interest because they serve as shape and size selective catalysts and molecular sieves. However, the possibility of using these materials as hosts for the synthesis of small clusters has only recently been explored [4, 5]. Similar to the well known semiconductor superlattices, zeolite frameworks provide a method for creating new three-dimensional periodic arrays of guest molecules enclosed in the zeolite voids.

The experimental effort in this area, driven partially by potential applications to nonlinear optical devices and solar elements has resulted in several zeolite-based materials, which include

§ Present address: Center for Computational Materials Science—6392, Naval Research Laboratory, Washington DC 20375-5000, USA.

0965-0393/00/030403+09$30.00

small semiconductor clusters. Some specific examples are CdS [6], GaP [7] and Se [8] clusters. More information about other systems can be found elsewhere in review articles [4, 5] and references therein. In addition to experimental efforts there have also been theoretical studies, which have investigated the structural and electronic properties of zeolites [9, 10] or the simulation of small silicon clusters in sodalite [11]. Some of the most interesting questions about these systems pertain to the guest–guest and guest–host interactions. The guest–host interaction seems to be dominant, because in typical zeolites guests are separated by more than ten angstroms. The experimentally observed blue shift of the optical absorption threshold [8] compared with free clusters suggest similar quantum confinement effects that occur in layered semiconductor superlattices, due to changes of electronic states in the system by guest–host interactions.

The present paper will discuss a similar clathrate structure known as melanophlogite. Melanophlogite is a naturally occurring, low-density form of silica, which is always found to contain some organic matter. The SiO_4 tetraeders of the host form a three-dimensional framework consisting of two different kinds of cages. One of these cages is the naturally occurring silica equivalent of a C_{20} fullerene. In fact, melanophlogite was the first known example of a silicate framework structure with the pentagonal dodecahedron as a framework element [12].

The main goal of the present work is to investigate the interesting guest–host interactions of the host framework and the methane included in this material. Raman spectroscopy provides a non-destructive method for obtaining information about the kind of guests by observing their vibrational fingerprints. Furthermore, if the the Raman activity of the guest molecules is known, the density of the guests may be determined. Since, density-functional calculations provide a cost-effective *ab initio* means for determining the Raman activity of molecules the two methods combined give us a powerful tool for analysing and characterizing the above-mentioned structures.

From a technological standpoint, the secondary goal of this work is to demonstrate, by way of example, that techniques similar to those used here may be helpful for obtaining information about the concentration and type of natural gas contained within the gas hydrates. One of the clathrate structures of the gas hydrates is, in fact, identical to the structure of melanophlogite. The work discussed in the following shows that *in situ* Raman measurements of gas hydrates in conjunction with theoretically determined Raman spectra could be used to determine the location, type and concentration of such molecules

In the following sections we provide more information about this not so well known material and give experimental and theoretical details. In section 3 we discuss the experimental and theoretical details. In section 4 we present and discuss our results and conclusions are given in the last section.

2. Melanophlogite

Melanophlogite is a white and colourless mineral, which is found only at a few localities (Sicily [13], Fortullino [14], Chvaletice [15], Mount Hamilton [16] and Tsekur-Koyash [17]). Although melanophlogite is quite rare in nature it has been synthesized at 443 K from an aqueous solution of silica acids under a high pressure of different gases [18].

This silica polymorph usually contains several guest molecules (e.g. CH_4, N_2 and CO_2) in varying amounts. Kamb [12] first suggested that this low-density cubic form† of silica, which may also incorporate long, straight-chain hydrocarbons, is isostructural to the cubic gas

† The reported tetragonal forms, with a doubled unit cell in one direction, will not be discussed here.

hydrates [3] of type I. The SiO_4 tetraeders form a three-dimensional framework by sharing corners. This framework contains two types of cages: two pentagondodecahedra (cage I) and six tetrakaidecahedra (cage II) per unit cell. Figure 1 displays a schematic diagram of the crystal structure of three by three unit cells parallel to the [100] direction. The highlighted part presents four cages of type I on the corners and two cages of type II in the middle. The structure of the smaller cage I shown in figure 2 is well known from recent interest in carbon fullerenes. It is the natural occurring silica equivalent of a C_{20} fullerene. However, due to the tetrahedral coordination preferred by Si atoms the cages share faces to satisfy the sp^3 bonding. The corners are occupied by silicon atoms, whereas the oxygen atoms are located on the middle of the edges. The free space within cage I can be approximately described by a sphere-like void with diameter $d \sim 5.7$ Å and a volume $V \sim 97$ Å^3.

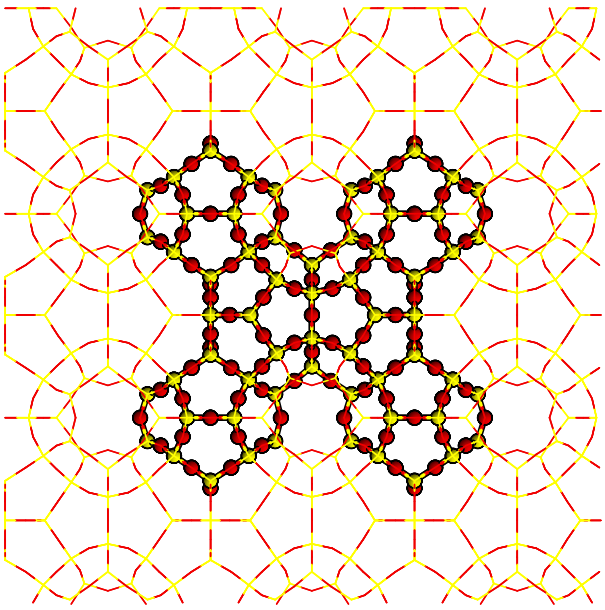

Figure 1. View of three by three unit cells of melanophlogite in the [100] direction. The corners of the emphasized section displays four cages of type I and two cages of type II in the middle. The lighter atoms are silicon atoms which are connected by oxygen atoms (dark circles). There are no guest molecules displayed.

The structure of cage type II is presented in figure 3. The top and bottom faces are hexagons and the remaining faces are pentagons. The free space within can be approximated by an ellipsoid with $d_1 \sim d_2 \sim 5.8$ Å, $d_3 \sim 7.7$ Å and a volume of 136 Å^3. An interesting feature of cage II is that the stacking of cages lead to nanotube-like structures, which may contain long chain-like molecules. The open circular objects seen in figure 1 represent a top view of the stacked cages of type II. The entire crystal structure may also be described as a three-dimensional array of stacked cages of type II.

3. Experimental and theoretical details

3.1. Raman measurements

Small crystallites of melanophlogite from Furtullino without visible fluid inclusions were carefully selected under an optical microscope from Olympus. The measurements were

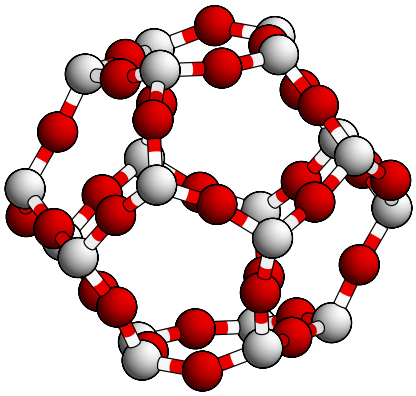

Figure 2. Cage I consists of 12 pentagonal faces. It is the natural occurring silica equivalent of a C_{20} fullerene. The atoms on the corners are silicon atoms (light circles), whereas the atoms between are oxygen atoms (dark circles). The guest molecule (methane) located inside this cage is not shown.

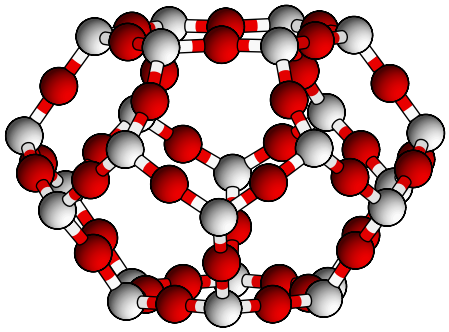

Figure 3. Cage II has a total of twleve pentagonal faces and two hexagonal faces (top and bottom). The atoms on the vertices are silicon atoms (light circles), which are connected to one another by bridging oxygen atoms (dark circles). The guest molecule (methane) located inside is not shown.

performed with the 514 nm line of an Ar^+ laser employing a triple-stage Jobin Yvon monochromator and a liquid nitrogen cooled CCD for detection. The scattered light was measured in subtractive mode. All experiments were carried out at room temperature with special care: using low power density of the laser in order to prevent the influence of illumination on the measurement results. The Raman spectra shown in figure 4 are typical of several obtained from different spots on the crystallite.

The spectral resolution in the C–H stretching vibration range was about 2 cm^{-1} due to the finite slit width of the spectrometer. Using this value in order to deconvolute the measured halfwidths the corrected halfwidths of the two observed CH_4 vibration bands are about 6 cm^{-1}.

3.2. Theoretical considerations

There are several current limitations which make it difficult to perform such calculations on periodic systems. First, the system is very large and contains a total of 143–178 atoms

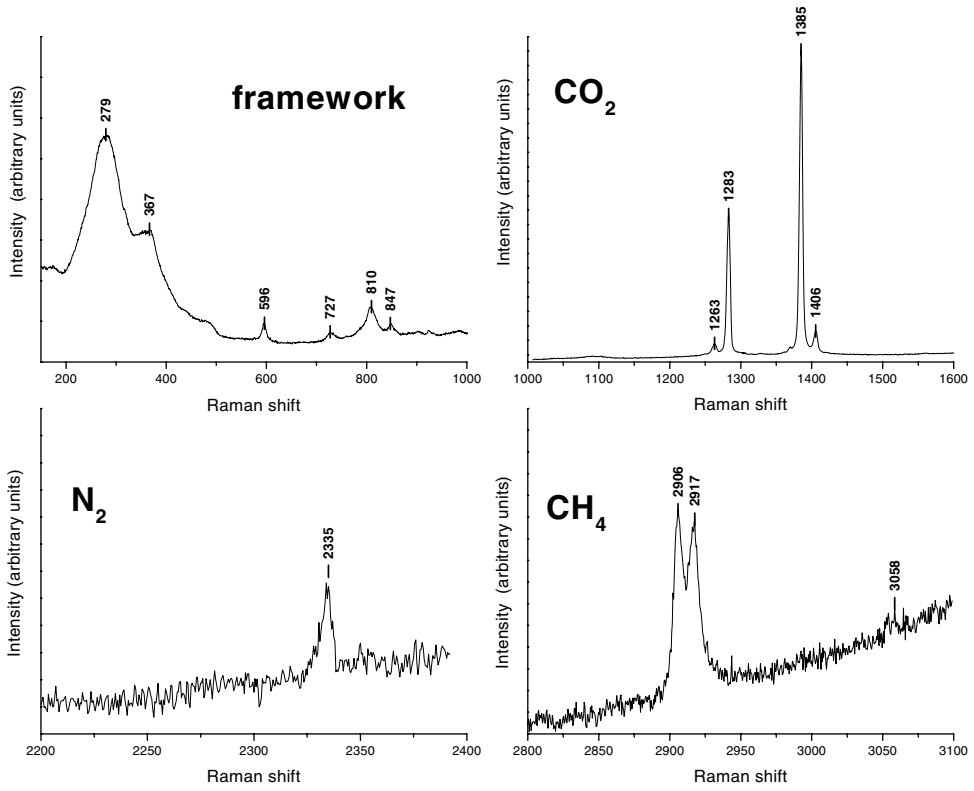

Figure 4. Raman spectra of melanophlogite: framework vibrations, CO_2 vibrations, N_2 vibrations and the totally symmetric breathing vibration of the guest molecule methane, CH_4.

depending on how many clathrate voids contain CH_4 molecules. Including the guest molecules in the void of the cages significantly lowers the symmetry of the unit cell. Second, the short C–H bond length would require extremely small muffin-tin spheres for a linearized augmented plane wave (LAPW) calculation which implies a very large value of $R * k\text{max}$. Even without this complication all-electron calculations on unit cells of this size are not currently an option.

Another frequently used numerical method for *ab initio* calculations of large unit and super cells would be a plane-wave expansion of the electronic wavefunctions, and non-local pseudopotentials to replace the effect of the core electrons. However, for the particular problem we are concerned with here, this approach is numerically very expensive for the following reason. The oxygen valence wavefunctions are strongly localized which results in a high plane-wave cutoff energy (typically about 60–70 Ryd). Together with the large volume of the complete unit cell, this makes plane-wave calculations too expensive.

There is also a more fundamental reason for using cluster-based models for this study. To date, the Raman spectra of periodic systems has only been studied for very simple periodic systems. This is primarily due to the problem of dealing with a uniform or extremely long-period electric field in another extremely short-period system. The calculation of Raman spectra for periodic systems remains an active area of research.

The calculation of the vibrational spectra of the whole unit cell together with different guest molecules by first-principle *ab initio* methods is currently still beyond present computing

possibilities. Therefore, in order to calculate the Raman frequencies and intensities of interest, we used some approximations based on experimental observations. The basic assumption is that no mixing of the vibrational modes of the framework and of guest molecules occur. This assumption is supported by experiment, because the framework vibrations are more than 2000 cm^{-1} lower than the investigated totally symmetric $1A_1$ mode of methane. Further possible changes of the molecule geometry due to charge transfer between guests and framework is neglected, although we allow for full relaxation of all electronic degrees of freedom and we account for breathing of the methane molecule. Using these assumptions the influence of the different cages can be considered as a small perturbation of a nearly free vibrating molecule.

Based on x-ray data [12] we generated the unit cell of melanophlogite and removed the two different cage types. The dangling bonds were then resaturated with hydrogen atoms. Holding the cage atoms fixed we allowed the methane to vibrate. This does not introduce a large error because, as already mentioned, the framework vibrations are slow compared to the totally symmetric $1A_1$ mode of methane.

The orientation of methane inside the cage has not been experimentally determined. Due to the space available there is no *a priori* reason for excluding the possibility that the methane can rotate within the cage at room temperature. For our calculations we restricted ourselves to an orientation of the methane molecule, which was adapted to the symmetry of cage I. There is no orientation of the T_d methane molecule which is compatible with the symmetry of cage II, therefore we have choosen the same orientation as for cage I. That means that all methane molecules would have the same orientation in the entire crystal framework of melanophlogite. This special choice certainly is not satisfactionary and could be avoided by using, for example, molecular dynamic techniques including the relaxation of the entire unit cell together with the included guest molecules. To address this point we carried out some preliminary tight-binding calculations allowing for full relaxation of the unit cell and the included methane. The initial placement of methane is not a special case for which the forces acting on the molecule vanish by symmetry. With the initial placement of methane described above we did not observe a rotation of methane during these simulations. The results of these tight-binding calculations will not be discussed here, although they agree well with the *ab initio* results. The use of the computationally more demanding *ab initio* methods was required, because the tight-binding method did not allow for the calculation of Raman intensities.

To determine the changes in the Raman frequencies and intensities, we displaced the hydrogen atoms of methane by a small distance (0.05 au) according to the positive and negative direction of the normal vibration of the methane A_1 mode and calculated the total energy and the forces of the corresponding geometry for both cages. Using the information of the forces acting on the relaxed free methane placed in both cages allowed for the calculation of the new equilibrium geometry of methane in the cages. In order to calculate the Raman intensities we applied an external electric field of 0.005 au to our cage structures with the methane as an included guest. The total energy for the frequency calculations was converged to 10^{-6} Hartree and for intensities to 10^{-8} Hartree.

The calculations were performed using the all-electron, full potential Gaussian-orbital cluster code NRLMOL [19]. The potential is calculated analytically on a variational integration mesh which allows for the determination of the electronic structure, total energies and Pulay-corrected Hellmann–Feynman forces with any desired numerical precision. We used the Perdew–Zunger parameterization of the standard Ceperly–Alder [20] functional within local density approximation (LDA). A more detailed description of the technique used and of computational problems associated with calculation of Raman scattering activities within density functional theory can be found elsewhere [21].

4. Results and discussion

4.1. Raman measurements

Figure 4 presents the results of Raman measurements of melanophlogite. The vibrational spectra shown in figure 4(*a*) was identified as the framework vibrations of melanophlogite. The higher peaks at 727, 810 and 847 cm^{-1} are not due to melanophlogite but probably due to dolomite, which was present in the investigated samples. This observation was supported by an absence of these peaks in samples from a different origin. Figures 4(*b*) and 4(*c*) are associated with the vibrations of CO_2 and N_2, respectively. Due to the larger halfwidths of these peaks than that of free molecules in air, we concluded that these molecules are an integral part of melanophlogite. The most interesting results used for further discussion of the Raman measurements are displayed in figure (*d*). The peak found at 2917 cm^{-1} is located at the same position as the totally symmetric A_1 mode of methane. Further support that the observed vibration is connected with methane comes from the higher peak found at about 3058 cm^{-1}, which is assigned to be asymmetric stretching T_2 mode of methane. The lower peak at 2906 cm^{-1} ($\Delta = 11$ cm^{-1}) is somewhat unexpected, since the total symmetric mode of methane is non-degenerate.

4.2. Theoretical calculation

As described above, we calculated the frequencies and Raman activities of the modes of methane in both cages. Due to the symmetry compatible orientation of methane in cage I the force constant matrix is diagonal for the investigated totally symmetric mode of methane. This further supports our chosen orientation, because within our numerical accuracy we found no torque components acting to rotate the methane molecule. The case of methane in cage II is more complicated, because the normal vibration of the totally symmetric mode of free methane is broken in cage II. Therefore our force constant matrix is no longer diagonal, which results in a mixing of other modes with the totally symmetric A_1 mode. After diagonalization of the force constant matrix we found a mixing of the totally symmetric mode with the threefold degenerate T_2 mode above 3000 cm^{-1}. This mode splits in a single vibrational mode and a twofold degenerated mode separated by 9 cm^{-1}. Eventually this could be found in experiment as a broad structure, because the unsplit threefold degenerate mode of the methane in cage I is found between the split modes of cage II. However, the current available experimental data do not allow for reliable investigation of this effect.

The results including only harmonic effects compared with the calculation of the free methane molecule using the same numerical approximations are summarized in table 1. Compared with the experimental results all calculated frequencies are slightly too high, which is a well known behaviour of LDA calculations. Using the free methane vibrations as a reference the A_1 mode in both cages is shifted downwards, but by different amounts. The perturbation of methane in the smaller cage I is larger, which results in the observed splitting of the totally symmetric mode of methane. The calculated splitting of only 3 cm^{-1} is too small compared with the experimentally measured value of 11 cm^{-1}. The previously mentioned tight-binding calculations of an entire unit cell of melanophlogite resulted in a splitting of 4.5 cm^{-1}.

In order to improve the theoretical results we included anharmonic effects in our calculations. Using all available energies and forces we fitted the data to a third-order polynomial of the total energy as a function of the displacement of the totally symmetric mode. Because we are still confined to the subspace of only one normal mode this problem reduces to a one-dimensional quantum mechanical problem of a particle in the resulting potential, which we solved numerically. This gives an additional splitting of 2 cm^{-1} due to anharmonic

Table 1. Raman frequency ω and activity R of the totally symmetric mode of methane in cages I and II compared with free methane including only harmonic effects.

	ω (cm^{-1})	R (Å^4 amu^{-1})
Free CH_4	2934	248
Cage I	2928	480
Cage II	2931	153

effects, which is additive to the harmonic splitting. Repeating the same calculations with a fourth-order polynomial lead to the same splitting as previously obtained. Therefore, our calculations give a totally splitting of the total symmetric mode of methane in melanophogite of 5 cm^{-1}. The agreement with experiment is still not perfect, and we attribute this to the approximate configuration of the CH_4 and the crystallographic data used for the generation of the cages. However, we believe that the qualitative description of this system is satisfactionary. The basic interaction between the cage and methane leads to a weakening of the bonding of the hydrogens to the carbons, which results in the downward shift of frequencies caused by an elongation of the carbon–hydrogen bond. This is an effect that is well known since zeolites are used for the cracking of long-chained hydrocarbons.

In addition to the calculations of vibrational frequencies the NRLMOL code allows for the calculation of Raman activities. The results presented in table 1 are, at first sight, confusing. Compared with the free molecule, the Raman activity of methane in cage I is enhanced, but decreased in cage II. This behaviour can be understood by the observed mixing of the totally symmetric A_1 mode and the T_2 mode above 3000 cm^{-1}, which caused by the cage II induced broken symmetry. Due to this mixing the Raman activity of the totally symmetric A_1 mode is decreased and increased for the T_2 mode above 3000 cm^{-1}. In the case of cage I this mixing does not occur, because cage I and methane share a common set of symmetry operations, so that the symmetry of cage I is compatible with that of methane for the totally symmetric vibrational mode.

As the final result we obtained a ratio of Raman activities of 3:1 for cage I and II. Bearing in mind that a unit cell of melanophlogite has a cage I:cage II ratio of 1:3, the observed, nearly equal, Raman intensities of both peaks are in good agreement with our calculations, assuming that the probability of methane as a guest molecule in both cage types is the same.

5. Conclusions

We have presented experimental and theoretical results for a vibration of a guest molecule in different cage structures. The applied methods are not confined to the discussed sample, but should be useful tools for investigations of a broader class of materials such as zeolites or other clathrates with guest molecules. The limiting condition for application should always be a careful check of the framework and guest interactions.

The calculations performed here qualitatively explain the splitting of the CH_4 symmetric vibrational A_1 mode that has been experimentally measured. Furthermore, the comparison between the calculated Raman-intensity ratios and the experimentally observed ratios suggests that, for this sample, the methane molecules occupy the two different types of cages with equal probability.

If such materials could be used to engineer arrays of weakly interacting encapsulated molecules or clusters, it would be useful to use Raman spectroscopy to determine the density of encapsulants and the relative probabilities of finding a given encapsulant in the different cages.

We have shown that the Raman intensities of the encapsulated molecule differ significantly from that of the gas-phase molecule and exhibit a sensitive dependence on the cage structure. This means that a quantitative determination of the relative populations cannot be achieved by borrowing gas-phase intensities. However, density-functional calculations provide a cost-effective means for determining how the encapsulant Raman intensities depend on the cage and could provide a mean for characterizing future samples.

Indeed melanophlogite samples from another location lead to experimentally observed ratios that are different from those discussed here. It would be interesting if an alternative experimental means could be used to confirm that the two samples do indeed have different ratios of cage I:cage II methane densities.

We hope this work will encourage some research on melanophlogite as an interesting material for basic studies of guest–host interactions and, possibly, as a means for developing arrays of weakly interacting particles.

Acknowledgments

We gratefully acknowledge S Köhler for making available and preparing the investigated melanophlogite samples. One of us (JK) would like to thank the Deutsche Forschungsgemeinschaft and the Michael-Jürgen-Leisler-Kiep Stiftung for financial support. MRP was supported, in part, by the ONR Molecular Design Institute N0001498WX20709.

References

[1] Kroto H W, Heath J R, O'Brien S C and Smalley R E 1985 *Nature* **318** 162
[2] Kratschmar W, Lamb L D, Fostiropoulos K and Huffman D R 1990 *Nature* **347** 254
[3] von Stackelberg M and Müller H R 1954 *Z. Elektrochem.* **58** 25
[4] Stucky G D and MacDougall J E 1990 *Science* **247** 669
[5] Ozin G A, Kuperman A and Stein A 1989 *Angew. Chem.* **28** 359
[6] Wang Y and Herron N 1988 *J. Phys. Chem.* **92** 4988
[7] MacDougall J E, Eckert H, Stucky G D, Herron N, Wang Y, Moller K, Bein T and Cox D 1989 *J. Am. Chem. Soc.* **111** 8006
[8] Bogomolov V N, Kholodkevich S V, Romanov S G and Agroskin L S 1981 *Solid State Commun.* **47** 181
[9] Ursenbach C U, Madden P A, Stich I and Payne M C 1995 *J. Phys. Chem.* **99** 6697
[10] Sun Q, Ye L and Xie X 1998 *Phys. Status Solidi* b **207** 357
[11] Demkov A A and Sankey O F 1997 *Phys. Rev.* B **56** 10 497
[12] Kamb B 1965 *Science* **148** 232
[13] von Lasaulx A 1876 *N. Jb. Mineral.* 250
Skinner B J and Appleman D E 1963 *Am. Mineral.* **48** 854
[14] Grasselini Troysi M and Orlandi P 1972 *Atti Soc. Tosc. Sci. Nat., Mem., Serie* A **79** 245
[15] Žák L 1967 *Am. Mineral.* **57** 779
[16] Cooper J F Jr and Dunning G E 1972 *Am. Mineral.* **57** 1494
[17] Kropatsheva S K and Markov J J 1975 *Dokl. Akad. Nauk* **224** 905
[18] Giess H, Gerke H and Liebau F 1982 *N. Jb. Mineral. Mh.* **3** 119
[19] Jackson K A and Pederson M R 1990 *Phys. Rev.* B **42** 3276
Pederson M R and Jackson K A 1991 *Phys. Rev.* B **43** 7312
Pederson M R and Jackson K A 1991 *Density Functional Methods in Chemistry* ed J K Labanowski and J W Andzelm (Berlin: Springer)
[20] Perdew J P and Zunger A 1981 *Phys. Rev.* B **23** 5048
[21] Porezag D and Pederson M R 1996 *Phys. Rev.* B **54** 7830

Appendix F

Kortus J., Pederson M. R. and Richardson S. L.

Density functional based prediction of the electronic, structural and vibrational properties of the energetic molecule: Octanitrocubane

Chem. Phys. Lett. **322**, 224-230 (2000)

19 May 2000

ELSEVIER

Chemical Physics Letters 322 (2000) 224–230

CHEMICAL PHYSICS LETTERS

www.elsevier.nl/locate/cplett

Density functional-based prediction of the electronic, structural, and vibrational properties of the energetic molecule: octanitrocubane

Jens Kortus [a], Mark R. Pederson [a,*], Steven L. Richardson [b]

[a] *Center for Computational Materials Science, Code 6390, Naval Research Laboratory, Washington, DC 20375, USA*
[b] *Department of Electrical Engineering and Materials Science Research Center, Howard University, Washington, DC 20059, USA*

Received 23 February 2000; in final form 30 March 2000

Abstract

We have performed density functional calculations on the recently discovered energetic molecule, octanitrocubane $C_8(NO_2)_8$. We predict a strongly exothermic dissociation energy and calculate the ionization potentials, electron affinities and vibrational spectra. We predict that the isolated molecule exhibits a symmetry which is higher than that found in the solid. The vibrational density of states shows strong Raman activity at low frequencies and strong IR intensities at high frequencies. We identify a low-energy anharmonic mode which is consistent with the experimentally assumed free torsional rotations of the NO_2 groups about their respective C–N axes.

1. Introduction

High-energy molecules are important not only for their obvious technological applications as explosives and propellants, but also for their inherently interesting molecular properties. One such example is the well-known molecule cubane (C_8H_8), which was first synthesized by Eaton and Cole [1]. Cubane has been extensively studied [2,3] because of the enormous strain energy due to the distortion of its C–C–C bond angle to 90°.

It has been suggested that cubane can be made more energetic by replacing its H atoms with nitro (NO_2) groups [4,5]. In fact, Zhang et al. [6] have recently synthesized octanitrocubane (cf. Fig. 1) where all the hydrogen atoms have been replaced by nitro groups. Octanitrocubane has been speculated to be even more energetic than the N-nitro compound HMX, which is one of the most energetic substances known.

In this Letter, we present an ab initio calculation of the optimized geometry of octanitrocubane, its molecular orbital energies and vibrational spectra. We show that the molecule, while stable, allows for large torsional displacements of the nitro groups and would release large amounts of energy upon dissociation into molecular N_2 and CO_2. Because octanitrocubane is significantly more electronegative than cubane, there is the possibility of cation induced stabilization of the crystal through selective doping. The infrared and Raman spectra calculated here should be useful in determining the presence of

* Corresponding author. Fax: +1-202-404-7546; e-mail: pederson@dave.nrl.navy.mil

0009-2614/00/$ - see front matter
PII: S0009-2614(00)00425-5

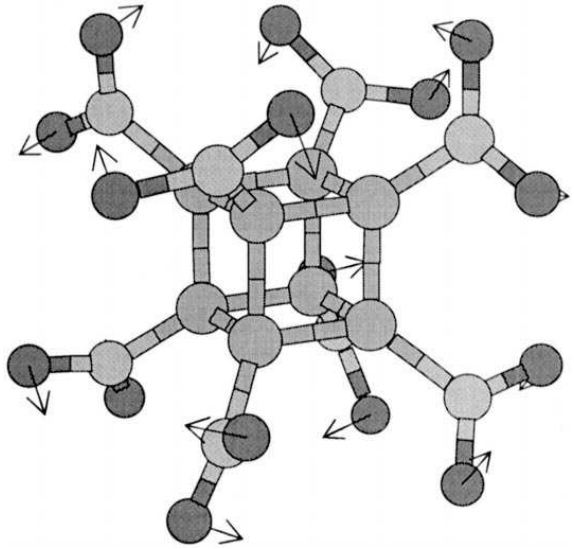

Fig. 1. Optimized molecular structure of octanitrocubane. The carbon atoms form a cube to which the nitro groups are connected at the corners. The dark balls are the oxygen atoms. The arrows point in the direction of the quartic concerted torsional mode that is discussed in this Letter.

octanitrocubane and in confirming the symmetry lowering which apparently occurs in the solid structure. Further, one of the very soft torsional modes exhibits strong anharmonicity and is fundamentally interesting.

2. Calculational details

Our density functional-based calculations [7,8] were performed with the all-electron Gaussian-orbital-based NRLMOL program [9,10], using the Perdew–Burke–Ernzerhof (PBE) generalized-gradient approximation for the exchange and correlation functional [11]. For each oxygen, nitrogen and carbon atom, we use nine s-type contracted functions, four p-type contracted Gaussians and 3 d-type contracted Gaussians. For carbon the contracted basis set is constructed from a total of 12 bare Gaussians, while for oxygen and nitrogen the contracted basis sets were constructed from a total of 13 bare Gaussians. The decay constants were optimized for density-functional applications and range between 2.22 $\times 10^4$ and 0.0772 for carbon, 5.18×10^4 and 0.0941 for nitrogen, and 6.12×10^4 and 0.1049 for oxygen. The contraction coefficients and decay constants are available electronically upon request and a discussion of the method used for determining these quantities appears in Ref. [12]. To determine the optimized geometries, we first solve the all-electron Schrödinger wave equation to find the self-consistent Kohn–Sham orbitals. Once these are obtained the Hellmann–Feynman–Pulay forces are determined and used in conjunction with the conjugate-gradient algorithm to optimize the molecular geometry [13–15]. This process is iterated until the forces on each atom are smaller than 0.01 eV/Å. Given the equilibrium geometry, we determine the vibrational frequencies, infrared spectrum and Raman spectra using the method discussed in Ref. [16]. Since we generally use symmetry to optimize our molecular geometries, the determination of the harmonic vibrational frequencies tells us if we are at a local minimum. If imaginary frequencies are found, the symmetry is reduced and we repeat the calculation until we are satisfied that we have found a symmetry that is locally stable.

A point of special interest to this molecule is the extremely soft concerted torsional vibrations associated with the NO_2 groups about the C–N bond axes. For these degrees of freedom it is necessary to go beyond a harmonic approximation to fully understand their dynamics. We will discuss this further when we come to the problem.

To place our calculated vibrational spectra of octanitrocubane in the proper context, we note that there have been several Hartree–Fock (HF) based and density functional-based calculations on the vibrational spectra of cubane [17–20]. Here we briefly compare the structural properties and IR spectra of cubane, as calculated with NRLMOL and the PBE density functional, to the DFT-based results of Miaskiewicz and Smith [20].

The PBE density functional should perform similarly as the BLYP density functional, which also is a gradient corrected density functional, but does not include a HF part as in the case of the hybrid B3LYP.

The C–C bond length of 1.5714 Å obtained from our geometry optimization of cubane with O_h symmetry falls between the BLYP (1.5833 Å) and B3LYP (1.5701 Å) results, and compares favorably with the experimental C–C bond lengths of 1.5708–

Table 1
Calculated frequencies and IR intensities of the three IR active modes of cubane. All frequencies given are unscaled. The results from this work are given under PBE.

IR frequency (cm^{-1})			IR intensity (km/mol)		
Exp.	BLYP	PBE	BLYP	B3LYP	PBE
852	839	849	4.7	6.1	9.3
1235	1239	1223	1.1	1.9	5.9
2990	3034	3033	165	140	137.5

The experimental values are given in Ref. [24]. The BLYP and B3LYP results are from Ref. [20].

1.571 Å obtained from microwave spectroscopy [21] and electron diffraction experiments [22] respectively. The C–H bond length of 1.0954 Å agrees also well with BLYP (1.0995 Å), B3LYP (1.0914 Å) and the experimental values of 1.098 Å [22] or 1.097 Å [21]. Miaskiewicz and Smith [20] have also calculated IR intensities for cubane. In Table 1 we compare our results for the frequencies and IR intensities for the three IR active modes with the previous DFT calculations on cubane.

The agreement among the various DFT and experimentally determined IR spectra is similar to what would be expected from previous DFT results [23]. Especially for the purpose of predicting experimental IR signatures of the cubane molecule the agreement among the PBE, BLYP and B3LYP is quite satisfactory. The qualitative strengths of the three modes show the same orderings for all three calculations. For a detailed discussion of basis-set and exchange-correlation dependencies in experimentally well understood molecules the reader is referred to Ref. [16]. Based on their calculations, Cole et al. [24] propose a semi-quantitative description of the IR bands at 852 and 1235 cm^{-1} as strong, and describe the IR mode at 2990 cm^{-1} as very strong. This description is reproduced by all of the calculations. The overall good agreement among our PBE density-functional results, other DFT calculations, and experimental results for cubane gives one confidence that the method will provide similar accuracy for describing octanitrocubane.

3. Results and discussions

Pictured in Fig. 1 is the equilibrium structure of the octanitrocubane molecule. The structure has two inequivalent carbon atoms, two inequivalent nitrogen atoms and three inequivalent oxygen atoms. The overall symmetry of the molecule is determined by a group of order 8 that is generated from the symmetry operations $(X,Y,Z) \rightarrow (Y,X,Z)$, $(X,Y,Z) \rightarrow (-X,-Y,Z)$ and $(X,Y,Z) \rightarrow (-X,Y,-Z)$. With respect to 4 N_2 molecules and 8 CO_2 molecules we find that this molecule is bound by 798 kcal mol^{-1} which is in good agreement with the MINDO/3 calculations of Owens [25] of 761 kcal mol^{-1}. We find that this molecule has an electron affinity of 3.43 eV and an ionization energy of 10.54 eV.

To address the question of local stability of this molecule we have performed a vibrational analysis of this cluster using the methodology discussed in Refs. [16,26]. Interestingly, at the harmonic level we find a total of eighty-nine real frequencies and *seven* zero-frequency modes. While six of the zero-frequency modes correspond to the usual rotational and translational modes, the seventh zero-frequency harmonic mode requires a more in-depth discussion. We start by noting that the harmonic analysis shows that this mode is entirely associated with torsional rotations of pairs of oxygen atoms about their respective C–N bonds. For reasons that will become clear shortly, we refer to this mode as the quartic concerted torsional mode (QCTM) throughout the remainder of the discussion.

Pictured in Fig. 1 are arrows on each of the 16 oxygen atoms which designate the displacement of the QCTM. For the equilibrium geometry, the nitro groups on opposite corners of the cube arrange themselves in a staggered configuration and the QCTM mode acts to preserve this staggered structure. Therefore we expect steric interactions between opposing nitro groups to remain unchanged by a QCTM displacement. Since the primary interactions between

oxygen atoms are mediated by pair repulsions, it is worthwhile to determine how the second-order energy changes if only pair interactions between the oxygen atoms are assumed. For this case we find that the second-order energy change is exactly zero for any pair potential for the QCTM, shown in Fig. 1. Finally, we note that we have performed frozen vibron calculations for both the energy and the force as a function of the QCTM displacement and the resulting potential energy curve is shown in Fig. 2. A detailed analysis of both the energy and forces as a function of the QCTM displacement confirms that that the second derivative and all odd derivatives of this mode vanish identically.

In addition to the classical potential observed by the torsional mode, we have determined the anharmonic vibrational wavefunctions and energies associated with this mode and present the results in Fig. 2. Because of the quartic nature of the potentials, the anharmonic wavefunctions are flatter than what would be expected from a harmonic oscillator potential. The zero point energy associated with this mode is found to be 16.4 cm^{-1} and the first excited state is found to be 58.5 cm^{-1}, suggesting that the lowest observable excitation would be observed at 42 cm^{-1}. As discussed below, our calculations show that this state exhibits weak Raman coupling. Because this

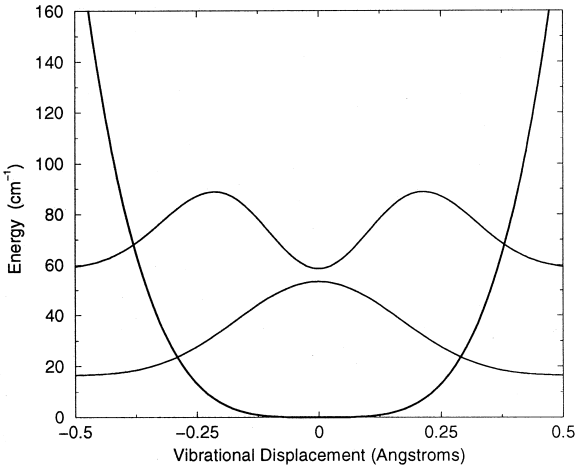

Fig. 2. Potential as a function of vibrational displacement observed by the QCTM. Also included are the squares of the lowest eigenmodes of this predominantly quartic potential. The energy intercepts of the eigenmodes are shifted by their respective energies which shows a zero point energy of 16 cm^{-1} and a lowest excitation energy of 42 cm^{-1}.

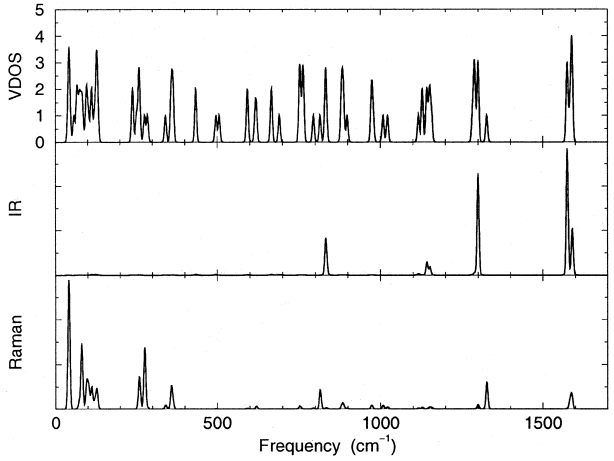

Fig. 3. The upper panel shows the calculated vibrational density of states (VDOS) of octanitrocubane. The middle and lower panels display the calculated IR and Raman spectra which are shown in arbitrary units.

mode is anharmonic, it might be detected by looking for second-harmonic generation in the Raman spectra which, according to our calculations, should occur at 102.1 cm^{-1}. Unfortunately, as discussed below, there are other strong Raman active modes which appear at both of these energies. The effective mass of this state is 15.99534 amu which again confirms that this state is associated entirely with the motion of oxygen atoms.

Since the potential associated with the QCTM is convex and since all other harmonic modes exhibit real frequencies, the symmetry of the molecule studied here corresponds to a locally stable geometry for the free molecule. To address the question of global stability we have performed calculations on two other reasonable symmetries of the molecule and have found that these symmetries lead to higher energies. In the solid phase, Zhang et al. [6] have determined the structure from X-ray measurements. The unit cell consists of four molecules which are related to one another by inversion and translations by $(\frac{1}{2},\frac{1}{2},0)$ lattice vectors. As an isolated molecule, each octanitrocubane molecule has a two-fold symmetry which means it has a lower symmetry than our equilibrium structure shown in Fig. 1. We have determined, that the experimental structure of the isolated molecule is higher in energy than our calculated structure. Furthermore, the molecule relaxes

without encountering a barrier to our equilibrium structure. This result strongly suggests that the geometry shown in Fig. 1 is the ground state geometry for the isolated molecule and that symmetry lowering in the crystal is due to intermolecular interactions.

We now discuss the harmonic modes that have spectroscopically interesting features. The calculated vibrational density of states is shown in the upper panel of Fig. 3. The middle and lower panels show a calculated overview of the IR spectra and Raman spectra. The IR and Raman spectra are given in arbitrary units.

3.1. Raman spectra

Because O, N and C have similar masses and form similar bonds the vibrational spectrum is generally associated with complicated coupled movements of all atoms in the molecule. However at very low energies (below 131 cm^{-1}) the vibrations are associated primarily with oxygen motion and in the 970–1157 cm^{-1} energy range the motion is associated primarily with carbon atoms. Also at very high energies (1283 cm^{-1} and higher) the carbon atoms are essentially stationary and the vibrational displacements are associated entirely with N and O motions. From the vibrational density of states we determine the zero point energy of the molecule to be 3.84 eV. At approximately 41 cm^{-1} there is a doubly degenerate Raman active mode that is associated primarily with torsional oxygen vibrations. Because this mode is two-fold degenerate and because it is nearly degenerate with the one-fold QCTM some interesting changes in the peak positions are expected to occur in this region as a function of temperature, symmetry lowering, and changes in charge state. At 258 cm^{-1} there is a two-fold state that leads to a reasonably strong Raman peak which is just below a very strong one-fold Raman active state at 276 cm^{-1}. These modes are primarily associated with C–N and C–C stretching. Since the molecular polarizability is roughly proportional to the volume, the strong Raman activity of these states is understood by noting that as the C–N and C–C stretches occur the size of the molecule and effective polarizability change during the vibration. Indeed, the Raman mode at 276 cm^{-1} is a breathing mode of octanitrocubane. At 815 cm^{-1} a one-fold mode leads to strong Raman activity. This Raman mode is associated with a collective breathing of the C and N atoms together with a O–N–O bending of the oxygens. At 1327 cm^{-1} there is another strong Raman peak, which is associated with breathing of the N atoms. In this case the C atoms are predominantly stationary and the oxygen atoms beat against the nitrogen atoms, as the nitrogen breaths outward. Finally, at 1583 and 1589 cm^{-1} there is strong Raman activity associated with two modes. In each case only 4 nitrogen atoms take part, with the N atoms wagging in the plane defined by the nearest neighbor carbon and oxygen atoms. The N atoms beat against the oxygen atoms and the carbons are fixed.

If one of the ^{14}N atoms is replaced by a ^{15}N atom the Raman active peaks shift only by a small amount (from 1 to 5 cm^{-1}), but replacing all nitrogens by their heavier isotope the modes at 815, 1327 and 1589 cm^{-1} shift by approximately 7.5, 19 and 36 cm^{-1}, respectively.

3.2. Infrared spectra

The IR spectrum shows four main peaks each of which is composed of a doubly degenerate mode and a singly degenerate mode. This is similar to the splitting of the threefold degenerate T_{1u} IR active modes in cubane.

At 832 cm^{-1} there is a doubly degenerate IR mode which is nearly degenerate with a one-fold at 835 cm^{-1}. These modes are primarily associated with a C–N stretching motion of the NO_2 groups and some bending of the oxygens. At 1143 and 1152 cm^{-1} there are IR active two-fold and one-fold vibrational states which correspond to C–C stretch modes and stationary nitro groups.

Because the NO_2 groups are not rigid spheres other very strong IR active modes also appear. At 1299 and 1300 cm^{-1} there are one-fold and two-fold very strong IR active modes, which correspond to a C–N stretch due to N atom motion, with the oxygen atoms beating against the N atoms. The highest frequency IR active mode is a two-fold degenerate state at 1576 cm^{-1} and a one-fold state at 1591 cm^{-1}. This mode is associated with a wagging mo-

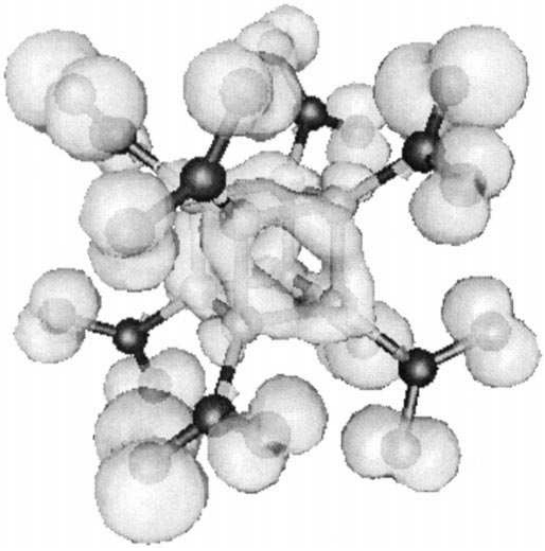

Fig. 4. Isodensity surface of the highest occupied molecular orbital (HOMO) for octanitrocubane. The energy of the HOMO level is −8.60 eV.

tion of the N atoms beating against the oxygen atoms and stationary C atoms.

3.3. Electronic structure

Pictured in Fig. 4 is the square of the wavefunction for the HOMO level. Both the HOMO and LUMO levels are two-fold degenerate, suggesting that small changes in charge state could lead to minor Jahn–Teller distortions followed by symmetry reduction that would be primarily mediated by movements of the oxygen atoms. From Fig. 4 it is also apparent that the HOMO level participates in C–C covalent bonding and that removal of an electron from this state could weaken the skeletal framework. Examination of the LUMO level (−5.35 eV) shows that the addition of an electron to the molecule introduces antibonding states which may also act to reduce the C–C covalent bonding. The electron affinity of octanitrocubane (3.43 eV) is very large compared to cubane (1.5 eV) and is even larger than that of the C_{60} molecule (2.74 eV GGA and experiment). In analogy to the fullerene in the alkali-doped fullerene crystals, the octanitrocubane molecule will act as an electron acceptor and Madelung induced stabilization of a solid phase of octanitrocubane could be accomplished by doping the solid phase with alkali atoms or other electron donors. However, the HOMO and LUMO levels show that such a stabilization would only be accomplished at the cost of destabilizing the octanitrocubane framework and this could lead an overly reactive solid.

Acknowledgements

J.K. and M.R.P. were supported in part by ONR Grant N0001498WX20709. S.L.R. acknowledges support from the US Navy–American Society for Engineering Education (ASEE) Faculty Sabbatical Leave and Summer Research Programs. We would like to thank Dr. Gilardi for critically reading the original manuscript.

References

[1] P.E. Eaton, T.W. Cole Jr., J. Am. Chem. Soc. 86 (1964) 3158.
[2] T. Yildirim, P.M. Gehring, D.A. Neuman, P.E. Eaton, T. Emrick, Phys. Rev. Lett. 78 (1997) 4938.
[3] S.L. Richardson, J.L. Martins, Phys. Rev. B 58 (1998) 15307.
[4] P.C. Hariharan, J.J. Kaufman, A.H. Lowrey, R.S. Miller, Int. J. Quantum Chem. 28 (1985) 39.
[5] D.A. Chapman, J.J. Kaufman, R.J. Buenker, Int. J. Quantum Chem. 1 (1991) 389.
[6] M.-X. Zhang, P.E. Eaton, R. Gilardi, Angew. Chem. Int. Ed. 39 (2000) 401.
[7] P. Hohenberg, W. Kohn, Phys. Rev. 136 (1964) B864.
[8] W. Kohn, L.J. Sham, Phys. Rev. 140 (1965) A1133.
[9] M.R. Pederson, K.A. Jackson, Phys. Rev. B 41 (1990) 7453.
[10] K.A. Jackson, M.R. Pederson, Phys. Rev. B 42 (1990) 3276.
[11] J.P. Perdew, K. Burke, M. Ernzerhof, Phys. Rev. Lett. 77 (1996) 3865.
[12] D. Porezag, M.R. Pederson, Phys. Rev. A 60 (1999) 2840.
[13] H. Hellmann, Einführung in die Quantentheorie, Deuticke, Leipzig 1937.
[14] R.P. Feynman, Phys. Rev. 56 (1939) 340.
[15] P. Pulay, Mol. Phys. 17 (1969) 197.
[16] D.V. Porezag, M.R. Pederson, Phys. Rev. B 54 (1996) 7830.
[17] J. Almlöf, T. Jonvik, Chem. Phys. Lett. 92 (1982) 267.
[18] C.P. Vlahacos, H.F. Hameka, J.O. Jensen, Chem. Phys. Lett. 259 (1996) 283.
[19] B.S. Jursic, J. Mol. Struct. 394 (1997) 15.
[20] K. Miaskiewicz, D.A. Smith, Chem. Phys. Lett. 270 (1997) 376.

[21] E. Hirota, Y. Endo, M. Fujitake, E.W. Della, P.E. Pigou, J.S. Chickos, J. Mol. Struct. 190 (1988) 235.
[22] L. Hedberg, K. Hedberg, P.E. Eaton, N. Nodari, A.G. Robiette, J. Am. Chem. Soc. 113 (1991) 1514.
[23] D.C. Patton, D.V. Porezag, M.R. Pederson, Phys. Rev. B 55 (1997) 7454.
[24] T.W. Cole, J. Perkins, S. Putnam, P.W. Pakes, H.L. Strauss, J. Phys. Chem. 85 (1981) 2185.
[25] F.J. Owens, J. Mol. Struct. 460 (1999) 137.
[26] A.A. Quong, M.R. Pederson, J.L. Feldman, Solid State Commun. 87 (1993) 535.

Appendix G

Kortus J., Richardson S. L. and Pederson M. R.

First-Principles DFT study of the structural, electronic and vibrational properties of azidopentazole

Chem. Phys. Lett. **340**, 565-570 (2001)

8 June 2001

ELSEVIER

Chemical Physics Letters 340 (2001) 565–570

CHEMICAL PHYSICS LETTERS

www.elsevier.nl/locate/cplett

First-principles DFT study of the structural, electronic and vibrational properties of azidopentazole

Jens Kortus [a,1], Mark R. Pederson [b,*], Steven L. Richardson [c]

[a] *Department of Physics, Georgetown University, Washington, DC 20057, USA*
[b] *Center for Computational Materials Science, Code 6390, Naval Research Laboratory, Washington, DC 20375, USA*
[c] *Department of Electrical Engineering and Materials Science Research Center, Howard University, Washington, DC 20059, USA*

Received 26 January 2001; in final form 5 April 2001

Abstract

In this Letter we report a density functional all-electron calculation of the structural and electronic properties of the polynitrogen high-energy molecule, azidopentazole (N_8). We have also performed a vibrational analysis to determine the IR and Raman spectra. Our calculated geometrical properties and vibrational frequencies are in good agreement with previous ab initio and density functional calculations. The weaker IR modes show a different relative ordering than previously reported. We also report calculated Raman intensities for azidopentazole.

1. Introduction

Azidopentazole (N_8) is a polynitrogen high-energy molecule whose structural geometry is characterized by a five-membered ring with a three-atom nitrogen tail (cf. Fig. 1). While this molecule has not yet been synthesized, there have been a number of theoretical calculations in the literature on the electronic and structural properties of azidopentazole. In particular, Glukhovtsev et al. [1] have performed high level ab initio molecular orbital and density functional theory (DFT) studies on a number of isomers of N_8 and have determined that azidopentazole with C_s symmetry is the most stable N_8 isomer. Nguyen and Ha [2] have reported ab initio molecular orbital theory calculations at the quadratic configuration interaction [QCISD(T)/6-31G(d)] and coupled-cluster [(CCSD(T)/DZP)] levels of theory and have also concluded that azidopentazole is the most stable of the N_8 isomers.

A number of workers including, Chung et al. [3], Gagliardi et al. [4,5], and Kortus et al. [6] have further argued that, although azidopentazole is much lower in energy than its cubic isomer N_8 [7,8] azidopentazole might not be very viable as a high-energy polynitrogen molecule because of its low decomposition barrier to molecular nitrogen.

Despite this possible limitation on its long-term stability, we still believe that azidopentazole is a possible candidate for a novel polynitrogen molecule, especially in light of the newly discovered N_5^+ cation by Christie et al. [9]. We report in this Letter a first-principles all-electron density functional

* Corresponding author. Fax: +1-202-404-7546.
E-mail addresses: pederson@dave.nrl.navy.mil (M.R. Pederson), slr@imhotep.ccmpf.howard.edu (S.L. Richardson).
[1] Present address: MPI für Festkörperforschung, Postfach 800665, D-70506 Stuttgart, Germany.

0009-2614/01/$ - see front matter
PII: S0009-2614(01)00414-6

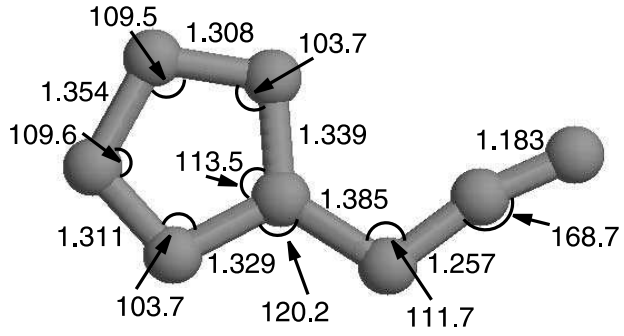

Fig. 1. Optimized geometry of the ground state of azidopentazole which has C_s symmetry with the PBE gradient-corrected density functional. The bond lengths are given in Å and the angles in degrees.

theory study of the electronic, structural, and vibrational properties of azidopentazole, in its ground state. While a structural optimization and vibrational analysis of azidopentazole have been previously reported in the literature [1–5], only calculated IR intensities have been reported [1].

Our results described here include both a detailed analysis of the calculated IR spectra as well as a discussion of the predicted Raman spectra and their intensities. We hope that this new information on the vibrational properties of azidopentazole will assist future experimental work in characterizing this elusive high-energy polynitrogen species.

2. Computational details

The theoretical studies described in this Letter were carried out using a linear combination of atomic orbitals-molecular orbital (LCAO) approach within the density functional framework [10,11]. The molecular orbitals were expanded as linear combinations of Gaussian functions centered on the atomic sites. The calculations were performed at the all-electron level and the multicenter integrals required in the solution of the Kohn–Sham equation were calculated by integrating numerically over a mesh of points [12].

Our density functional-based calculations were performed with the all-electron Gaussian-orbital Naval Research Laboratory Molecular Orbital Library (NRLMOL) program [12–16], using the Perdew–Burke–Ernzerhof (PBE) [17] generalized-gradient approximation for the exchange and correlation function. The PBE density functional used in our work is a gradient corrected exchange-correlation functional which is similar to the BLYP density functional often used in many quantum chemical studies.

For nitrogen, 13 optimized decay parameters ranging from 51750.624 to 0.09411174 are used [15]. We used eight s-type, four p-type, and three d-type Gaussian orbitals per N atom, thus giving a total of 280 basis functions which were used for our geometry optimizations. The contraction coefficients for the 1s, 2s, 2p atomic orbitals were obtained by performing an SCF-LDA calculation on the spherical unpolarized nitrogen atom whose total atomic energy was converged to within 10 meV [15].

The molecule azidopentazole was optimized using the Hellmann–Feynman–Pulay forces [18–20] in conjunction with the conjugate-gradient algorithm. A final optimization was obtained when the total forces were less than 0.001 hartree/bohr.

The vibrational frequencies are calculated by direct diagonalization of the dynamical matrix. This matrix is constructed by taking finite differences of both positive and negative displacements (0.05 a.u.) of the coordinates of each atom near the equilibrium geometry and calculating the forces for each corresponding geometry. The infrared and Raman intensities discussed here were obtained from derivatives with respect to the atomic coordinates of the dipole moment and the polarizability tensor. Based on the definitions of the dipole moment and the polarizability tensor, the derivatives of these properties can be expressed as a direct response to an external electric field. A more detailed discussion of the methods used here can be found in [14,21]. For our study the energies and wave functions must be well converged, as the Raman activity involves a third derivative of the total energy. This required the use of a total of 9 s-type, $4(\times 3)$ p-type, and $4(\times 5)$ d-type functions on each atom leading to a total of 328 basis functions. The additional polarization functions are particularly important. Tests on smaller systems containing similar atoms suggest that our reported Raman activities should be within 5–10%

of the results obtained effectively using only single Gaussians. [14] The use of many single Gaussians on all atoms allows one to at least partially mimic the effect of excluded basis functions with higher angular momentum.

3. Results and discussion

3.1. Geometry optimization

We have summarized in Fig. 1 the results of the geometry optimization within our gradient-corrected PBE density-functional calculations. Our calculated bond lengths and bond angles are within 0.1 Å and 1°, respectively, of the B3LYP/6-31G* results of Glukhovtsev et al. This excellent agreement can be seen as a further test of the accuracy of the PBE functional used in our work in comparison to the more commonly used functionals in quantum chemistry.

3.2. Electronic structure

In view of possible applications for high-energy materials total energy calculations contain useful information. Table 1 compares the total energy of azidopentazole to the single bonded O_h-symmetric N_8-cubane octaazacubane and the D_{2h}–symmetric octaazapentalene. Further, we report in Table 1 the zero point corrected total energies (E_0) obtained from the vibrational frequencies in the harmonic approximation.

The single-bonded octaazacubane, an isoelectronic analogue of the highly strained hydrocarbon cubane (C_8H_8) [23], is very high in energy. In fact the sum of the total energies of the free ions N_3^- and N_5^+, which both have been experimentally observed [9] and could be used as precursors for synthesis, is lower than that of octaazacubane, which makes a synthesis from these ions unlikely.

Octaazapentalene, consisting of two five-membered rings fused together (see Fig. 2), was found to be the lowest energy structure in a study of ten N_8 isomers by Gagliardi et al. [22]; however, azidopentazole was not included in this study. In agreement with other theoretical predictions [1,2] we find that azidopentazole is lower in energy than octaazapentalene. Both of these isomers are significantly lower in energy than the sum of the free ions, which could raise hope for a possible synthesis.

Another interesting energy scale is the energy for decomposition to molecular nitrogen, because all of these isomers will most likely decompose into the much more stable molecular nitrogen. In accord with previous work [1] we find that the relative energy (zero point corrected) for decomposition of azidopentazole to four N_2 molecules is 172 kcal/mol for the PBE density functional.

Fig. 3 shows the square of the wave function for the highest occupied molecular orbital (HOMO) of azidopentazole which has an energy of −7.6 eV. It is apparent that the HOMO participates in the covalent N–N bonding, therefore removing an electron from this level will weaken the bonding. The vertical ionization potential is 10.9 eV. Similarly, Fig. 4 shows the square of the wave function for the lowest unoccupied molecular orbital (LUMO) for azidopentazole which has an energy of −4.136 eV. As expected, electrons will be accepted in the acidic tail of the molecule. The calculated electron affinity of only 0.63 eV is rather small. This makes possible doping with alkali atoms, in analogy to the alkali-doped fullerene crystals, difficult and a stabilization of a solid

Table 1
Total ground state energies E and zero point corrected energies E_0 in atomic units (a.u.) for several N_8 isomers calculated in these work

	E	E_0	$E_0^{rel}(4N_2)$
N_3^-	−164.14485	−164.13586	
N_5^+	−273.13727	−273.11756	
Octaazacubane (O_h)	−437.21014	−437.17813	393.2
Octaazapentalene (D_{2h})	−437.54780	−437.51182	183.8
Azidopentazole (C_s)	−437.56550	−437.53077	171.9

E_0^{rel} is the zero point energy corrected relative energy to $4N_2$ molecules in kcal/mol.

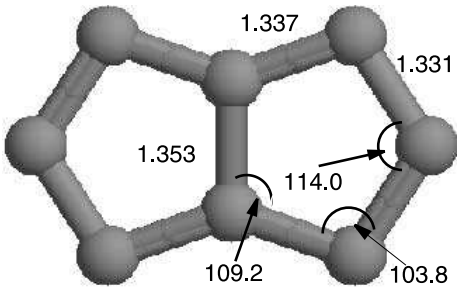

Fig. 2. Optimized geometry of the ground state of octaazapentalene which has D_{2h} symmetry.

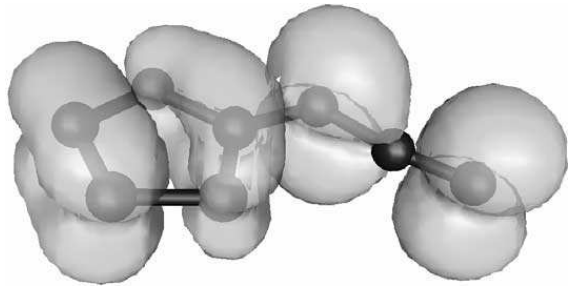

Fig. 3. Isodensity surface of the highest occupied molecular level of azidopentazole. The energy of this level is −7.6 eV.

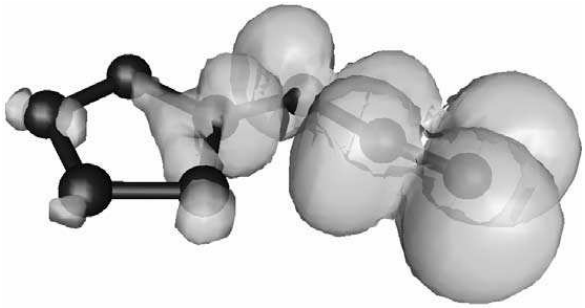

Fig. 4. Isodensity surface of the lowest unoccupied molecular level of azidopentazole. The energy of this vacant level is −4.136 eV.

phase of azidopentazole by Madelung effects would be unlikely. Further occupation of the LUMO would weaken the bond between the pentagon and the tail. This bond is already the longest in the molecule so LUMO occupation would increase the propensity toward decomposition.

3.3. Vibrational spectra

In order to aid experiment in identification and characterization of the predicted structure we have calculated Raman and IR spectra which are displayed in Fig. 5. Due to the lowering of symmetry compared to N_5^+ with C_{2v} symmetry the spectra show distinctive changes, which should allow for a clear identification. Table 2 reports the calculated absolute infrared intensity and Raman activity. The strongest IR active mode at 2164 cm^{-1} is a vibrational mode associated mainly with movement of the two outermost nitrogens on the tail. The nitrogens in the pentagon do not take part in the vibration. The lowest frequency mode at 54 cm^{-1} is a complicated torsional vibration of the tail against the pentagon. No bonds are significantly stretched during this vibration, which might help to prevent the decomposition of the molecule into molecular nitrogen. The strong Raman mode at 151 cm^{-1} is a wagging mode of the three-atomic tail against the pentagon in the plane of the molecule. Another strong mode at 921 cm^{-1} is almost entirely due to distortions of the nitrogens within the pentagon. The two top nitrogens in Fig. 1 beat against the other nitrogens in the pentagon, seriously straining and stretching the nitrogen bonds in the pentagon. The two high frequency modes at 1311 and 1345 cm^{-1} are breathing modes which mainly involve only the pentagonal

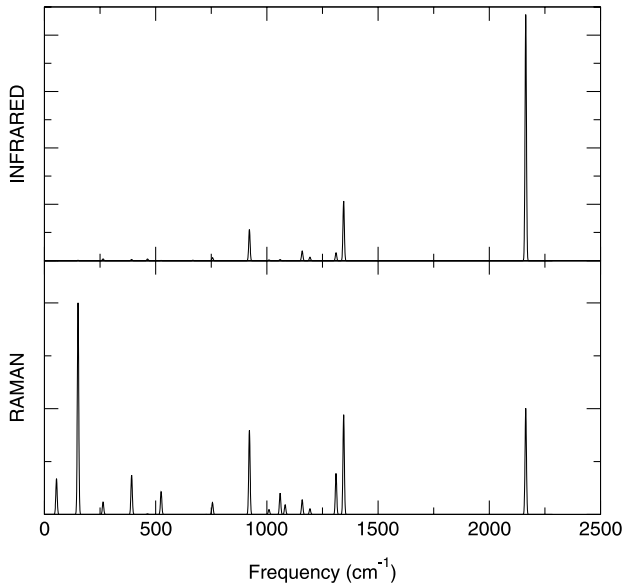

Fig. 5. Calculated infrared and Raman spectra of azidopentazole The IR and Raman intensities are in arbitrary units, a constant line width of 6 cm^{-1} was assumed.

Table 2
Calculated frequencies, IR intensities and the total Raman scattering activity of azidopentazole

Frequencies (cm^{-1})	IR (km/mol)	Raman ($Å^4$/amu)
54	0.1	0.2
151	0.5	7.8
264	2.6	1.1
392	1.7	6.1
463	2.5	0.1
525	0.4	5.2
667	0.6	0.0
727	0.0	0.0
755	4.6	4.1
921	46.7	36.2
1009	1.1	2.3
1060	1.7	10.6
1082	0.1	4.9
1159	14.5	8.0
1194	5.2	3.2
1311	11.8	25.4
1345	89.4	63.3
2164	369.5	108.7

nitrogens. The strong Raman activity of these modes can be qualitatively understood by noting that the size of molecule changes for these vibrations. Since the molecular polarizability is roughly proportional to the volume, the effective polarizability changes and therefore the modes are Raman active. Small movies illustrating the movement of the nitrogen atoms according to the vibrational modes are available from the authors upon request.

Our calculated vibrational frequencies are in good agreement with results from Glukhovtsev et al. [1] who have calculated the harmonic vibrational frequencies and infrared intensities at the B3LYP/6-31G* level of theory. Their frequencies range between 41 and 2267 cm^{-1}. Both calculations find the highest mode to be the strongest IR active mode. The IR intensity of 384 km/mol given in that work [1] agrees well with our value of 369.5 km/mol. The relative ordering of the strength of the IR active modes agrees for the six strongest IR active modes, however, the numerical agreement gets worse. In particular the seventh and eighth strongest mode are ordered differently in the two calculations. Nevertheless the agreement of the six strongest modes in both calculations should give confidence in the reliability of these theoretical predictions, whereas the prediction of the weak IR active modes is probably influenced by chosen basis sets and numerical errors.

4. Conclusions

Using first-principles all-electron density-functional calculations we have studied the structural, electronic and vibrational properties of the still experimentally elusive N_8 isomer azidopentazole. In agreement with earlier work we have found azidopentazole to be the most stable N_8 isomer predicted so far, although it does have a low barrier for decomposition to molecular nitrogen.

Although azidopentazole has not yet been experimentally observed, there have been a number of highly energetic molecules which were once believed not to exist (e.g. C_8H_8 (cubane) [23], $C_8N_8O_{16}$ (octanitrocubane) [24] and the cation N_5^+ [8]) and were successfully synthesized.

Our calculated IR and Raman spectra contain useful information, which would be needed to identify azidopentazole if a successful synthesis is found. In addition to the frequencies we calculated IR and Raman intensities. The strongest IR modes are in good agreement with earlier reports. To the best of our knowledge no Raman intensities have been previously reported. Successful observation of the azidopentazole Raman modes would experimentally confirm the presence of the molecule and suggest reasonable stability.

We hope that this work supports the search for the interesting but still elusive species azidopentazole.

Acknowledgements

J.K. and M.R.P. were supported in part by ONR grant N0001498WX20709. S.L.R. acknowledges support from the US Navy–American Society for Engineering Education (ASEE) Faculty Sabbatical Leave and Summer Research Programs.

References

[1] M.N. Glukhovtsev, H. Jiao, P.v.R. Schleyer, Inorg. Chem. 35 (1996) 7124.
[2] M.T. Nguyen, T.K. Ha, Chem. Ber. 129 (1996) 1157.
[3] G. Chung, M.W. Schmidt, M.S. Gordon, J. Phys. Chem. 104 (2000) 5647.
[4] L. Gagliardi, S. Evangelisti, A. Bernhardsson, R. Lindh, B.O. Roos, Int. J. Quantum Chem. 77 (2000) 311.
[5] L. Gagliardi, S. Evangelisti, P.-O. Widmark, B.O. Roos, Theor. Chem. Acc. 97 (1997) 136.
[6] J. Kortus, M.R. Pederson, S.L. Richardson, submitted for publication.
[7] P.E. Eaton, Angew. Chem. 31 (1992) 1421.
[8] J.A. Pople, J.S. Binkley, R. Seeger, Int. J. Quantum Chem. S10 (1976) 1.
[9] K.O. Christie, W.W. Wilson, J.A. Sheehy, J.A. Boatz, Angew. Chem. Int. Ed. 38 (1999) 2004.
[10] P. Hohenberg, W. Kohn, Phys. Rev. 136 (1964) B864.
[11] W. Kohn, L.J. Sham, Phys. Rev. 140 (1965) A1133.
[12] M.R. Pederson, K.A. Jackson, Phys. Rev. B 41 (1990) 7453.
[13] K.A. Jackson, M.R. Pederson, Phys. Rev. B 42 (1990) 3276.
[14] D.V. Porezag, M.R. Pederson, Phys. Rev. B 54 (1996) 7830.
[15] D.V. Porezag, M.R. Pederson, Phys. Rev. A 60 (1999) 9566.
[16] M.R. Pederson, D.V. Porezag, J. Kortus, D.C. Patton, Phys. Stat. Sol. (b) 217 (2000) 197.
[17] J.P. Perdew, K. Burke, M. Ernzerhof, Phys. Rev. Lett. 77 (1996) 3865.
[18] H. Hellmann, in: Einführung in die Quantentheorie, Deuticke, Leipzig, 1937.
[19] R.P. Feynman, Phys. Rev. 56 (1939) 340.
[20] P. Pulay, Mol. Phys. 17 (1969) 197.
[21] M.R. Pederson, A.A. Quong, J.Q. Broughton, J.L. Feldman, Comput. Mater. Sci. 2 (1994) 536.
[22] L. Gagliardi, S. Evangelisti, B.O. Roos, P.-O. Widmark, J. Mol. Struct. (Theochem.) 428 (1998) 1.
[23] P.E. Eaton, T.W. Cole Jr., J. Am. Chem. Soc. 86 (1964) 962.
[24] M.-X. Zhang, P.E. Eatona, R. Gilardi, Angew. Chem. Int. Ed. 39 (2000) 401.

Appendix H

Kortus J. and Pederson M. R.

Magnetic and vibrational properties of the uniaxial $Fe_{13}O_8$ cluster

Phys. Rev. **B 62**, 5755-5759 (2000)

Magnetic and vibrational properties of the uniaxial $Fe_{13}O_8$ cluster

Jens Kortus and Mark R. Pederson
Center for Computational Materials Science, Code 6390, Naval Research Laboratory, Washington, DC 20375
(Received 29 March 2000)

We have performed all-electron density-functional-based calculations on the recently synthesized iron oxide $Fe_{13}O_8$ cluster. The $Fe_{13}O_8$ cluster shows a complicated magnetic structure, with several magnetically stable ferro-, ferri-, and antiferromagnetic states. The most stable state is a ferromagnetic state with a total moment of $32\mu_B$ per cluster. We report a systematic investigation of the electronic and magnetic structure of different magnetic states. For the most stable ferromagnetic state we calculate the magnetic anisotropy barrier and the complete vibrational spectra including IR and Raman intensities from density functional theory.

I. INTRODUCTION

Due to their very interesting magnetic properties, which are analogous to magnetic metallic nanoparticles, several magnetic molecules have received significant experimental interest recently. Such molecules include Mn_{12}-acetate and the octanuclear Fe(III) clusters,[1] which have high total spins and large anisotropy energies, and the layered V_{15} cluster,[2] which has a small net spin. These clusters have been studied as prototypical systems which exhibit magnetism at the nanoscale. As shown in a series of experiments, the Mn_{12}-acetate cluster[1] exhibits a magnetic hysteresis and quantum tunneling of the magnetic orientation. Upon application of well-defined magnetic fields, discontinuities in the hysteresis loops appear, indicating a switching of moment orientation. In 1937 Van Vleck explained that the moment-reorientation temperature is determined by the magnetic anisotropy energy, which itself is due to relativistic interactions such as spin-orbit coupling.[3]

Understanding and influencing the magnetic anisotropy energy is one of the challenges in the field of nanoscale magnets since the magnetic anisotropy energy ultimately governs the potential use of a nanomagnet in information storage devices. A short introduction to the technological importance of magnetic nanocrystals for data storage can be found in Ref. 4.

Recently, Wang *et al.*[5] synthesized a new iron oxide cluster by reactive laser vaporization. From time of flight mass spectra and first-principles calculations[5,6] they respectively concluded that this iron oxide cluster consists of 13 iron and 8 oxygen atoms with D_{4h} symmetry. Comparing the stability of this cluster with other possible structures showed that the $Fe_{13}O_8$ with D_{4h} symmetry is the most stable cluster. Wang and co-workers[5] have discussed the need for understanding the Fe-O interactions because of the role that such interactions play in corrosion, biological processes, and oxide film formation. Further, their reported moments of approximately $2\mu_B$ per iron atom[5] suggest potential applications of this cluster as a nanomagnet. Therefore additional investigations on the electronic and vibrational structure, spin-ordering, magnetic states, and the magnetic anisotropy barrier of this cluster are indeed vital.

Sun and co-workers[6] have reported the calculation of the vibrational modes of $Fe_{13}O_8$, finding local stability of this iron oxide cluster, because all calculated vibrational frequencies are real. However, the frequencies given in Table II of that work[6] range between 3.9 cm^{-1} to 22.16 cm^{-1} which are unusually low. Results presented in this work suggest that there may be a conversion error in their calculations.

In this paper we present results from all-electron density-functional-based studies of the $Fe_{13}O_8$ cluster as a function of magnetic state and spin ordering and provide density-functional-based infrared and Raman spectra. For other transition metal oxides such as $Mn_{12}O_{12}$ (Refs. 7–9) and the octanuclear iron(III) cluster[1] antiferromagnetic couplings are known to be important and antiferromagnetic or ferrimagnetic ground states are observed in these systems. Because of the coupling of the magnetic and structural degrees of freedom, consideration of ferro-, ferri-, and antiferromagnet ordering is an important issue from the standpoint of determining the ground state of a magnetic molecule. As such, the investigation of different possible spin orderings as well as total moments is one of the primary aims of this paper. For the most stable structure obtained we calculate the vibrational spectra in order to clarify some questions raised with the reported values by Sun and co-workers.[6] In Sec. II we provide details on the computational methods employed and the basis sets used. A short discussion of the calculation of the magnetic anisotropy energy is also given there. In Sec. III we discuss the results for the different magnetic couplings and the vibrational spectra for the most stable geometry found. We conclude by summarizing our results in Sec. IV.

II. COMPUTATIONAL DETAILS

The density-functional-theory (DFT) calculations were performed with the all-electron Gaussian-orbital-based NRLMOL program.[10] NRLMOL is specifically designed for studies of molecules and clusters and does not use periodic boundary conditions. All calculations discussed here use the Perdew-Burke-Ernzerhof (PBE) generalized-gradient approximation (GGA) for the density functional.[11] NRLMOL combines large Gaussian-orbital basis sets, numerically precise variational integration, and an analytic solution of Poisson's equation in order to accurately determine the self-consistent potentials, secular matrix, total energies, and Hellmann-Feynman-Pulay forces. In conjunction with the conjugate-gradient algorithm, the Hellmann-Feynman-Pulay

0163-1829/2000/62(9)/5755(5)/$15.00

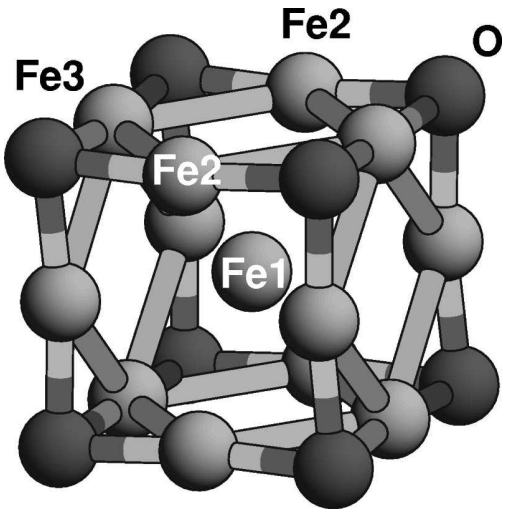

FIG. 1. The structure of the iron oxide $Fe_{13}O_8$ cluster with D_{4h} symmetry. The dark balls at the corners are the eight oxygen atoms and the lighter balls are the Fe atoms.

forces are used to iteratively optimize the molecular geometries. The process is stopped after the largest nuclear gradient is found to be smaller than 0.05 eV/Å.

The exponents for the single Gaussians have been fully optimized for DFT calculations.[12] The basis set for the iron atoms includes 20 bare Gaussians ranging between $3.866\,75\times10^6$ and 0.045 179 which are contracted to 12 s-like, 5 p-like, and 5 d-like atomic orbitals. The basis set for the oxygen atoms includes 13 bare Gaussians between 6.121×10^4 and 0.1049 which are contracted to 9 s-like, 4 p-like, and 4 d-like atomic orbitals. As proved in Ref. 12, in order to obtain errors in total energies that are smaller than a prescribed tolerance the shortest-range Gaussian exponent must scale at least as fast as $CZ^{10/3}$ where Z is the nuclear charge and C is a constant that determines the accuracy of the core energy. The basis sets developed in Ref. 12 obey this scaling law.

The NRLMOL code has been successfully applied to several problems with $3d$ transition metals, such as the magnetic and structural ordering in small iron clusters,[13] the structure of small Mn_n clusters,[14] and the calculation of the magnetic anisotropy barrier in $Mn_{12}O_{12}$-acetate molecules.[8,9,15] Using the methodology described in Ref. 16 NRLMOL can be used to calculate the vibrational modes and the IR and Raman intensities from first principles.

In Fig. 1 we show our structure of the $Fe_{13}O_8$ cluster. In order to facilitate comparison with the recent work of Sun *et al.*[6] we have adopted the labeling scheme used in their work. Using D_{4h} symmetry the cluster has three inequivalent iron atoms [Fe(1), Fe(2), and Fe(3), respectively] and one oxygen atom. All other atoms are related by symmetry.

The $Fe_{13}O_8$ cluster shows complicated magnetic properties and allows for several different couplings between the iron atoms which will be discussed separately in the following sections. Due to the coupling between magnetic and structural properties, each magnetic state requires a separate geometry optimization. We confine our discussion to D_{4h} symmetry for the iron oxide cluster in order to compare our results with earlier work[6] and because the number of stable magnetic solutions is already very large.

An investigation of several magnetic configurations with O_h symmetry showed that these configurations are at least 1 eV higher in energy than the lowest-energy state with D_{4h} symmetry found. As shown later in this paper the lowest-energy configuration is also vibrationally stable so it is at least a locally metastable geometry. Further, we have determined that distortions of 1.25 a.u. along the softest symmetry breaking vibrational mode lead to an increase in energy of 0.2 eV, showing a predominantly parabolic behavior in this range. Since there is no rigorous method known for obtaining the ground-state geometry of a multiatom system, a comparison between theoretically and experimentally determined physical observables, such as the vibrational spectra and anisotropy energies, can provide an indirect method for ascertaining the global stability of a cluster geometry.

A way to determine whether a magnetic state is at least metastable is to examine the highest occupied molecular orbital (HOMO) and lowest unoccupied molecular orbital (LUMO) levels of the majority and minority spin. The spin gaps, defined as

$$\Delta_1 = -(\epsilon^{\mathrm{maj}}_{\mathrm{HOMO}} - \epsilon^{\mathrm{min}}_{\mathrm{LUMO}}), \tag{1}$$

$$\Delta_2 = -(\epsilon^{\mathrm{min}}_{\mathrm{HOMO}} - \epsilon^{\mathrm{maj}}_{\mathrm{LUMO}}), \tag{2}$$

correspond to the energy required to transfer an infinitesimal amount of charge from the HOMO of one spin to the LUMO of the other one. The system can only be magnetically stable if both spin gaps are positive. Further, if the spin gaps are not both positive, they determine whether an increase or decrease of total moment will stabilize the system.

Magnetic anisotropy energy

As discussed in Ref. 15, upon introduction of spin-orbit coupling, the anisotropy Hamiltonian of a uniaxial molecule can be written according to

$$H = \alpha S^2 + \beta S_z^2 . \tag{3}$$

If β is positive, the molecule has an easy plane of magnetization, for negative β it has an easy axis along which the moment will align itself. The calculation of the second-order contributions to the magnetic anisotropy energy (MAE) is derived in Ref. 15. The method uses a simplified but exact method for incorporating spin-orbit coupling into density-functional and other mean-field theories. In uniaxial systems the MAE is primarily due to spin-orbit effects and normally on the order of several tens of kelvin. The MAE can be obtained from the parameter β and the maximum expectation value of the spin operator S_z directly:

$$\Delta_{\mathrm{MAE}} = \beta \langle S_z \rangle^2 . \tag{4}$$

For systems such as the clusters studied here, which have a HOMO-LUMO gap that is large compared to a typical spin-orbit interaction, second-order perturbation theory can be used to determine the value of β.[15] This procedure has been carried out in applications for the uniaxial Mn_{12}-acetate molecule and has been shown to be very accurate. In order to give an estimate of the accuracy of the method employed here we note that for the Mn_{12}-acetate nanomagnet the agree-

TABLE I. Highest occupied molecular orbital (HOMO), lowest unoccupied molecular orbital (LUMO), spin gaps Δ, and the energy (ΔE) of the optimized structures with respect to the most stable state with $32\mu_B$ for $Fe_{13}O_8$ in the ferromagnetic state for different total moments of the cluster. The energies are given in eV. The definition of the spin gaps Δ is given in the text.

Total moment	$20\mu_B$	$26\mu_B$	$32\mu_B$	$34\mu_B$
Majority HOMO	−4.62	−4.54	−5.08	−4.64
Majority LUMO	−4.22	−4.25	−4.50	−4.37
Minority HOMO	−4.23	−4.29	−4.63	−4.78
Minority LUMO	−4.10	−4.21	−4.30	−4.50
Spin gap Δ_1	0.52	0.33	0.78	0.14
Spin gap Δ_2	0.01	0.04	0.13	0.41
ΔE	1.554	1.096	0	0.003

ment between the calculated second-order contributions to the MAE (55.7 K) and the experimental value (55.6 K) is excellent.[8,9,15,17]

III. RESULTS AND DISCUSSION

A. Ferromagnetic coupling

Within the constraint of D_{4h} symmetry we performed a rather exhaustive search of the possible ferromagnetic states. First, using D_{4h} symmetry we optimized the geometry of the cluster with a ferromagnetic state corresponding to a total moment of $20\mu_B$. Both spin gaps $\Delta_1 = 0.516$ eV and $\Delta_2 = 0.012$ eV are positive, which show that this state is at least metastable. However, Δ_2 is small, indicating that another ferromagnetic state obtained by transferring charge from the minority spins to the majority ones could also lead to a metastable state. Starting from this geometry we carried out 16 different calculations with fixed total moments of the cluster ranging between $20\mu_B$ and $52\mu_B$. Using the above-defined criteria of positive spin gaps for both spins we determined the magnetically metastable configurations for which we further optimized the geometry within the constraint of this given moment. In some cases one of the spin gaps became negative during the geometry optimization. In theses cases we changed the moment accordingly and relaxed the geometry further. This approach resulted in the identification of four metastable ferromagnetic states with total moments of $20\mu_B$, $26\mu_B$, $32\mu_B$, and $34\mu_B$. The magnetic states with $32\mu_B$ and $34\mu_B$ were found to be the most stable ones. These states are energetically nearly degenerate with the $34\mu_B$ state only 3 meV higher in energy. The most stable structure found, was the state with $32\mu_B$. In Table I we give the HOMO, LUMO, and gap for both spin channels, and the energy of the optimized geometries with respect to the lowest-energy state with $32\mu_B$.

Using the same labels as Ref. 6, the bond lengths and bond angles of the optimized geometry of the cluster with ferromagnetic coupling and a total moment of $32\mu_B$ are given by $r_{\text{O-Fe(1)}} = 3.3139$ Å, $r_{\text{O-Fe(2)}} = 1.8948$ Å, and $r_{\text{O-Fe(2)}} = 1.8508$ Å, and $\angle$O-Fe2-O$= 157.4°$ and $\angle$O-Fe3-O$= 177.2°$. The average moment of $2.46\mu_B$ per iron atom is larger than the average moment of $2.061\mu_B$ given by Wang *et al.*[5] Their value corresponds to a total moment of about $26\mu_B$, which from our calculations is a less stable magnetic state.

In order to compare the local moments we placed a sphere with a radius of 1.32 Å around the atoms and calculated the charge within the sphere. For the center Fe atom we find a moment of $2.82\mu_B$ and $2.70\mu_B$ and $1.66\mu_B$ for the other two iron atoms. Our local moments are larger than the previous reported ones,[5] which agrees with the larger total moment we found. The fact that the largest moment is found on Fe(1) and the smallest one on Fe(3) is in good agreement with that earlier work.

The magnetic anisotropy barrier,[9] which gives the energy to flip the spin projection, is an important figure of merit for applications of nanomagnets for information storage. Besides the large total moment of $32\mu_B$ the iron-oxide cluster has an anisotropy barrier calculated from second-order perturbation theory of 33.4 K. The parameter β from Eq. (4) has a value of $4 \times 33.4/32^2 = 0.1305$ K.

Although a magnetic anisotropy barrier of 30 K is large at the molecular level, this effect is still one order of magnitude too small for devices working at room temperature. The MAE is a very sensitive property of electronic structure, magnetic ordering, and cluster geometry. The MAE for the energetically nearly degenerate state with $34\mu_B$ changes to 52 K. This strong dependence will make experimental measurements of the MAE more difficult because the result will depend strongly on the experimental conditions. On the other hand, it indicates a rich potential to influence and tune the MAE according to application requirements. A simple explanation based on the number of interactions between occupied and unoccupied states in both spin channels and the spin gaps alone is not sufficient for explaining the change of the MAE. In order to attain the goal of tuning the MAE for device applications more insight is required for understanding all interactions which influence the MAE.

Closely connected to this problem is the interaction of the free cluster with its environment because potential technical applications for any nanomagnet would require supporting them on substrates or possibly embedding them within other condensed media. The cluster-support interaction could change the magnetic properties of the isolated cluster since bond formation and/or charge transfer between the cluster and substrate could occur upon chemisorption of the clusters. More generally the overall symmetry of the anisotropy Hamiltonian would change which could effect the magnetic bistability of the cluster. Further such effects would depend on whether the cluster was adsorbed with the easy axis perpendicular or parallel to the substrate surface. Finally all of these effects would be strongly dependent on substrate choice. Additional detailed investigations of these problems need to be performed to quantify the effects of substrate-adsorbate interactions on the magnetic properties of small particles. Calculations aimed at understanding the effects of these interactions are currently in progress. A good introduction to the related experimental and theoretical problems associated with interactions between adsorbates and substrates is given by Selwood.[18] However, prior to addressing interactions between a magnetic particle and the host it is necessary to have a complete understanding of the magnetic configurations of the isolated particle and we turn to this point here.

B. Ferrimagnetic coupling

If orbitals are spatially orthogonal and occupy the same region in space, parallel alignment of the spins leads to a larger exchange interaction energy and ferromagnetic coupling is subsequently favored. Antiferromagnetic coupling occurs in cases where the orbitals are spatially separated but nonorthogonal. In such cases antiparallel alignment of the spins bypasses the need for spatial orthogonality and provides for a reduction in the kinetic energy. An example of antiferromagnetic interactions in clusters is the $Mn_{12}O_{12}$ tower structure observed by Ziemann and Castleman.[7,9] In this structure the net moment is zero. Antiferromagnetic coupling is experimentally observed in the octanuclear iron(III) cluster $[Fe_8O_2(OH)_{12}(tacn)_6]^{8+}$, which shows antiferromagnetic coupling between neighboring irons. However, the local moments do not entirely compensate one another, leading to an nonvanishing total moment of the cluster and ferrimagnetic order.[1,8,9] The magnetic spinel Fe_3S_4 also shows a ferrimagnetic spin arrangement.[19]

From these experiences we expect that antiferromagnetic interactions could also play an important role for the iron oxide clusters and a complete investigation of spin ordering in this system is required.

Using the same approach as in the ferromagnetic case we started with 12 different fixed total moments between $0\mu_B$ and $20\mu_B$. In order to obtain antiferromagnetic solutions we used a starting potential which favored antiferromagnetic coupling between the Fe(2) and Fe(3) atoms. During the self-consistency cycle no constraints on the electronic degrees of freedom were applied and the coupling between the Fe(1) atom and the other two atoms was determined self-consistently. By calculating the self-consistent local moments for each atom we determined whether the solution had converged to a state with antiferromagnetic coupling. The geometries of all states with positive spin gaps were further optimized.

We find antiferromagnetic and several ferrimagnetic states with total moments $4\mu_B$, $8\mu_B$, $10\mu_B$, $12\mu_B$, $13\mu_B$, $14\mu_B$, and $15\mu_B$ to be metastable magnetic states for the iron oxide cluster. The ferrimagnetic states with $12\mu_B$, $13\mu_B$, $14\mu_B$, and $15\mu_B$ have twofold states at the Fermi level, which are not fully occupied, suggesting that Jahn-Teller distortions would lead to a reduction in symmetry.

All these states are close in energy and show similar behavior. The magnetic state with $14\mu_B$ is the lowest-energy state exhibiting antiferromagnetic coupling between the Fe atoms. However, this state is 86 meV higher in energy than the ferromagnetic state with $32\mu_B$. Results for the HOMO, LUMO, and spin gaps for some of the more interesting magnetic states are given in Table II. The energy ΔE is the energy with respect to the ferromagnetic state with $32\mu_B$, which was the most stable state found for all magnetic configuration.

The bond lengths of the most stable ferrimagnetic state with a total moment of $14\mu_B$ are $r_{\text{O-Fe(1)}}=3.232\,18$ Å, $r_{\text{O-Fe(2)}}=1.8878$ Å, and $r_{\text{O-Fe(2)}}=1.8393$ Å; the bond angles did not change much: $\angle$O-Fe2-O$=169.8°$ and $\angle$O-Fe3-O$=174.7°$. The local moments within a sphere are Fe(1), $2.7320\mu_B$; Fe(2), $-2.7349\mu_B$; and Fe(3), $2.6794\mu_B$.

TABLE II. HOMO, LUMO, and spin gaps Δ for $Fe_{13}O_8$ with antiferromagnetic coupling for states with different total moment. ΔE gives the energy with respect to the ferromagnetic state with with $32\mu_B$, which was the most stable state found. The energies are given in eV.

Moment	$0\mu_B$	$4\mu_B$	$8\mu_B$	$10\mu_B$	$12\mu_B$	$14\mu_B$
Majority HOMO	−4.58	−4.47	−4.61	−4.56	−4.60	−4.42
Majority LUMO	−4.22	−4.25	−4.37	−4.34	−4.28	−4.42
Minority HOMO	−4.48	−4.47	−4.52	−4.55	−4.30	−4.51
Minority LUMO	−4.04	−4.11	−4.12	−4.18	−4.30	−4.31
Δ_1	0.53	0.36	0.49	0.38	0.30	0.11
Δ_2	0.26	0.22	0.15	0.21	0.02	0.09
ΔE	0.70	0.75	0.31	0.20	0.12	0.09

C. Vibrational spectra

In order to find the vibrational spectra of the $Fe_{13}O_8$ cluster within the harmonic approximation we need to calculate the dynamical or Hessian matrix. For the calculation of all matrix elements of the dynamical matrix we need only 14 different geometries due to the D_{4h} symmetry of the cluster. Diagonalizing the dynamical matrix gives directly the vibrational frequencies and eigenmodes. As explained in detail in Ref. 16, 12 additional self-consistent field calculations are necessary for the determination of the polarizability tensor and the dipole moment, which are the required ingredients for calculating IR and Raman intensities.

In Fig. 2 we show the vibrational spectra including IR and Raman intensities calculated from density-functional theory. We find that the ferromagnetic state with a moment of $32\mu_B$ per cluster is locally stable. Our frequencies range from 29.7 cm^{-1} as the lowest to 660 cm^{-1} as the highest frequency. These values differ by an order of magnitude from the frequencies given by Sun and co-workers.[6] A good test for the numerical accuracy of our calculations is the value of the trivial frequencies of the three translational and rotational

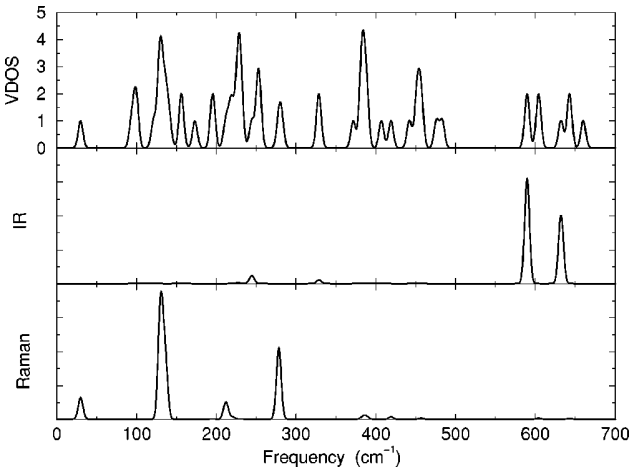

FIG. 2. The upper panel displays the calculated vibrational density of states (VDOS), the middle panel the IR spectra, and the lower panel the Raman spectra of the most stable ferromagnetic iron oxide $Fe_{13}O_8$ cluster with D_{4h} symmetry. The lowest frequency is 29.7 cm^{-1}. The IR and Raman intensities are in arbitrary units; a constant line width of 6 cm^{-1} was assumed.

modes which should be zero, which we also obtain from diagonalizing the dynamical matrix. The largest absolute value for one of these six modes is 0.000 012 cm^{-1}.

Our results are closer in magnitude to those of the Fe dimer, where different levels of theory give values between 350 cm^{-1} and 500 cm^{-1} with an experimental value[20] of 300 cm^{-1}. The value obtained by NRLMOL within the standard local spin density approximation was reported earlier as 418 cm^{-1} in Ref. 13 which changes to 406 cm^{-1} for the PBE-GGA exchange-correlation functional. Since the NRLMOL code has been successfully applied to the calculation of vibrational spectra[21–25] with very good agreement to experiment, we are confident in the results reported here. The calculated IR and Raman intensities could be useful for experiments investigating the iron oxide cluster.

IV. SUMMARY

In this paper we have investigated the magnetic coupling between iron atoms in the interesting $Fe_{13}O_8$ iron oxide cluster using first-principles density-functional calculations with the PBE-GGA functional for the exchange-correlation functional. Several metastable ferro- and ferrimagnetic states with different total moments per cluster have been found. The antiferromagnetic state is also magnetically metastable. The state with the lowest energy is a ferromagnetic state with $32\mu_B$ per molecule, which is nearly energetically degenerate with a ferromagnetic state with $34\mu_B$ being only 3 meV lower in energy. Several ferrimagnetic states are also close in energy. The observed ground state for the iron oxide cluster differs from a previous reported ferromagnetic state ($26\mu_B$) by Wang and co-workers.[5]

The calculation of the vibrational spectra shows, in agreement with reports of Sun *et al.*,[6] that the cluster is vibrationally stable within D_{4h} symmetry, although our calculated frequencies differ significantly from earlier reported ones. Besides the frequencies we calculated the IR and Raman spectra which could be helpful for vibrational spectroscopy studies. Several magnetic configurations with O_h symmetry have been studied and are found to be at least 1 eV higher in energy than the lowest-energy state with D_{4h} symmetry found.

The high magnetic moment of $32\mu_B$ and a magnetic anisotropy energy of 33.4 K suggest that this cluster may be an interesting nanomagnet if collection and assembly of reasonably large quantities of these clusters is possible. The cluster should show similar interesting behavior of magnetic hysteresis and tunneling of the magnetic orientation as found in other nanomagnets.[1]

From a practical point of view additional systematic studies of the influence of passivation and chemisorption on the magnetic properties of these and other clusters is of current interest. These interactions are important for understanding experiments and may enable one to design materials with given magnetic properties. Work in this direction is currently being carried out.

ACKNOWLEDGMENTS

This work was supported in part by ONR (Grant Nos. N0001400WX2011 and N0001498WX20709).

[1] A. Caneschi, D. Gatteschi, C. Sangregorio, R. Sessoli, L. Sorace, A. Cornia, M.A. Noval, C. Paulsen, and W. Wernsdorfer, J. Magn. Magn. Mater. **200**, 182 (1999), and references therein.

[2] D. Gatteschi, L. Pardi, A.L. Barra, A. Müller, and J. Döring, Nature (London) **354**, 463 (1991).

[3] J. Van Vleck, Phys. Rev. **52**, 1178 (1937).

[4] R.F. Service, Science **287**, 1902 (2000); S. Sun, C.B. Murray, D. Weller, L. Folks, and A. Moser, *ibid.* **287**, 1989 (2000).

[5] Q. Wang, Q. Sun, M. Sakurai, J.Z. Yu, B.L. Gu, K. Sumiyama, and Y. Kawazoe, Phys. Rev. B **59**, 12 672 (1999).

[6] Q. Sun, Q. Wang, K. Parlinski, J.Z. Yu, Y. Hashi, X.G. Gong, and Y. Kawazoe, Phys. Rev. B **61**, 5781 (2000).

[7] P.J. Ziemann and A.W. Castleman, Jr., Phys. Rev. B **46**, 13 480 (1992).

[8] M.R. Pederson and S.N. Khanna, Chem. Phys. Lett. **307**, 253 (1999).

[9] M.R. Pederson and S.N. Khanna, Phys. Rev. B **59**, R693 (1999).

[10] M.R. Pederson and K.A. Jackson, Phys. Rev. B **41**, 7453 (1990); K.A. Jackson and M.R. Pederson, *ibid.* **42**, 3276 (1990).

[11] J.P. Perdew, K. Burke, and M. Ernzerhof, Phys. Rev. Lett. **77**, 3865 (1996).

[12] D. Porezag and M.R. Pederson, Phys. Rev. A **60**, 2840 (1999).

[13] J.L. Chen, C.S. Wang, K.A. Jackson, and M.R. Pederson, Phys. Rev. B **44**, 6558 (1991).

[14] M.R. Pederson, F. Reuse, and S.N. Khanna, Phys. Rev. B **58**, 5632 (1998).

[15] M.R. Pederson and S.N. Khanna, Phys. Rev. B **60**, 9566 (1999).

[16] D.V. Porezag and M.R. Pederson, Phys. Rev. B **54**, 7830 (1996).

[17] A.L. Barra, D. Gatteschi, and R. Sessoli, Phys. Rev. B **56**, 8192 (1997).

[18] P.W. Selwood, *Chemisorption and Magnetization* (Academic Press, New York, 1975).

[19] M.R. Spender, J.M.D. Coey, and A.H. Morrish, Can. J. Phys. **50**, 2313 (1971).

[20] E.G. Moroni, G. Kresse, J. Hafner, and J. Furthmüller, Phys. Rev. B **56**, 15 629 (1997), and references therein.

[21] A. Briley, M.R. Pederson, K.A. Jackson, D.C. Patton, and D.V. Porezag, Phys. Rev. B **58**, 1786 (1998).

[22] K.A. Jackson, A. Briley, S. Grossman, D.V. Porezag, and M.R. Pederson, Phys. Rev. B **60**, R14 985 (1999).

[23] D.C. Patton, D.V. Porezag, and M.R Pederson, Phys. Rev. B **55**, 7454 (1997).

[24] M.R. Pederson, K. Jackson, D.V. Porezag, Z. Hajnal, and Th. Frauenheim, Phys. Rev. B **54**, 2863 (1996); A. Sieck, D. Porezag, Th. Frauenheim, M.R. Pederson, and K.A. Jackson, Phys. Rev. A **56**, 4890 (1997); K.A. Jackson, M.R. Pederson, D.V. Porezag, Z. Hajnal, and Th. Frauenheim, Phys. Rev. B **55**, 2549 (1997).

[25] A.A. Quong, M.R. Pederson, and J.L. Feldman, Solid State Commun. **87**, 535 (1993).

Appendix I

Kortus J., Baruah T., Pederson M. R., Khanna S. N. and C. Ashman

Magnetic moment and anisotropy in Fe_nCo_m Clusters

Appl. Phys. Lett. **80**, 4193-4195 (2002)

Magnetic moment and anisotropy in Fe_nCo_m clusters

J. Kortus,[a] T. Baruah,[a] and M. R. Pederson
Center for Computational Materials Science, Code 6390-Naval Research Laboratory, Washington, DC

C. Ashman and S. N. Khanna[b]
Physics Department, Virginia Commonwealth University, Richmond, Virginia 23284-2000

(Received 10 December 2001; accepted for publication 5 April 2002)

Electronic structure calculations of Fe_nCo_m ($n+m=5$ and 13) are used to examine the effects of alloying on the magnetic moment and magnetic anisotropies. Our density-functional studies show that many mixed clusters have moments comparable to or higher than the pure clusters. The mixed clusters, however, have very low anisotropies and could be ideal as soft magnetic materials. It is shown that shape, composition, and compositional ordering must be considered for optimization of anisotropy energies. © *2002 American Institute of Physics.* [DOI: 10.1063/1.1482793]

Extensive research over the past decade has shown that small clusters offer a class of magnetic properties. Clusters of itinerant ferromagnetic solids Fe, Co, and Ni have higher magnetic moments per atom than the corresponding bulk;[1] clusters of nonmagnetic solids like Rh are spin polarized;[1,2] and atomic moments in clusters of Mn, which exhibits complex magnetic order in the bulk, are ferromagnetically aligned.[3,4] The reduction in particle size also leads to new dynamical behaviors. For a particle with a size smaller than the typical magnetic domain size, the atomic moments are exchange coupled and the particles behave as a single magnet with a combined moment from the individual atoms. However, the anisotropy energy (AE) that determines the minimum energy required to reorient this combined magnetic moment decreases with size and typically becomes comparable to thermal energies in particles of about 10 nm. These particles then undergo superparamagnetic (SP) relaxation.[5–8] A fundamental understanding of the magnetic anisotropy energy (MAE), which controls the onset of SP behavior is therefore requisite to the design of molecular scale magnets.

While there has been considerable effort in the past to understand the evolution of the magnetic moment, the few theoretical attempts to understand the MAE in clusters have been limited to semiempirical approaches.[10] Recently Zhou *et al.*[11] have shown that the MAE in clusters and low-dimensional systems can be affected by the orbital-correlation terms. However in the absence of a precise recipe for derivation of the orbital-polarization or correlation correction within density-functional theory, the conclusions of these papers can best be regarded as informative albeit qualitative.

The purpose of this letter is to examine the magnetic moment and the magnetic anisotropy in small Fe_nCo_m clusters. Bulk FeCo alloys exhibit the highest saturation magnetization and the limiting value, occurring around 35% Co, known as the Slater–Pauling limit, has long been regarded as the highest possible magnetization. Can this limit be overcome in clusters and, as a related issue, do the Fe_nCo_m clusters exhibit higher magnetization than pure Fe or Co clusters? The bulk alloys are used as soft magnetic materials due to their small magnetic anisotropy. The magnetic anisotropy of clusters is not known and the factors that control the magnetic anisotropy in these reduced sizes are not well understood. This line of inquiry is motivated by the possibility that the small anisotropy of the solid alloys may be enhanced by a chemical ordering of atoms in specialized geometries. To address these issues, we have carried out studies on several Fe_nCo_m clusters. Here, we present results on five and 13 atom clusters.

Our studies employed a linear combination of atomic-orbitals approach Naval Research Laboratory Molecular Orbital Library (NRLMOL)[12] within the generalized-gradient approximation (GGA)[13] to the density-functional theory. The basis sets used contained 20 bare Gaussians with exponents varying from 0.0452 to $3.866\,748\times10^6$ for Fe and 0.048 28 to $4.208\,47\times10^6$ for Co contracted to 11 *s*-like, 5 *p*-like and 4 *d*-like orbitals resulting in 46 basis functions for each atom. This large basis set shows great stability and gives reliable geometries. Detailed information on the construction of the Gaussian basis sets can be found in Ref. 14.

One focus of the present work is the calculation of the MAE. The main contribution to this quantity comes from the spin–orbit coupling and except for the cases where the second-order term is zero (due to symmetry), the most significant contribution comes from this term. For intrinsically uniaxial or lower-symmetry systems such as those discussed here the second-order contribution to the MAE is given by the change in the second-order spin–orbit energy (Δ_2) as the angle (θ) between the axis of symmetry and the quantization axis varies between 0 and $\pi/2$. For lower-symmetry systems, the second-order MAE depends on two angles. We have just proposed an implementation of the spin–orbit coupling that uses the exact representation given by $U(\mathbf{r},\mathbf{p},\mathbf{S}) = -1/2c^2\mathbf{S}\cdot\mathbf{p}\times\nabla\Phi(\mathbf{r})$. In addition to including some nonspherical contributions that would be absent in a standard $\mathbf{L}\cdot\mathbf{S}$ representation, the numerical implementation is particularly well suited to local-orbital methods such as NRLMOL.[15] Please note, while the scalar relativistic corrections (mass velocity and Darwin terms) have a $1/c^2$ contri-

[a]Also at: Department of Physics-Georgetown University, Washington, DC 20057.
[b]Electronic mail: khanna@hsc.vcu.edu

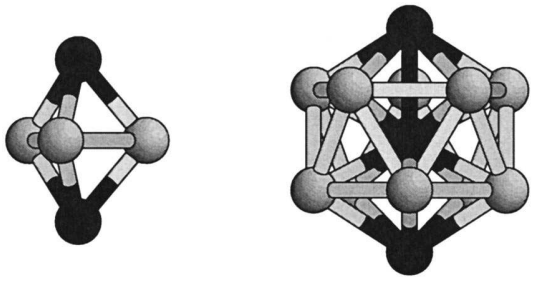

FIG. 1. The uniaxial geometrical configurations studied here include triangular bipyramid geometries ($N=5$) and distorted icosahedrons ($N=13$). For the mixed clusters, the dopant atoms were placed along the uniaxial axis.

bution to the single-electron Hamiltonian, these terms do not effect the second-order MAE for systems with real Kohn–Sham orbitals.

Some of the intermediate 13-atom clusters studied here have either no or a very small energy gap. As such the second-order perturbation method discussed in Ref. 15 is not obviously applicable so an exact-diagonalization method was developed. For a simple comparison, we found that the $S=3$ μ_B Fe_2 dimer has a second-order MAE of 5.36 K which is in good agreement with the 5.23 K result obtained from exact diagonalization.

In Fig. 1, we show the configurations studied in this work. The five- and 13-atom clusters are chosen because they allow for uniaxial structures. For pure uniaxial configurations, it is possible to further enhance the uniaxial character via substitution of different transition metal atoms along the axis of symmetry. This procedure allows for uniaxial clusters with compositions Fe_3Co_2, $Fe_{10}Co_3$, Co_3Fe_2, and $Co_{10}Fe_3$. For the smaller clusters ($N=5$), the uniaxially symmetric stable geometries have been further optimized for these stoichiometries with no symmetry constraints in order to find the influence of geometry on the MAE.

We start by comparing some of the present results with previous calculations. In Table I, we show the magnetic moments and the magnetic anisotropies of mixed Fe_nCo_m clusters. For Co_5, our calculated ferromagnetic ground state has D_{3h} symmetry, a magnetic moment of $13\mu_B$ and a binding energy of 11.67 eV. Fan *et al.*[16] have performed symmetry restricted density-functional calculations on Co_5 and find a C_{4v} ground state with a magnetic moment of $13\mu_B$ and a binding energy of 11.45 eV. Castro *et al.*, on the other hand, find a ground state with a moment of $9\mu_B$. The magnetic moments of Co_m clusters calculated by these authors increase monotonically from Co_2 to Co_4, but Co_5 has a lower moment than even Co_4. Possibly, these authors did not examine higher spin states. For Fe_5, our calculated moment is in agreement with earlier calculations by Castro *et al.*[17] The bond lengths are slightly different and we find a binding energy of 11.86 eV as compared to their calculated values of 10.98 eV. Postnikov *et al.*,[18] and Hobbs *et al.*,[19] have carried out *ab initio* molecular dynamics simulations on Fe_5 using GGA and local density approximation (LDA). While Hobbs *et al.* find a moment of 14.00 μ_B in the LDA, Postnikov *et al.*[18] find a moment of 18.00 μ_B. For the GGA, Postnikov *et al.* and Hobbs *et al.*[18,19] find moments of 18.00 μ_B. Since these studies are based on pseudopotentials, it is possible that the differences between these authors and the all electron calculation by us and Castro *et al.*[17] are due to the treatment of the core.

TABLE I. Symmetry group, magnetic moments, MAE, and smallest highest occupied molecular orbital–lowest unoccupied molecular orbital gaps for the ground-state Fe_nCo_m 5 atom clusters. EA (EP) means easy-axis (plane). TA stands for a system with three different axes. Anisotropy energies have been calculated using both second-order perturbation expressions (Ref. 10) and exact diagonalization methods. The two methods agree to 0.5–1.0 K for all cases. The [a] indicates majority–minority gap,[b] indicates minority–majority gap.

Cluster	Symmetry		Moment μ_B	MAE (K)	GaP (eV)
Co_5	D_{3h}	EA	13	6	0.41[a]
Co_3Fe_2	C_s	TA	13	27/15	0.06[b]
Co_2Fe_3	D_{3h}	EP	16	21	0.59[a]
Fe_5	C_{2v}	EP	16	14	0.20[b]

TABLE II. Magnetic moment and MAE for relaxed 13-atom clusters with three central atoms constrained along the z axis (MAE-z) and fully unconstrained (MAE) for the Fe_nCo_m clusters. For Co_{13}, the fully relaxed cluster has a moment of 21 μ_b.

Cluster	Moment (μ_B)	MAE-z (K)	MAE (K)
Co_{13}	21	0	0
$Co_{10}Fe_3$	30	56	63
$Fe_{10}Co_3$	41	51	9
Fe_{13}	44	41	41

In Ref. 8, moments as a function of size for large Fe, Ni, and Co clusters are measured. While the smallest clusters in these studies are still large compared to those discussed here a reasonable extrapolation of 2.6 μ_B and 3.2 μ_B for Co and Fe agrees well with the present results. The magnetic moments per atom in bulk Co and Fe are 1.72 μ_B and 2.22 μ_B, respectively. Further, our predicted MAE for the pure clusters are well below room temperature. This is consistent with the Stern–Gerlach experiments on Fe_n and Co_n clusters cooled down to 77 K where the clusters are deflected in the same direction indicating a SP relaxation.[9]

We now discuss 13-atom clusters. We have investigated Co_{13}, Co_3Fe_{10}, $Co_{10}Fe_3$, and Fe_{13} clusters assuming C_{5v} and D_{2h} symmetries. For the mixed clusters, the substituted atoms have been added to preserve the uniaxial symmetry (Fig. 1). All 13-atom clusters are found to be easy-plane systems. The total magnetic moments obtained are given in Table II. It is seen that the magnetic moment increases as Co is substituted by Fe. In particular $Fe_{10}Co_3$ has a moment of 3.15 μ_B/atom which is almost 35% higher than the Slater–Pauling limit. The question arises as to whether the clusters are magnetically softer or harder than the corresponding solids.

Starting from the Hamiltonian obtained from self-consistent field (SCF) calculations without spin–orbit coupling, we calculated the spin–orbit matrix elements as described in Ref. 15 and obtained the MAE from exact diagonalization. Our earlier studies have shown that the magnetic anisotropy is mainly determined by the mixing of electronic states close to the Fermi energy. To further illustrate this dependence, we introduced an electronic temperature that allows the occupation of unoccupied states. The calculated AE as a function of the broadening temperature is

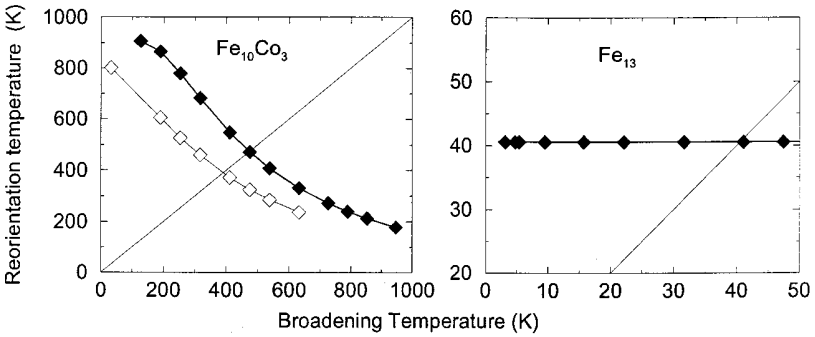

FIG. 2. Anisotropy energy as a function of electronic broadening temperature for clusters with imposed C_5 symmetry. The open squares for $Fe_{10}Co_3$ are results from SCF calculations at the same temperature as the broadening temperature. The intersection with the straight line corresponds to the moment reorientation temperature.

shown in Fig. 2. The results on the magnetic anisotropy at various electronic temperatures can also be used to estimate the blocking temperature, i.e., temperature above which the moments will reorient in different directions. This is given by the temperature at which the MAE becomes equal to the thermal energy.

The Fe_{13} cluster has a large energy gap of 0.2 eV, therefore temperature changes which are small compared to this gap will not change the occupation of states or the anisotropy. The $Fe_{10}Co_3$ cluster, however, showed a surprisingly high moment reorientation temperature of 480 K. However, this result was obtained only by varying the temperature for the spin–orbit coupling. A change in temperature for a metallic system also changes the SCF wave functions and energies. Therefore, we carried out SCF calculations at the same electronic temperature as used in the spin–orbit part, allowing for full electronic relaxation at that broadening temperature. The results are also shown in Fig. 2. The SCF anisotropy curve is now shifted downwards, resulting in a reorientation temperature of about 400 K.

Degeneracies at the Fermi level indicate possible Jahn–Teller relaxations, therefore we allowed for geometry relaxation by lowering symmetry constraints. First, we restricted the movement of the three central atoms along the z axis, all other outer atoms were symmetry unconstrained. The degeneracies at the Fermi level vanish and all clusters gain Jahn–Teller energy. Relaxing the symmetry has a dramatic effect on MAE, which decreases significantly. Removing all constraints, the largest change is found for the case of $Fe_{10}Co_3$. The axial arrangement of the Co atoms is lost and the MAE decreases significantly. Fe_{13} does not show any great changes in geometry or MAE as expected. Results for the MAE are given in Table II.

It is interesting to compare the aforementioned results with the bulk. Fe_xCo_{1-x} alloys exhibit the highest magnetization at a Co concentration of around 30% and are associated with an increase in the local moment on Fe sites from a bulk value of 2.2 μ_B/atom to almost 2.8 μ_B/atom (Ref. 20) for Fe sites surrounding Co. In clusters, the Fe sites in Fe_{13} already have a moment of 3.38 μ_B/atom and the addition of Co does not lead to any enhancement of the magnetic moment. However, the introduction of chemical ordering via three Fe atoms in $Co_{10}Fe_3$ and by three Co atoms in $Fe_{10}Co_3$ does increase the anisotropy compared to pure clusters when the atoms are constrained along the z axis. Similar behavior is also observed in five-atom clusters.

To summarize, the present studies show that the small Fe_n and Fe_nCo_m clusters exhibit high magnetic moments per atom that are about 35% higher than the Slater–Pauling limit. However, the clusters have small magnetic anisotropy energies indicating that bulk magnetic alloys can be made softer by going to nanosizes. What is most surprising is that whereas bulk Co has a higher anisotropy than pure Fe or mixed Fe–Co alloys, Co_n clusters have the lowest anisotropy. The present work also shows that a high magnetic anisotropy requires a strong coupling between occupied and unoccupied states close to the Fermi energy. One possible way to accomplish this may be to generate unreactive, compositionally ordered uniaxial clusters with small gaps.

Two of the authors (S.N.K. and C.A.) are thankful to DOE (DE-FG02-96ER45579) for support. Two other authors (M.R.P. and J.K.) were supported in part by the ONR Molecular Design Institute (Grant Nos. N0001400AAF00002 and N00014-98-WX20709).

[1] J. P. Chen, C. M. Sorensen, K. J. Klabunde, and G. C. Hadjipanayis, Phys. Rev. B **51**, 11527 (1995); and references therein.
[2] A. J. Cox, J. G. Louderback, and L. A. Bloomfield, Phys. Rev. Lett. **71**, 923 (1993).
[3] C. A. Baumann, R. J. Van Zee, S. Bhat, W. Weltner, Jr., J. Chem. Phys. **78**, 190 (1983).
[4] M. R. Pederson, F. Reuse, and S. N. Khanna, Phys. Rev. B **58**, 5632 (1998).
[5] C. P. Bean and J. D. Livingston, J. Appl. Phys. **30**, 120S (1959).
[6] S. N. Khanna and S. Linderoth, Phys. Rev. Lett. **67**, 742 (1991).
[7] J. A. Becker, R. Schäfer, R. Festag, W. Ruland, J. H. Wendorff, J. Pebler, S. A. Quaiser, W. Helbig, and M. T. Reetz, J. Chem. Phys. **103**, 2520 (1995).
[8] I. M. L. Billas, A. Chatelain, and W. A. de Heer, Science **265**, 1682 (1994).
[9] D. C. Douglass, J. P. Bucher, and L. A. Bloomfield, Phys. Rev. Lett. **66**, 3052 (1991).
[10] G. M. Pastor, J. Dorantes-Dávila, S. Pick, and H. Dreysse, Phys. Rev. Lett. **75**, 326 (1995).
[11] L. Zhou, D. Wang, and Y. Kawazoe, Phys. Rev. B **60**, 9545 (1999).
[12] M. R. Pederson and K. A. Jackson, Phys. Rev. B **41**, 7453 (1990); K. A. Jackson and M. R. Pederson, *ibid.* **42**, 3276 (1990).
[13] J. P. Perdew, K. Burke, and M. Ernzerhof, Phys. Rev. Lett. **77**, 3865 (1996).
[14] D. V. Porezag and M. R. Pederson, Phys. Rev. A **60**, 2840 (1999).
[15] M. R. Pederson and S. N. Khanna, Phys. Rev. B **60**, 9566 (1999); Chem. Phys. Lett. **307**, 253 (1999).
[16] H. J. Fan, C. W. Liu, and M. S. Liao, Chem. Phys. Lett. **273**, 353 (1997).
[17] M. Castro, C. Jamorski, and D. R. Salahub, Chem. Phys. Lett. **271**, 133 (1997).
[18] A. V. Postnikov, P. Entel, and J. M. Soler (unpublished).
[19] D. Hobbs, G. Kresse, and J. Hafner, Phys. Rev. B **62**, 11556 (2000).
[20] J. M. Maclaren, T. C. Schulthess, W. H. Butler, R. Sutton, and M. McHenry, J. Appl. Phys. **85**, 4833 (1999).

Appendix J

Kortus J., Hellberg C. S., Pederson M. R. and Khanna S. N.

DFT studies of the molecular nanomagnet Fe_8 and the V_{15} spin system

Eur. Phys. J. D **16**, 177-180 (2001)

Eur. Phys. J. D **16**, 177–180 (2001)

THE EUROPEAN PHYSICAL JOURNAL D

EDP Sciences

DFT studies of the molecular nanomagnet Fe_8 and the V_{15} spin system

Electronic structure and magnetic ordering

J. Kortus[1,a], M.R. Pederson[1], C.S. Hellberg[1], and S.N. Khanna[2]

[1] Center for Computational Materials Science, Naval Research Laboratory, Washington DC 20375-5000, USA
[2] Department of Physics, Virginia Commonwealth University, Richmond, VA 23284-2000, USA

Received 30 October 2000

Abstract. Based on first-principles all-electron density-functional calculations we report the electronic structure and magnetic ordering of the molecular magnet Fe_8 and the V_{15} spin system. The ferrimagnetic ordering with total spin $S = 10$ of the eight iron atoms in the Fe_8 cluster agrees well with experimental results from polarized neutron data. In comparison the low spin system V_{15} shows a spin $S = 1/2$ ground state which is also found from our calculations.

PACS. 75.50.Xx Molecular magnets – 71.24.+q Electronic structure of clusters and nanoparticles

1 Introduction

Molecular magnets such as Mn12-ac and Fe_8 are a new class of materials that have raised significant scientific interest due to the observation of quantum tunneling of magnetization and hysteresis of a purely molecular origin [1,2]. These big molecular clusters form crystals of identical nanomagnets, whose structure can be well characterized by X-diffraction measurement. Because nearly all molecules in the crystal have the same orientation, macroscopic measurement can directly observe single molecular properties and quantum phenomena. The high value of the ground state spin of $S = 10$ for Mn12-ac and Fe_8 makes these clusters also interesting for possible applications in nanoscale magnetic devices. In order to build any device it is necessary to understand the strong interactions of the metal ions, such as spin-spatial couplings and spin-spin exchange effects. Further, the ligands and other non-magnetic atoms are very important in stabilizing the spin configurations. In order to account for the strong ligand-metal interactions and to determine the electronic and magnetic structure of a given system, first-principles methods allowing for electronic, charge and structural relaxations are needed. The knowledge gained from these calculations can be very helpful for understanding and improving the systems.

One of the experimentally best studied clusters is the Fe_8-cluster with the formula $[Fe_8O_2(OH)_{12}(tacn)_6]^{8+}$, with tacn = $C_6N_3H_{15}$. The cluster is particularly interesting because its magnetic relaxation becomes temperature independent below 0.36 K, showing for the first time a pure tunneling of the magnetization [3].

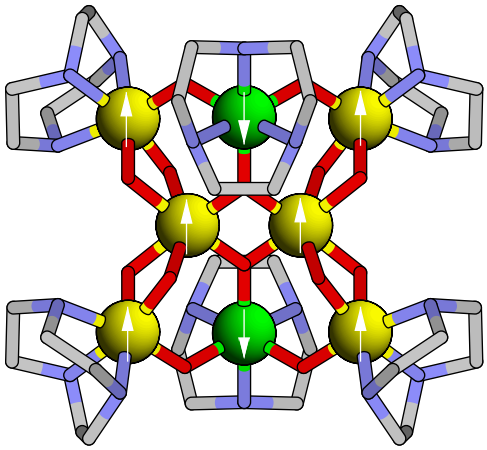

Fig. 1. The optimized geometry of the Fe_8 cluster. The balls show the iron atoms, the arrows represent the ferrimagnetic spin ordering in the cluster. The organic tacn-rings are very important for stabilizing the magnetic core of the molecule and in separating the Fe_8-clusters in the crystal. The hydrogens are not shown for clarity.

The structure of the Fe_8-cluster is shown in Fig. 1. The cluster found in molecular crystals has D_2 symmetry. The central iron atoms are connected by hydroxo bridges to the four outer iron ions. The spheres show the iron atoms, which are Fe(III) ions with a d^5 electron configuration. The ferrimagnetic coupling of spins between the eight Fe atoms results in a $S = 10$ spin ground state [4]

[a] e-mail: kortus@dave.nrl.navy.mil

and is illustrated by arrows inside the spheres. The organic tacn-rings are very important for stabilizing the magnetic core of the molecule by accepting charge, thus allowing the correct charge state of the Fe^{3+} ions. Additionally, the tacn-rings separate the Fe_8-clusters in the crystal, resulting in typical intermolecular dipole fields of the order of 0.05 T [5].

The V_{15} compound is a low spin compound with $S = 1/2$. The weakly anisotropic V_{15} demonstrates quantum behavior, such as tunneling splitting of low lying spin states and is an attractive model system for the study of mesoscopic quantum coherence and processes which destroy it. Understanding such processes is of interest to the field of quantum computing.

V_{15} has a crystallographically imposed trigonal symmetry with three sets of inequivalent vanadium atoms [6]. The unit cell contains two V_{15} clusters and is large enough that dipolar interactions between the molecules are negligible. Between 20 K and 100 K the effective paramagnetic moment is $3\mu_B$ corresponding to three independent spins and below 0.5 K it decreases showing an $S = 1/2$ ground state for the V_{15} molecule. The experimental results were interpreted with antiferromagnetic interactions between all vanadium atoms [6].

The large number of atoms in Fe_8 and V_{15} still makes first-principles calculations a challenge, and we are not aware of any other electronic structure calculations for these clusters. In this paper we present first-principles gradient corrected density-functional calculations at the all-electron level for all atoms for both the Fe_8- and the V_{15}-cluster. We report on the electronic structure and magnetic ordering for these systems.

2 Computational details

The DFT calculations [7] discussed herein were performed with the all-electron Gaussian-orbital-based NRLMOL program [8]. All calculations employed the Perdew-Burke-Ernzerhof (PBE) generalized-gradient approximation for the density-functional [9]. NRLMOL combines large Gaussian orbital basis sets, numerically precise variational integration and an analytic solution of Poisson's equation in order to accurately determine the self-consistent potentials, secular matrix, total energies and Hellmann-Feynman-Pulay forces [10]. The exponents for the single Gaussian have been fully optimized for DFT calculations [11].

2.1 Fe_8 molecular nanomagnet

Using X-ray data deposited at the Cambridge Crystallographic Data Centre [12] we generated the Fe_8 cluster.

For each Fe we used 7 s-like, 3 p-like and 2 d-like contracted Gaussian orbitals with 19 exponents between 0.12 and 3.87×10^6. Fluorine was described by 5 s- and 4 p-contracted orbitals using 14 bare Gaussian between 0.118 and 1.23×10^5. Oxygen had 3 s- and 2 p-contracted orbitals with 13 Gaussian between 0.105 and 6.12×10^4, nitrogen had the same number of contracted orbitals and bare Gaussian ranging from 0.12 to 5.17×10^4. Carbon had also basis of 3 s- and 2 p-orbitals with 12 exponents between 0.1 and 2.22×10^4, finally hydrogen had 2 s- and 1 p-orbital with 6 exponents between 0.1 and 77.84. This basis set resulted in a total number of 1466 contracted orbitals for the whole cluster.

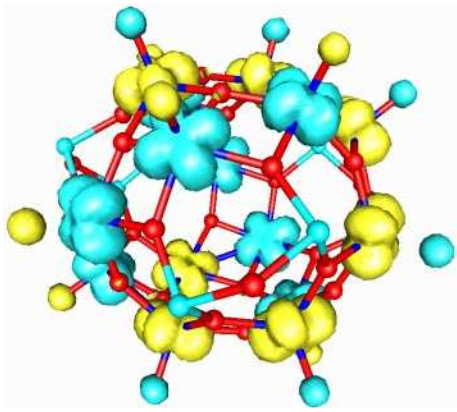

Fig. 2. The spin density of the V_{15} cluster. The picture shows clearly the single d-electron of a V^{4+} ion. Most of the spin density is localized at the V, less than 1% of the spin density is on the oxygen atoms which are on top of the V. The dark balls represent oxygen and the lighter ones arsenic.

2.2 V_{15} spin system

Starting from X-ray data[13] we generated several unit cells and isolated from that a single $K_6[V_{15}As_6O_{42}(H_2O)]$ unit. The structure of V_{15} is shown in Fig. 2. The vanadium atoms are at the place of the shown d-like orbitals, the oxygen atoms are small dark balls and the arsenic atoms are represented by lighter small balls. The potassiums included in the calculation are not shown. The three sets of the vanadium atoms define two hexagons separated by a triangle of vanadiums. Due to the layered structure the V_{15} cluster is expected to show interesting magnetic properties.

In order to use the D_3 symmetry of the V_{15} molecule [14] we initially replaced the statistically oriented water molecule in the center of the molecule by the noble gas neon. Subsequent calculations show that the electronic and magnetic properties of this system are unaffected by the presence or type of inert moiety enclosed within the void.

The basis set for vanadium consists of 20 bare Gaussian ranging from 3.108×10^6 to 0.03783 contracted to 9 s-, 4 p- and 3 d-molecular orbitals, for oxygen we used 13 bare Gaussian between 6.121×10^4 and 0.1049 contracted to 5 s-like, 3 p- and 1 d-molecular orbitals. The arsenic atoms were described by 21 bare Gaussian between 6.9614505×10^6 and 0.0607459 contracted to 10 s-, 5 p- and 4 d-like orbitals. This gives a total of 1853 contracted orbitals used as basis set for the calculations.

In conjunction with the conjugate-gradient algorithm the Hellmann-Feynman-Pulay forces were used in order

to optimize the molecular geometry. The process was stopped after the largest nuclear gradient was smaller than 0.2 eV/Å. The total force was 0.28 eV/Å.

3 Results and discussion

3.1 Fe_8 molecular nanomagnet

In the molecular crystal [12] the positive charged Fe_8-cluster is neutralized with Br atoms. We started the calculations with Br atoms but run in problems with an incomplete charge transfer to the Br. A density of states plot revealed a strong peak of Br p-states at the Fermi level. This unchemical hybridization of the Br with the Fe_8-cluster due to energetically to high lying Br p-states can be attributed to problems with density-functional theory itself, requiring self-interaction corrections or LDA+U methods in order to account for. Another source of the problem could be the neglected water molecules in our calculations, which are present in the crystal. Calculations on a single Br-ion surrounded by water molecules showed a lowering of the Br p-states, therefore allowing for better charge transfer. The incomplete charge transfer results in a metallic density of states at the Fermi-level, which complicates the self-consistent calculations and geometry optimization of the cluster.

Even more problematic is a competition between the experimental seen ferrimagnetic state with an energetically close ferromagnetic state with also $S = 10$. Using Br atoms we could stabilize the ferrimagnetic state only by applying a small external potential on the Fe atoms favoring the ferrimagnetic state.

Due to these reasons we replaced the Br with F atoms, which are more electro-negative allowing for better charge transfer. With the F atoms the calculations converged to the experimental found ferrimagnetic state with $S = 10$ [4] without an external potential.

More recent experiments by Pontillon *et al.* [15] confirm the ferrimagnetic ordering and find smaller local moments at the two iron atoms with the minority spins than on the iron atoms with majority spins.

In order to calculate the local moments, we placed a sphere of 1.32 Å around each iron and calculated the spin density inside the sphere. Some charge will not be included in the sphere, and this approximation will give only a lower estimate for the local moments and charge states.

For the two iron atoms with minority spins we obtain a moment of $-3.6\mu_B$, whereas the majority spin irons have moments $3.8\mu_B$ and $3.9\mu_B$. These local moments are smaller than expected for Fe(III) which can be attributed to spin density outside the sphere. A plot of the spin density confirms the right spin-polarization of the irons by showing a spherical spin density around the Fe as expected for a closed shell d^5 electron configuration.

3.2 V_{15} spin system

The plot of the spin density in Fig. 2 clearly shows the localization of moment on the vanadium atoms. Even more, it clearly displays the d-character as expected for a V^{4+}-ion with a single d-electron, showing that our calculation reproduce the proper charge state of the vanadiums. The spin configuration shown in Fig. 2 has a total spin $S = 1/2$ and is also the lowest energy DFT spin configuration. This spin configuration was found by a coupled multilevel analysis which relies on fitting density-functional energies to mean-field Heisenberg energies [16].

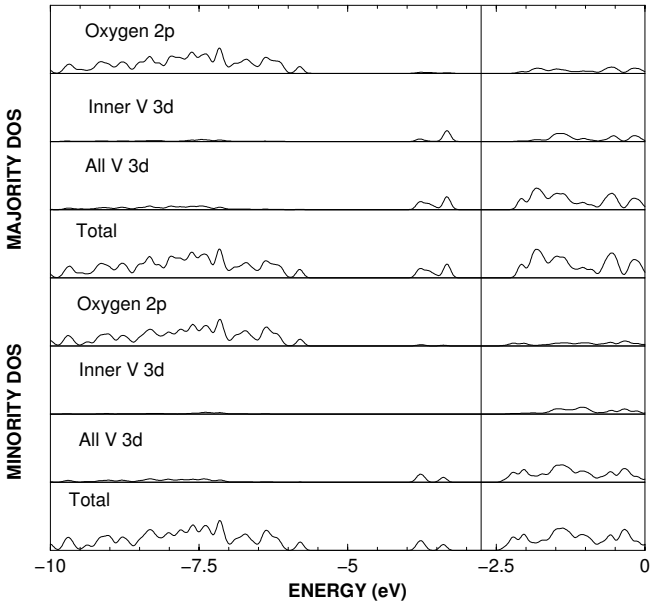

Fig. 3. Electronic density of states (DOS) broadened by 0.54 eV of V_{15} in a spin $S = 3/2$ configuration. For each spin the total DOS, the projected DOS of all V($3d$), the projected DOS of the three V($3d$) forming the inner triangle and the projected O($2p$) are presented. The vertical line divides the occupied and unoccupied states. Units are arbitrary, but the same scale has been used for all projected DOS plots.

The quantum mechanical ground state will be a superposition of all $S = 1/2$ states, therefore the obtained spin configuration from our DFT calculations can not be compared directly with experiment. Nevertheless, our results are essentially in agreement with the experimentally found $S = 1/2$ ground state [17] of the V_{15} cluster.

Figure 3 displays the density of states for a spin $S = 3/2$ configuration with ferromagnetically aligned spins in the inner triangle and antiferromagnetically coupled spins in top and bottom hexagons. This low-energy spin configuration becomes important at temperatures above 20 K and below 80 K.

For each spin the DOS is decomposed into the $3d$ contributions of all vanadium atoms (All V $3d$) and the $2p$ contributions of oxygen (Oxygen $2p$). The vanadium DOS is further decomposed into the $3d$ contribution of the vanadiums (Inner V $3d$) forming the inner triangle between the two hexagons. The projected density of states clearly shows that the states near the Fermi level are $3d$ states from the vanadium atoms.

Further, by comparing the majority and minority contributions of the vanadiums forming the inner triangle, it

Table 1. Highest occupied molecular orbital (HOMO), lowest unoccupied molecular orbital (LUMO) and spin gaps Δ for the V_{15} molecule in the spin $S = 3/2$ state. All energies are given in eV.

	HOMO	LUMO	Δ
Majority spin	−3.369	−2.159	1.210
Minority spin	−3.440	−2.412	1.082

is clear that these three vanadiums are aligned ferromagnetically since they only contribute to the majority DOS.

Further, most of the DOS in the majority DOS comes from these atoms. The states due to the V atoms at the Fermi level are well localized and do not show hybridization with other atoms such as oxygen. This indicates mainly ionic bonding, which is supported by our local moments for the vanadium atoms of $0.97\mu_B$, close to the moment of a V^{IV} ion. The DOS for the arsenic atoms is not shown, because there are no significant contributions.

In Table 1 we present the highest occupied molecular orbital (HOMO) and lowest unoccupied molecular orbital (LUMO) for the majority and minority spin channel together with the resulting spin gaps.

In order to estimate local moments we placed spheres around the atoms and calculated the spin densities inside the spheres. The only significant moments are located on the vanadium atoms, the largest other moments are at oxygen atoms with about $0.06\mu_B$. The sphere radius for the vanadium atoms was 1.32 Å. The vanadium atoms forming the two hexagons are coupled antiferromagnetically with local moments of $-0.88\mu_B$ and $0.85\mu_B$ inside the sphere. The vanadium atoms forming the middle triangle are ferromagnetically ordered with a local moment of $0.97\mu_B$. This result agrees well with the measurements above 20 K, that the spins in the triangle are localized spins on the vanadiums acting independently.

For the $S = 1/2$ spin configuration displayed in Fig. 2, the moments in the spheres do not change not significantly. They are less than 4% smaller than for the $S = 3/2$ configuration.

4 Conclusion

We performed first-principles gradient corrected density-functional calculation at the all-electron level on the experimentally interesting molecular nanomagnet Fe_8 and the spin system V_{15}. The magnetic ordering obtained from our calculations agrees well with experimental found magnetic orderings in these clusters. The local moments found for the Fe_8-cluster confirms recent experimental findings from polarized neutron scattering. In case of V_{15} we are able to describe different spin configurations. Our findings are in good agreement with experiments.

Electronic structure calculations can give insight in the magnetic interaction and help in understanding experiment. The information obtained here can be used directly for interpretation of polarized neutron scattering experiments and finding the charge state of the metal ions. Much more experimental relevant information has been obtained from our calculations as magnetic anisotropy energies, orbital moments, Heisenberg exchange parameters, hyperfine fields and vibrational properties. These will be reported elsewhere.

This work was supported in part by ONR grant N00014-98WX20709 and N0001400AF00002. Computations were performed at the DoD Major Shared Resource Centers.

References

1. J. Friedman, M.P. Sarachik, J. Tejeda, J. Maciejewski, R. Ziolo, Phys. Rev. Lett. **76**, 3820 (1996); L. Thomas, F. Lionti, R. Ballou, D. Gatteschi, R. Sessoli, B. Barbara, Nature **383**, 145 (1996).
2. C. Sangregorio, T. Ohm, C. Paulsen, R. Sessoli, D. Gatteschi, Phys. Rev. Lett. **78**, 4645 (1997).
3. W. Wernsdorfer, R. Sessoli, Science **284**, 133 (1999).
4. R. Caciuffo, G. Amoretti, A. Murani, R. Sessoli, A. Caneschi, D. Gatteschi, Phys. Rev. Lett. **81**, 4744 (1998).
5. W. Wernsdorfer, T. Ohm, C. Sangregorio, R. Sessoli, D. Mailly, C. Paulsen, Phys. Rev. Lett. **82**, 3903 (1999).
6. D. Gatteschi, L. Pardi, A.L. Barra, A. Müller, J. Döring, Nature **354**, 463 (1991).
7. P. Hohenberg, W. Kohn, Phys. Rev. **136**, B864 (1964); W. Kohn, L.J. Sham, Phys. Rev. **140**, A1133 (1965).
8. M.R. Pederson, K.A. Jackson, Phys. Rev. B **41**, 7453 (1990); K.A. Jackson, M.R. Pederson, Phys. Rev. B **42**, 3276 (1990).
9. J.P. Perdew, K. Burke, M. Ernzerhof, Phys. Rev. Lett. **77**, 3865 (1996).
10. H. Hellmann, *Einführung in die Quantentheorie* (Deuticke, Leipzig, 1937); R.P. Feynman, Phys. Rev. **56**, 340 (1939); P. Pulay, Mol. Phys. **17**, 197 (1969).
11. D. Porezag, M.R. Pederson, Phys. Rev. A **60**, 2840 (1999).
12. K. Wieghardt, K. Pohl, I. Jibril, G. Huttner Angew. Chem., Int. Ed. Engl. **23**, 77 (1984); Cambridge Crystallographic Data Centre; Refcode: COCNAJ; `http://www.ccdc.cam.ac.uk/`
13. A. Müller, J. Döring, Z. Anorg. Allg. Chem. **595**, 251 (1991).
14. A. Müller, J. Döring, Angew. Chem. Int. Ed. **27**, 1721 (1988).
15. Y. Pontillon, A. Caneschi, D. Gatteschi, R. Sessoli, E. Ressouche, J. Schweizer, E. Lelievre-Berna, J. Am. Chem. Soc. **121**, 5342 (1999).
16. J. Kortus, C.S. Hellberg, M.R. Pederson, Phys. Rev. Lett. **86**, 3400 (2001).
17. I. Chiorescu, W. Wernsdorfer, A. Müller, H. Bögge, B. Barbara, Phys. Rev. Lett. **84**, 3454 (2000).

Appendix K

Kortus J., Baruah T., Bernstein N., and Pederson M.R.

Magnetic ordering, electronic structure and magnetic anisotropy energy in the high-spin Mn_{10} single molecule magnet

Phys. Rev. B **66**, 092403-1/4 (2002)

Magnetic ordering, electronic structure, and magnetic anisotropy energy in the high-spin Mn_{10} single molecule magnet

Jens Kortus*
Max-Planck-Institut für Festkörperforschung, Heisenbergstrasse 1, D-70569 Stuttgart, Germany

Tunna Baruah, Noam Bernstein, and Mark R. Pederson
Center for Computational Materials Science, Naval Research Laboratory, Washington, DC 20375-5000
(Received 22 April 2002; published 16 September 2002)

We report the electronic structure and magnetic ordering of the single molecule magnet $[Mn_{10}O_4(2,2'\text{-biphenoxide})_4Br_{12}]^{4-}$ based on first-principles all-electron density-functional calculations. We find that two of the ten core Mn atoms are coupled antiferromagnetically to the remaining eight, resulting in a ferrimagnetic ground state with total spin $S=13$. The calculated magnetic anisotropy barrier is found to be 9 K in good agreement with experiment. The presence of the Br anions impacts the electronic structure and therefore the magnetic properties of the ten Mn atoms. However, the electric field due to the negative charges has no significant effect on the magnetic anisotropy.

DOI: 10.1103/PhysRevB.66.092403 PACS number(s): 75.50.Xx, 71.15.Mb, 75.30.Gw

The interest in magnetic molecular clusters of transition-metal ions has been continuously growing since the observation of magnetic bistability of a purely molecular origin in the so-called Mn_{12}-ac,[1] which shows a magnetic hysteresis cycle below 4 K similar to that observed for bulk magnetic materials. The magnetic bistability associated with the hysteresis cycle has created an interest in these clusters for information storage, although at low temperature quantum effects affect the reversal of the magnetization, resulting in steps in the hysteresis.[2] This phenomenon of quantum tunneling of magnetization is governed by the magnetic anisotropy energy (MAE)[3] barrier which is due to directional dependencies of the second-order spin-orbit-coupling energy.

Recently, Pederson and Khanna have developed a method for accounting for second-order anisotropy energies.[4] This method relies on an exact and simple expression for the spin-orbit coupling operator used in a second-order perturbative treatment to determine the dependence of the total energy on spin projection. Initial applications to the uniaxial Mn_{12}-ac lead to a density-functional-based second-order anisotropy energy[5] of 55.7 K, in agreement with the experimentally deduced values[6,7] of 54.8(3) or 55.6 K.

Because the second-order anisotropy energy scales with the square of the magnetization it was generally believed that a high-spin ground state S would be beneficial for a large barrier. The $[Mn_{10}O_4(2,2'\text{-biphenoxide})_4Br_{12}]^{4-}$ cluster has been reported to have a $S=12$ high-spin ground state[8] but only a small energy barrier of about 7.7 K. In this work we investigate the electronic and magnetic properties and the magnetic anisotropy energy of this high-spin single molecule magnet. The information obtained here may be useful in the search for single molecule magnets with a greater magnetic anisotropy.

Figure 1 shows the structure of the $[Mn_{10}O_4(2,2'\text{-biphenoxide})_4Br_{12}]^{4-}$ molecular magnet. The 10 Mn atoms form a tetrahedronlike structure with Mn atoms at the corners and at the middle of the tetrahedron edges. Two of the Mn atoms, the top and the bottom spheres in Fig. 1, are coupled antiferromagnetically to the rest of the Mn atoms. The Mn atoms are bridged by O atoms. The magnetic core is further stabilized by organic rings that are also connected to the O atoms. The negatively charged cluster is compensated by $[(CH_3CH_2)_3NH]_2[Mn(CH_3CN)_4(H_2O)_2]$ in the molecular crystal, but experimental results suggest that the magnetic anisotropy is due to the localized valences of the 10 Mn atoms.[8] In order to use the higher symmetry and make the problem computationally feasible, we carried out our calculation on the negatively charged $[Mn_{10}O_4(2,2'\text{-biphenoxide})_4Br_{12}]^{4-}$ cluster which contains 114 atoms. The eight symmetry operations reduce the complete cluster to 18 inequivalent atoms.

Our density functional-based calculations[9,10] were per-

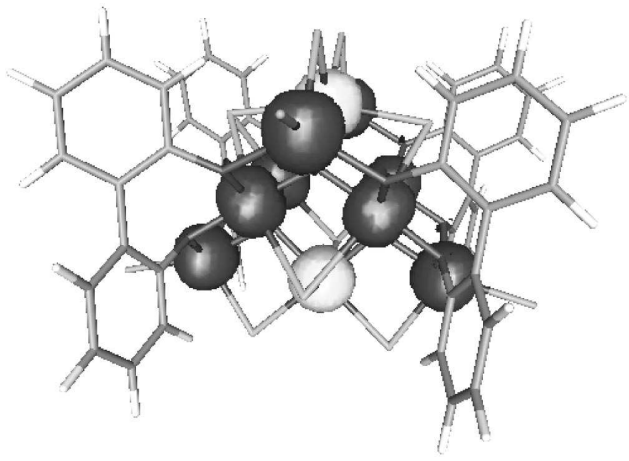

FIG. 1. The tetrahedronlike structure of the ten Mn atoms and the surrounding organic rings. The Br atoms are not displayed for clarity. Density isosurfaces for $0.03e/a_B^3$ for majority (dark) and minority (light) spins on Mn atoms are shown. The plot clearly shows that the magnetic moment is localized at the Mn atoms, and it directly confirms the antiferromagnetic coupling of two Mn atoms (large light spheres) to the remaining Mn atoms (large dark spheres).

TABLE I. The Gaussian basis set used for the calculation. The minimum and maximum exponent α of the bare Gaussians, the number of bare Gaussians, the number of contracted *s*-, *p*-, and *d*-like basis functions.

	$\alpha_{\min}$	$\alpha_{\max}$	N_{bare}	*s*	*p*	*d*
Br	0.0781	7.9×10^6	21	11	6	4
Mn	0.0416	3.6×10^6	20	11	5	4
O	0.1049	6.1×10^4	13	8	4	3
C	0.0772	2.2×10^4	12	8	4	3
H	0.0745	77.84	6	5	3	1

formed with the Naval Research Laboratory Molecular Orbital Library (NRLMOL) program,[11–16] using the Perdew-Burke-Ernzerhof (PBE) generalized-gradient approximation for the exchange and correlation functional[17]. The molecular orbitals were expanded as linear combinations of Gaussian functions centered at the atomic sites. The calculations were carried out at the all-electron level and the multicenter integrals required in the solution of the Kohn-Sham equation were calculated by integrating numerically over a mesh of points.[11] NRLMOL combines large Gaussian orbital basis sets, numerically precise variational integration and an analytic solution of Poisson's equation to accurately determine the self-consistent potentials, secular matrix, total energies, and Hellmann-Feynman-Pulay forces. The exponents for the single Gaussian have been fully optimized for density functional theory calculations.[15] The basis set for the Mn_{10} cluster consisted of a total of 3756 contracted orbitals. The minimum and maximum exponent of the bare Gaussians, the number of bare Gaussians, and the number of contracted *s*-, *p*-, and *d*-like basis functions are given in Table I for each atomic species. The contraction coefficients for atomic orbitals were obtained by performing an SCF-LDA calculation on the spherical unpolarized atom where the total energy of the atom was converged to within 10 meV. The basis functions that do not correspond to atomic wave function were constructed from the longest range bare Gaussians in the basis set.

Here we repeat some of the formulas needed for discussion of the magnetic anisotropy energy. The same definitions and notation are used as in Ref. 4. In the absence of a magnetic field the second-order MAE Δ_2 resulting from the spin-orbit coupling, for an arbitrary symmetry, reduces to

$$\Delta_2 = \sum_{\sigma\sigma'} \sum_{ij} M_{ij}^{\sigma\sigma'} S_i^{\sigma\sigma'} S_j^{\sigma'\sigma}, \tag{1}$$

which is a generalization of Eq. (19) of Ref. 4. The matrix elements $S_i^{\sigma\sigma'} = \langle \chi^\sigma | S_i | \chi^{\sigma'} \rangle$ implicitly depend on two angles (θ,β) defining the axis of quantization. The matrix elements $M_{ij}^{\sigma\sigma'}$, which are related to the induced orbital moment, are given by

$$M_{ij}^{\sigma\sigma'} = -\sum_{kl} \frac{\langle \phi_{l\sigma} | V_i | \phi_{k\sigma'} \rangle \langle \phi_{k\sigma'} | V_j | \phi_{l\sigma} \rangle}{\varepsilon_{l\sigma} - \varepsilon_{k\sigma'}}, \tag{2}$$

where $\phi_{l\sigma}$, $\phi_{k\sigma}$, and $\varepsilon_{l\sigma}$ are, respectively, the occupied, unoccupied and the corresponding energies of states. V_i is same as defined in Eq. (7) of Ref. 4 and is related to derivatives of the Coulomb potential. The matrix elements can be evaluated by integrating products of the Coulomb potential with partial derivatives of the basis functions. This procedure avoids the time consuming task of calculating the gradient of the Coulomb potential directly.

In addition to the magnetically interesting complex, the crystal also contains single Mn complexes to balance the charges. Using high-field EPR spectroscopy Barra *et al.*[8] found that this $[(CH_3CH_2)_3NH]_2[Mn(CH_3CN)_4(H_2O)_2]$ unit is paramagnetic. We also find that this unit is paramagnetic, with the Mn atom in a $+2$ charge state and a spin of $S=5/2$. The complex exhibits easy-plane behavior with an energy well of 0.1 K. We therefore focus the remainder of our work on the Mn_{10} unit only.

Calculations on a $S=12$ high spin state revealed that this spin state would not be magnetically stable because there would be no common Fermi level in the majority and minority spin channel. The Fermi level misalignment indicated further transport of electrons of the minority to the majority spin channel. As a result we obtained a $S=13$ high spin state as the magnetic ground state instead of the $S=12$ state obtained from high-field EPR spectroscopy. Our result is consistent with experiment since it is difficult to differentiate experimentally between the two possibilities.[18]

A plot of the spin density shown in Fig. 1 clearly confirms the antiferromagnetic coupling of two of the Mn atoms to the remaining Mn atoms. The spin density around the minority spin Mn and the four majority spin Mn at the corners of the tetrahedronlike magnetic core show a nearly spherical spin density as expected for a closed d^5 shell. The other four Mn atoms which are on the edges of the tetrahedron (large dark spheres) show a less spherical spin density, indicating another charge state for these atoms. In order to analyze the magnetic ordering we calculated the spin density in spheres around the atoms. This gives a measure of the localized moment at the atom, but will generally underestimate the exact value. Using spheres with a radius of $2.23a_B$ around the Mn atoms we obtained for the three non-equivalent Mn atoms (majority spin tetrahedron edge, majority spin tetrahedron vertex, and minority spin tetrahedron edge) a local moment of 3.6, 4.3, and $-4.3\mu_B$, respectively. This result suggests an ionic picture that the first Mn has an Mn^{3+} $(S=2)$ state, whereas the other two are Mn^{2+} $(S=5/2)$. This picture is fully in accord with the spin density plot in Fig. 1. Due to the symmetry of the cluster, the two types of majority spin Mn atoms have a multiplicity of 4 whereas the minority spin Mn atom has a multiplicity of 2, resulting in the previously mentioned $S=4\times2+4\times5/2-2\times5/2=13$ magnetic ground state.

The electronic density of states (DOS) for the majority and minority spin channels is shown in Fig. 2. For each spin, the DOS is further decomposed into the $3d$ contributions of all Mn atoms. It is evident from the plot that the states around the Fermi level are clearly connected with $3d$ states of the Mn atoms. This result also agrees well with the experimental picture that the states near the Fermi level are

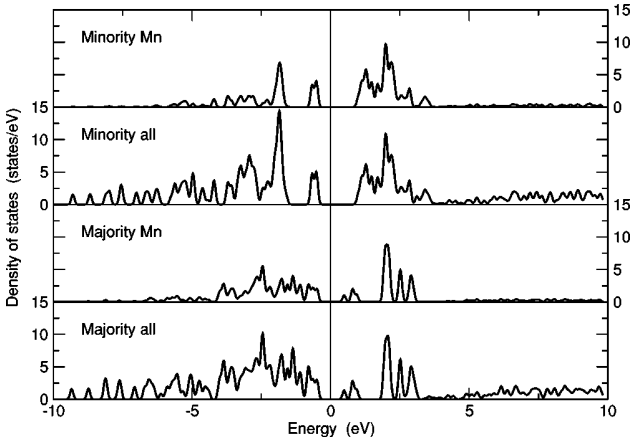

FIG. 2. Electronic density of states (DOS) broadened by 0.54 eV of Mn_{10} in the spin $S=13$ configuration. For each spin the total DOS and the projected DOS of all Mn($3d$) are presented. The vertical line indicates the Fermi level.

well localized and do not show strong hybridization with other atoms, although we find some O, Br, and N contributions for the occupied states.

Starting from the experimental geometry[18] we carried out about 30 steps of a conjugate-gradient algorithm using the Hellmann-Feynman-Pulay forces for optimization of the geometry. For each new geometry we calculated the complete Hamiltonian of the magnetic anisotropy and the second-order contribution to magnetic anisotropy barrier DS_z^2. In accord with experimental data, we find that the Mn_{10} single molecule magnet is an easy-axis system. The barrier showed no strong dependence on geometry varying between 8.8 and 10.4 K with a value of 9.5 K for the lowest energy geometry. Expressing the barrier in the form of a simple spin Hamiltonian $H=DS_z^2$ we obtained a value of $D=-0.056$ K. For the calculation of the spin orbit matrix elements, we included all valence electrons and all unoccupied states in an energy window of 13.6 eV above the highest occupied state. The difference between the second-order treatment and exact diagonalization of the Hamiltonian including the spin-orbit matrix elements, which also includes some higher order effects, was of the order of 0.1 K. This error is also an estimate of the numerical accuracy of our calculation, indicating that changes due to structural effects are much more significant.

Equation 2 shows that the barrier is related to matrix elements between occupied and unoccupied orbitals in the majority and minority spin channels. In order to give a deeper insight into which states are forming the barrier, we analyze these contributions in more detail. First, we focus on the contributions of the different spin channels. Table II summarizes the result in form of the D parameter allowing only a given spin channel, for example including only matrix elements $M_{ij}^{\sigma\sigma'}$ between occupied majority states and unoccupied minority states, in the calculation of the barrier. All matrix elements from the occupied majority electrons prefer an easy-axis system, whereas the matrix elements from the occupied minority spin channel would result in an easy-plane system. Only due to the larger values of the contributions of

TABLE II. The contributions of the different spin channels [see Eq. (2)] to the magnetic anisotropy parameter D and the magnetic anisotropy energy DS_z^2.

occupied	unoccupied	D (K)	DS_z^2 (K)
majority	majority	−0.039	−6.6
majority	minority	−0.106	−17.9
minority	majority	0.034	5.7
minority	minority	0.055	9.3

the occupied majority spin channel the system ends up as an easy-axis system. This partial cancellation between the different spin channels seems to be the reason for the small barrier as compared with Mn_{12}, where we observed constructive contributions to the barrier from all spin channels.

In addition to the spin channel contribution, we can analyze which electronic states contribute most to the matrix elements $M_{ij}^{\sigma\sigma'}$. In Fig. 3 we display plots of the square of the wavefunctions of the occupied majority state and the unoccupied minority state that contribute to the matrix element $M_{ij}^{\sigma\sigma'}$ with the largest absolute value. It is clearly visible that the states of interest are d states localized at the same Mn atom. In this case, the states are localized at the minority spin Mn atoms (light spheres in Fig. 1). In order to emphasize the d character of the wave functions, we have chosen the top view, although the wave functions of the other minority Mn atom are just below the top ones and are not visible. The value of $M_{ij}^{\sigma\sigma'}$ is not determined by a single contribution, but rather the result of the sum of many contributions with different signs.

While Mn is the only magnetically active species in the complex, the remaining atoms affect the magnetic properties of the molecule. In particular the electric field of the twelve Br^- ions can affect the MAE through its effects on the electronic structure and on the spin-orbit coupling. Effects of the Br ions on the electronic structure are of a chemical nature, and a detailed analysis is beyond the scope of this work. However, direct effects on the spin-orbit coupling energy

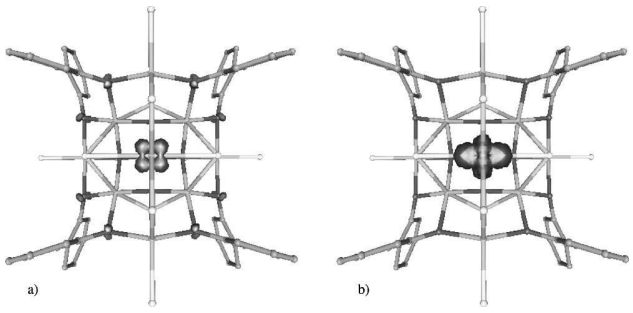

FIG. 3. Isolines at $0.005e/a_B^3$ of the square of the wave functions [occupied majority state (a) and unoccupied minority state (b)] that contribute most to the matrix elements $M_{ij}^{\sigma\sigma'}$. The view is from top with respect to the earlier figures. It is clearly visible that the matrix element connects majority and minority d states at the same Mn atom.

could raise the possibility that even small variations in the positions of these ions could affect the magnetic properties of the molecule.

To measure the effects of the Br^- ions on the electronic structure we repeated the calculations with various subsets of the Br^- ions. For each removed Br we also removed an extra electron, keeping the remaining molecule isoelectronic with the original complex. For these systems with either zero, four, or eight Br atoms, we observed a range of behaviors. In some cases the electronic structure near the Fermi level was similar to the original molecule, although it never showed truly rigid-band-like behavior. In other cases, however, the electronic structure changed significantly, sometimes completely closing the HOMO-LUMO gap. Associated with these electronic structure changes were large changes in the MAE, including changes in the magnitude of the anisotropy barrier, as well as instances of changes to an easy-plane system.

To measure the direct effect of the electric field of the Br ions on the spin-orbit coupling, external Coulomb potentials which acted to cancel the long range affects of the Br anions were added and the spin-orbit interaction and magnetic anisotropy were recomputed. This neutralized the electric field due to the Br^- ions near the Mn sites without changing the electronic structure of the molecule. We tested the effects with neutralizing charge distributions of various widths, and by neutralizing four, eight, or all twelve Br anions. The MAE changed by less than 1 K in all of these calculations. We therefore conclude that the electric fields created by the Br^- ions do not have a significant effect on the magnetic properties of the molecule.

In conclusion, we present a study of the electronic and magnetic properties of the Mn_{10} single molecule magnet. We confirm the experimentally suggested magnetic ordering, although we find that a state with $S=13$ is the magnetic ground state in contrast to the $S=12$ state suggested from high field EPR measurements[8]. In agreement with experiment we find the Mn_{10} unit is an easy-axis system with a small barrier of 9.5 K and the compensating cluster in the molecular crystal, which has one Mn atom with $S=5/2$, is an easy plane system with a MAE of 0.1 K, negligible compared with the Mn_{10} unit. We show that the magnetic anisotropy is determined by a competition between different spin channels involved. This competition is the main reason for the small barrier observed. The electric field caused by the negative charges of Br anions has no significant direct effect on the spin-orbit coupling or the MAE, although their chemical interactions do have significant effect on the electronic structure and therefore on the MAE. The states most important for the magnetic anisotropy energy involve transitions between occupied majority and unoccupied minority *d* states at the same Mn atom.

J.K. would like to thank the Schloeßmann Foundation for financial support and R. Sessoli for helpful discussions. The work was partially supported by the Office of Naval Research and the DOD HPCMO.

*Electronic address: j.kortus@fkf.mpg.de

[1] R. Sessoli, D. Gatteschi, A. Caneschi, and M.A. Novak, Nature (London) **365**, 141 (1993).
[2] J. Friedman, M.P. Sarachik, J. Tejeda, J. Maciejewski, and R. Ziolo, Phys. Rev. Lett. **76**, 3830 (1996); L. Thomas, F. Lionti, R. Ballou, D. Gatteschi, R. Sessoli, and B. Barbara, Nature (London) **383**, 145 (1996).
[3] J. Van Vleck, Phys. Rev. **52**, 1178 (1937).
[4] M.R. Pederson and S.N. Khanna, Phys. Rev. B **60**, 9566 (1999).
[5] M.R. Pederson and S.N. Khanna, Chem. Phys. Lett. **307**, 253 (1999); M.R. Pederson and S.N. Khanna, Phys. Rev. B **59**, R693 (1999).
[6] K.M. Mertes, Y. Suzuki, M.P. Sarachik, Y. Paltiel, H. Shtrikman, E. Zeldov, E. Rumberger, D.N. Hendrickson, and G. Christou, Phys. Rev. Lett. **87**, 227205 (2001).
[7] A.L. Barra, D. Gatteschi, and R. Sessoli, Phys. Rev. B **56**, 8192 (1997).
[8] A.L. Barra, A. Caneschi, D. Gatteschi, D.P. Goldberg, and R. Sessoli, J. Solid State Chem. **145**, 484 (1999).
[9] P. Hohenberg and W. Kohn, Phys. Rev. **136**, B864 (1964).
[10] W. Kohn and L.J. Sham, Phys. Rev. **140**, A1133 (1965).
[11] M.R. Pederson and K.A. Jackson, Phys. Rev. B **41**, 7453 (1990).
[12] K.A. Jackson and M.R. Pederson, Phys. Rev. B **42**, 3276 (1990).
[13] A. Briley, M.R. Pederson, K.A. Jackson, D.C. Patton, and D.V. Porezag, Phys. Rev. B **58**, 1786 (1998).
[14] D.V. Porezag and M.R. Pederson, Phys. Rev. B **54**, 7830 (1996).
[15] D.V. Porezag and M.R. Pederson, Phys. Rev. A **60**, 2840 (1999).
[16] M.R. Pederson, D.V. Porezag, J. Kortus, and D.C. Patton, Phys. Status Solidi B **217**, 197 (2000).
[17] J.P. Perdew, K. Burke, and M. Ernzerhof, Phys. Rev. Lett. **77**, 3865 (1996).
[18] R. Sessoli (private communication).

Appendix L

Kortus J., Hellberg C. S. and Pederson M. R.

Hamiltonian of the V_{15} Spin System from First-Principles Density-Functional Calculations

Phys. Rev. Lett. **86**, 3400-3403 (2001)

Hamiltonian of the V_{15} Spin System from First-Principles Density-Functional Calculations

Jens Kortus,* C. Stephen Hellberg, and Mark R. Pederson

Center for Computational Materials Science, Code 6390, Naval Research Laboratory, Washington, D.C. 20375

(Received 11 July 2000)

We report first-principles all-electron density-functional-based studies of the electronic structure, magnetic ordering, and anisotropy for the V_{15} molecular magnet. From these calculations, we determine a Heisenberg Hamiltonian with five antiferromagnetic and one *ferromagnetic* exchange couplings. We perform direct diagonalization to determine the temperature dependence of the susceptibility. This Hamiltonian reproduces the experimentally observed spin $S = 1/2$ ground state and low-lying $S = 3/2$ excited state. A small anisotropy term is necessary to account for the temperature independent part of the magnetization curve.

DOI: 10.1103/PhysRevLett.86.3400 PACS numbers: 75.50.Xx, 75.30.Et, 75.30.Gw, 75.45.+j

With the continued interest in the fabrication and optimization of miniaturized magnetic devices [1], future design considerations will require an understanding of nanoscale magnetic systems. In order to transition such materials into simple devices it is necessary to be able to explain how interactions such as spin-spatial coupling and spin-spin exchange effects may couple collectively to create a seemingly single-spin system. Further, it is necessary to determine the temperature range at which such systems will indeed behave collectively. In general the properties of a nanoscale system of coupled spins depend directly on the strength of the exchange parameters and on the size and sign of the anisotropy energy due to spin-orbit coupling. While these parameters are generally determined by the transition metal atoms, the ligands and other nonmagnetic atoms are responsible for stabilizing the array of spins. Requisite to a complete computational understanding of such spin systems is the ability to account for the strong ligand-metal interactions and to determine whether the behavior of a given spin system is mainly mediated by the anisotropy, by spin-spin coupling, or by a combination of the two.

Recently, the Mn_{12}-acetate and Fe_8 molecules [2] have attracted considerable interest because they behave as high-single-spin systems (total spin $S = 10$) at temperature ranges on the order of 20–60 K. Because of their large magnetomolecular anisotropy energy these systems retain their moment orientation at reasonably high temperatures and exhibit the phenomena of resonant tunneling of magnetization at well defined magnetic fields [3,4].

The $K_6[V_{15}As_6O_{42}(H_2O)]8H_2O$ molecular crystal, first synthesized by Müller and Döring [5,6], represents a transition-metal spin system in the same size regime as the Mn_{12} and Fe_8 molecular crystals. In contrast to Mn_{12} and Fe_8 molecules, the V_{15} molecule is thought to behave as a weakly anisotropic magnet composed of 15 spin $s = 1/2$ particles which couple together to form a molecule with a total spin $S = 1/2$ ground state. Besides the fundamental interest in understanding quantum effects in these nanomagnets, they might be also relevant for implementations of quantum computers [7]. Calculations on such correlated systems present a challenge to mean-field frameworks such as density-functional theory because it is often not possible to construct a single collinear reference state which preserves the inherent symmetry of the system and has the correct spin quantum numbers.

This work utilizes an efficient coupled multilevel analysis which relies on fitting density-functional energies to mean-field Heisenberg or Ising energies in order to determine the exchange parameters. The approximate exchange parameters gleaned from the first N Ising configurations were used to find the next lowest energy Ising configuration and subsequently to improve the parametrization of the exchange parameters. "Self-consistency" of this approach is determined when the predicted Ising levels are unchanged by the addition of data from new Ising configurations. The coupling of the density-functional method to a classical Ising representation allowed us to determine the exchange parameters by considering only several spin configurations. Further, the resulting ground-state spin configuration within density-functional theory exhibits the correct spin projection of $1/2$. With the exchange parameters determined, we diagonalize the complete many-body Heisenberg Hamiltonian to calculate the susceptibility and spin correlation functions for comparison with experiment. The many-body basis is complete, so all states are allowed including noncollinear spin arrangements and quantum disordered phases [8].

Starting from x-ray data [9] we generated several unit cells and isolated a single $K_6[V_{15}As_6O_{42}(H_2O)]$ unit. In order to optimize the geometry within the quasi- D_3 symmetry of the V_{15} molecule [5], we initially replaced the statistically oriented water molecule at the center of the molecule by a neon atom and used an $S = 3/2$ spin configuration which does not break the crystallographic symmetry. The Ising configuration of this molecule consists of three aligned spin-$\frac{1}{2}$ V atoms in the triangle and equivalent upper and lower hexagons composed of a ring of antiferromagnetically (AF) coupled spin-$\frac{1}{2}$ V atoms.

The geometry of the molecule was then optimized within the all-electron density-functional methodology using the generalized-gradient approximation (GGA) [10]. The

 0031-9007/01/86(15)/3400(4)$15.00

calculations were performed with the Naval Research Laboratory Molecular Orbital Library (NRLMOL) [11]. Calculations on 49 geometrical configurations were performed during the conjugate-gradient relaxation of the molecule. Subsequent calculations show that the geometrical, electronic, and magnetic properties of this system are unaffected by the presence or type of inert moiety enclosed within the void. Using this geometry, we performed eleven additional calculations on different spin configurations (see Table I) to determine the six exchange parameters (J's) of the Heisenberg Hamiltonian

$$H = \sum J_{ij} \mathbf{S}_i \cdot \mathbf{S}_j \,, \tag{1}$$

as well as the spin configuration of the density-functional ground state [8]. The J's used in the above Hamiltonian are defined according to Fig. 1. As shown in Table I, we have included high-spin configurations (XI, XII, XIII), which generally have some symmetry as well as lower-spin nonsymmetric configurations. The energy for the high-spin $S = 15/2$ ferromagnetic (FM) state (XIII) of 873 meV is predominantly caused by a large AF exchange coupling (J) between the most closely bonded hexagonal V atoms. However, the 113 meV splitting between the $S = 9/2$ and $S = 15/2$ states (XII and XIII) shows that there is a reasonably strong AF coupling, approximately 18 meV on average, between the triangular and hexagonal atoms. All of the data displayed in Table I have been used to determine the exchange parameters from a least square fit to the mean-field solution of the Heisenberg Hamiltonian (1). The fit is very good with errors ranging from 0.1–1.55 meV. The fit leads to exchange parameters of $J = 290.3$ meV, $J' = -22.7$ meV, $J'' = 15.9$ meV, $J1 = 13.8$ meV, $J2 = 23.4$ meV, and $J3 = 0.55$ meV, where positive numbers correspond to AF and negative ones to FM interactions. The *ferromagnetic* interaction J' is a surprising result [12] and deserves further discussion since it is qualitatively different from earlier assumptions based on entirely AF interactions [6,13]. Ferromagnetic coupling is possible without polarizing the oxygens through a 4th order process similar to superexchange. In superexchange, the intermediate state has the lowest d orbital on the V doubly occupied with up and down electrons [14]. However, electrons can also hop to higher energy d orbitals on the V's. In this case both parallel and antiparallel spins are allowed without violating the Pauli exclusion principle, but Hund's rule coupling prefers parallel alignment. The superexchange process (same d orbital) completely excludes the process with same-spin electrons while the FM process (different d orbitals) merely favors FM alignment. Thus a FM coupling is obtained if the V-O hopping matrix elements into the higher d orbital are significantly larger than the matrix elements for the hopping of O electrons into the lowest energy d orbital. The occurrence of such interactions is possible in a low-symmetry system such as the one studied here.

Even with this FM interaction, our spin Hamiltonian yields an $S = 1/2$ ground state composed largely of Ising configurations similar to the one depicted in Fig. 1. This Ising configuration was predicted from the J's from earlier fits to DFT energies and corresponds to the ground-state DFT configuration (I).

We have fully diagonalized the Heisenberg Hamiltonian (1). Using all symmetries, the largest irreducible many-body subspace has dimension 2145. We find a spin-1/2 Kramer doublet as the ground state with a low-lying spin-3/2 quadruplet as shown in Fig. 1. The rest of the spectrum is well separated from these eight states. The large value of J binds the spins in the hexagons into singlets. The low-energy physics arises from the inner triangle spins interacting with each other both directly and with an effective coupling through the hexagons, yielding the doublet-quadruplet spectrum [15]. There are two important energy scales in the spectrum: Δ, the gap between the doublet and quadruplet, and J, the energy at which the

TABLE I. DFT energies (E) of calculated Ising configurations, energies obtained from the fit, and $4\langle S_i^q S_j^q \rangle$ along each of the six bonds. Also included is the anisotropy shift δ for the $M_s = S$ state of each Ising configuration. A least square fit of this data leads to exchange parameters of $J = 290.3$, $J' = -22.7$, $J'' = 15.9$, $J1 = 13.8$, $J2 = 23.4$, and $J3 = 0.55$ meV.

E (meV)	Fit	J	J'	J''	$J1$	$J2$	$J3$	Spin	Label	δ (K)
−78.37	−78.44	−6	2	−2	6	−6	−1	1/2	I	0.8
−73.39	−73.63	−6	2	−2	4	−4	−1	1/2	II	
−35.48	−35.08	−6	−2	2	4	−4	−1	1/2	III	
−34.89	−34.53	−6	−2	2	4	−4	3	3/2	IV	
0.00	−0.79	−6	−6	6	6	−6	3	3/2	V	1.5
8.38	8.28	−6	−6	6	2	−2	−1	1/2	VI	1.3
28.14	28.08	−6	−6	6	−6	6	3	3/2	VII	
126.32	126.14	−4	−4	6	4	−6	3	1/2	VIII	
129.17	128.88	−4	−4	2	6	−4	3	5/2	IX	
278.35	278.50	−2	−6	2	4	−4	3	3/2	X	
434.22	435.78	0	0	6	6	0	3	9/2	XI	1.6
760.75	760.76	6	6	6	−6	−6	3	9/2	XII	1.6
873.11	872.35	6	6	6	6	6	3	15/2	XIII	1.8

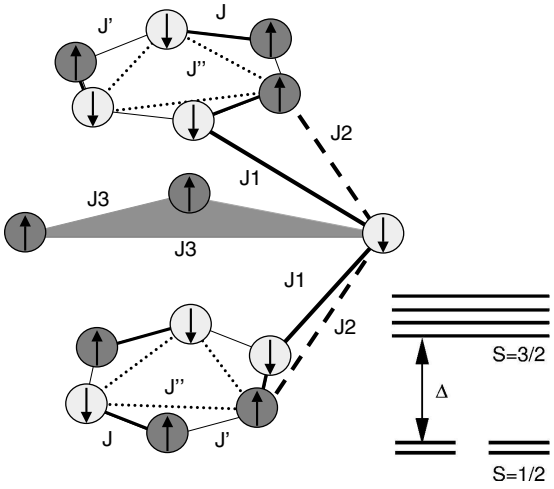

FIG. 1. The 15 magnetic vanadium atoms of the $K_6[V_{15}As_6O_{42}(H_2O)]$ molecule. They form two hexagonal layers and an inner triangular layer of vanadium atoms sandwiched within. The arrows show the lowest energy spin configuration found from DFT calculations. The six exchange parameters used in the Heisenberg Hamiltonian are shown as lines. Schematically displayed are energy levels of the Kramer doublet ($S = 1/2$) ground state and the low-lying quadruplet ($S = 3/2$) separated by Δ.

singlets in the hexagon break and the molecule starts to behave as more than three spins.

The low-energy effective interaction between inner triangle spins proceeds via $J1$ and $J2$ (which frustrate each other) to a hexagon singlet, via J' and J'' to a neighboring singlet, and finally via $J1$ and $J2$. A larger contribution to Δ comes from a direct interaction through $J3$ mediated by hopping through O and As levels. Thus simple perturbation theory [6] yields

$$\Delta = \frac{3}{4}\,\frac{(J2 - J1)^2(J'' - J')}{J^2} + \frac{3}{2}\,J3\,. \qquad (2)$$

Comparing our calculated susceptibility with experiment [13], we find the low-temperature behavior indicates our doublet-quadruplet gap $\Delta \approx 10$ K to be significantly larger than the experimental value of $\Delta \approx 3.7$ K, while the high-temperature behavior shows our calculated value of J is too large. Both of these discrepancies can be explained almost entirely by J's that are too large within the density-functional-based treatment, as known for other vanadium systems [8].

Agreement with experiment for the low temperature Δ can be achieved by dividing all J's by a constant factor of 2.9. Figure 2 shows our calculated result with rescaled J's compared to experimental data from Chiorescu. A uniform scaling of our calculated exchange parameters is not able to obtain the right low and high temperature behavior at the same time. The high temperature behavior could be improved by further reducing J with corresponding adjustments to the other couplings to keep Δ constant.

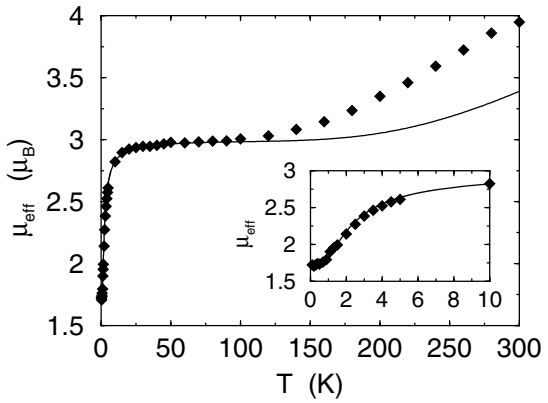

FIG. 2. The effective moment $\mu_{\text{eff}} = \sqrt{3\chi T}$ calculated with all J's uniformly rescaled by dividing by a constant factor of 2.9. The diamonds are the actual experimental values from Chiorescu. The inset shows the low temperature behavior.

A set of AF interactions [6] also fits the experimental results. In fact any set of parameters with the correct values of J and Δ given by Eq. (2) will fit the effective moment well. To support future efforts aimed at experimentally confirming our relative parameters, we have calculated the spin-spin correlation function $C_S = 4\langle S_i^q \cdot S_j^q \rangle$, with q representing the arbitrary quantization axis. Since J is always largest, the spins tend to form a singlet along this bond, yielding $C_S(J) \cong -1$ (AF correlation). The three inner triangle spins form a noncollinear arrangement with $C_S \cong -0.33$ between all pairs of spins. The direct $J3$ coupling reduces the correlations between triangle and hexagon spins. We find $C_S(J1) \cong +0.02$ and $C_S(J2) \cong -0.02$ (FM and AF correlations, respectively), while the coupling constants of Ref. [6] yield $C_S(J1) \cong +0.12$ and $C_S(J2) \cong -0.14$. This prediction should be measurable with neutron scattering.

Chiorescu *et al.* observe that rotation of the spin projection is achieved without encountering a barrier [13] and Dobrovitski *et al.* posit that the V_{15} molecule is indeed a low anisotropy system [15]. As shown below the existence of either easy-plane or easy-axis anisotropy will shift the $M_s = 3/2{-}1/2$ Zener-Landau tunneling transitions that have been observed by Chiorescu *et al.* [13].

Recently, Pederson and Khanna have developed a new method for accounting for second-order anisotropy energies [16]. This method relies on a simple albeit exact method for spin-orbit coupling and a second-order perturbative treatment of the spin-orbit operator to determine the dependence of the total energy on spin projection. Initial applications to Mn_{12} lead to a density-functional-based second-order anisotropy energy of 55.7 K [17] which is in essential agreement with the experimentally deduced values of 55.6 K [18]. We have generalized this methodology to systems with arbitrary symmetry and have calculated the anisotropy energy for several different spin configurations of the V_{15} molecule.

We have calculated the anisotropy energy for the lowest Ising configurations with one, three, nine, and fifteen unpaired electrons, as given in Table I. In all cases we find that the V_{15} possesses weak easy-plane anisotropy. This result ensures that anisotropy effects will not change the total spin of the V_{15} ground state. Examination of the expression for the second order anisotropy energy in Ref. [16], shows that such energies do not necessarily scale as the square of the total moment. Indeed, as shown in Table I, we find that the anisotropic effects are in fact only weakly dependent on the total spin and that the energy of the $M_s = S$ state increases by approximately $\delta = 0.8$ to 1.8 K. Chiorescu *et al.* show that the broadening of the Zener-Landau tunneling fields decreases with temperature for the $|1/2, 1/2\rangle$ to $|1/2, -1/2\rangle$ transitions but are independent of temperature for the $|3/2, 3/2\rangle$ to the $|3/2, 1/2\rangle$ transitions [13]. This behavior is exactly what is expected from a sample containing weak easy-plane spin anisotropy. At sufficiently low temperatures, only the $S = 3/2$ and $S = 1/2$ states are relevant, and the field-dependent crossing of these states depends on whether the magnetic field is parallel or perpendicular to the easy plane. The broadening is proportional to the difference of the magnetic anisotropy energy for the different spin configurations involved. Because of the small anisotropy in V_{15} the effect will be small. Although it is not possible to translate the DFT obtained anisotropy energies directly to the quantum mechanical many-spin ground state discussed here, we obtain from these energies tunnel field broadenings between 0.1 to 0.48 T which envelop the experimentally observed field broadening of about 0.2 T [13]. In powdered samples, the small easy-plane anisotropy would lead to a broadening in the tunneling field and in single crystals the effect would change the tunneling fields as a function of field orientations.

To summarize, we have performed accurate all-electron density-functional calculations on the V_{15} cluster as a function of geometry and spin configuration. By dynamically coupling the mean-field density-functional approach to exact-diagonalization of a many-spin Heisenberg representation, we have efficiently determined the lowest density-functional configurations and the entire Heisenberg spin excitation spectrum. Our calculations suggest that the small experimentally observed orientational dependence of the tunneling field for the $M_s = 3/2$ to $M_s = 1/2$ is a signature of configuration dependent magnetic anisotropy in this molecule. The method used here is general and allows one to characterize both systems which are potentially useful for magnetic storage (Mn_{12}, Fe_8) and systems which show quantum coherence, such as the one studied here.

This work was supported in part by ONR Grants No. N0001498WX20709 and No. N0001400AF00002. Computations were performed at the DoD Major Shared Resource Centers. We thank I. Chiorescu for enlightening discussions and for supplying the data used in Fig. 2.

*Present address: MPI für Festkörperforschung, Postfach 80065, D-70506 Stuttgart, Germany.

[1] R. F. Service, Science **287**, 1902 (2000); S. Sun, C. B. Murray, D. Weller, L. Folks, and A. Moser, Science **287**, 1989 (2000).

[2] A. Caneschi, D. Gatteschi, C. Sangregorio, R. Sessoli, L. Sorace, A. Cornia, M. A. Noval, C. Paulsen, and W. Wernsdorfer, J. Magn. Magn. Mater. **200**, 182 (1999), and references there.

[3] J. Friedman, M. P. Sarachik, J. Tejada, and R. Ziolo, Phys. Rev. Lett. **76**, 3820 (1996); L. Thomas, F. Lionti, R. Ballou, D. Gatteschi, R. Sessoli, and B. Barbara, Nature (London) **383**, 145 (1996).

[4] C. Sangregorio, T. Ohm, C. Paulsen, R. Sessoli, and D. Gatteschi, Phys. Rev. Lett. **78**, 4645 (1997).

[5] A. Müller and J. Döring, Angew. Chem., Int. Ed. Engl. **27**, 1721 (1988).

[6] D. Gatteschi, L. Pardi, A. L. Barra, A. Müller, and J. Döring, Nature (London) **354**, 463 (1991).

[7] N. D. Mermin, Phys. Today **53**, No. 7, 11 (2000); D. P. DiVincenzo and D. Loss, J. Magn. Magn. Mater. **200**, 202 (1999).

[8] C. S. Hellberg, W. E. Pickett, L. L. Boyer, H. T. Stokes, and M. J. Mehl, J. Phys. Soc. Jpn. **68**, 3489 (1999).

[9] A. Müller and J. Döring, Z. Anorg. Allg. Chem. **595**, 251 (1991).

[10] J. P. Perdew, K. Burke, and M. Ernzerhof, Phys. Rev. Lett. **77**, 3865 (1996).

[11] M. R. Pederson and K. A. Jackson, Phys. Rev. B **41**, 7453 (1990); K. A. Jackson and M. R. Pederson, Phys. Rev. B **42**, 3276 (1990).

[12] M. A. Korotin, I. S. Elfimov, V. I. Anisimov, M. Troyer, and D. I. Khomskii, Phys. Rev. Lett. **83**, 1387 (1999).

[13] I. Chiorescu, W. Wernsdorfer, A. Müller, H. Bögge, and B. Barbara, Phys. Rev. Lett. **84**, 3454 (2000); cond-mat/9911180.

[14] J. B. Goodenough, *Magnetism and the Chemical Bond* (Wiley, New York, 1963).

[15] V. V. Dobrovitski, M. I. Katsnelson, and B. N. Harmon, Phys. Rev. Lett. **84**, 3458 (2000).

[16] M. R. Pederson and S. N. Khanna, Phys. Rev. B **60**, 9566 (1999).

[17] M. R. Pederson and S. N. Khanna, Chem. Phys. Lett. **307**, 253 (1999); M. R. Pederson and S. N. Khanna, Phys. Rev. B **59**, R693 (1999).

[18] A. L. Barra, D. Gatteschi, and R. Sessoli, Phys. Rev. B **56**, 8192 (1997).